APPLIED COMPUTATIONAL ELECTROMAGNETICS SOCIETY JOURNAL

November 2025
Vol. 40 No. 11
ISSN 1054-4887

The ACES Journal is abstracted in INSPEC, in Engineering Index, DTIC, Science Citation Index Expanded, the Research Alert, and to Current Contents/Engineering, Computing & Technology.

The illustrations on the front cover have been obtained from the ARC research group at the Department of Electrical Engineering, Colorado School of Mines

Published, sold and distributed by: River Publishers, Alsbjergvej 10, 9260 Gistrup, Denmark

November 2025 REVIEWERS

Giovanni Angiulli
Ruaa Anooz
Alireza Baghai-Wadji
Chandresh Dhote
Javad Ebadi
Nunzia Fontana
Alessandro Formisano
Venkata Surya Bhavana Harish Gollavilli
Yanyan Huang
Taha Imeci
Yongwei Li
Enrique Melgoza
Andrew Peterson
Qian Qi
C. J. Reddy
Partha Shome
Mehmet Tabakcioglu
Marsellas Waller
Julia Wolff
Anupam Yadav

THE APPLIED COMPUTATIONAL ELECTROMAGNETICS SOCIETY JOURNAL

Vol. 40 No. 11 November 2025

TABLE OF CONTENTS

Learning the Basic Physics of Electromagnetic Radiation Through Computational Modeling

Edmund K. Miller

Life Fellow, IEEE
Los Alamos National Laboratory (Retired)
e.miller@ieee.org

Abstract – While electromagnetics (EMs) may be perceived to be a mathematically intensive subject, the following discussion demonstrates that many important education-related aspects of EM radiation can be "discovered" through computational modeling. The goal here is to demonstrate an intuitive learning environment that reveals important features of EM physics to incentivise a desire to learn about the underlying mathematics on which the computer model is based. The idea is that seeing the fascinating details that the equations produce prior to confronting the possibly intimidating background mathematics can be a more productive and enjoyable exercise.

Index Terms – Charge acceleration, computer modeling, electromagnetic radiation, Lienard-Wichert fields, Poynting vector, reflection radiation, source radiation, time-domain electromagnetics.

I. INTRODUCTION

Electromagnetic radiation is a phenomenon produced by charge acceleration. This basic physical fact provides the explanation for how antennas radiate and receive electromagnetic (EM) energy (time domain) or power (frequency domain) and for how other electromagnetic interactions occur. The mathematical equations that provide an analytical description for the radiation, propagation and scattering of EM fields were formalized by James Clerk Maxwell in 1846 and are now called Maxwell's Equations (MEs). His unification of these equations originated from the experimental and analytical work of numerous scientists (in alphabetical order) such as Ampere, Columb, Farady, Gauss, Heaviside, Henry, Hertz, Kirchhoff, Lorentz, Oersted, Poisson, Poynting, Volta, Weber and others. Some of these names are attached to various quantities in electromagnetics and electrical engineering as recognition of their contributions. Most of this initial development involved various measurements in the late 18$^{\text{th}}$ and 19$^{\text{th}}$ centuries whose results led to mathematical formulas or models to quantitatively describe them.

The motivation for this discussion is not to present a conventional introduction to the mathematics of MEs. Instead, it is intended to illustrate, via various physics' phenomena, that mathematics alone need not be the sole focus of EM. Instead, computational modeling has become a complementary and indispensable tool in the discipline. The goal is to show prospective students the fascinating reality of EM radiation made possible by computational electromagnetics, literally computer experimentation, to encourage student interest in its study. The fundamental equation (1) below demonstrates analytically the statement above about charge acceleration. This expression, derived from MEs exhibits the charge-acceleration dependence of EM radiation in what is known as the Lienard-Wichert fields [1, 2]:

$$\mathbf{E} = q\left[\frac{1-v^2/c^2}{(R-\mathbf{R}\cdot\mathbf{v}/c)^3}\right] \times\left\{\left[\left(\mathbf{R}-\frac{\mathbf{v}}{c}\right)+\frac{\mathbf{R}}{c^2}\times\right]\left[\left(\mathbf{R}-\frac{\mathbf{v}}{c}R\right)\times\frac{d\mathbf{v}}{dt}\right]\right\}, \quad (1)$$

and

$$\mathbf{H} = \frac{1}{R}\mathbf{R}\times\mathbf{E}, \quad (2)$$

for a point charge q in free space at the origin having velocity $\mathbf{v}$ and acceleration $\mathbf{a} = d\mathbf{v}/dt$ where $\mathbf{R}$ is the vector coordinate of the $\mathbf{E}$ and $\mathbf{H}$ field locations in a spherical coordinate system. Note that when v $\ll$ c the acceleration term in equation (1) simplifies to

$$\mathbf{E} = \mathbf{r}\times\mathbf{r}\times\mathbf{a}q/Rc^2, \quad (3)$$

where $\mathbf{r}$ is a unit vector in the $\mathbf{R}$ direction.

A careful examination of Eq. (1) leads to the conclusion that only the acceleration term falls off as $1/R$ to thus account for EM radiation, as may be clearer in Eq. (3). This is because the EM power-flow density as expressed by Poynting's vector $\mathbf{S}$ is given by

$$\mathbf{S} = \mathbf{E}\times\mathbf{H} \text{ in w/m}^2, \quad (4)$$

Submitted On: September 05, 2025
Accepted On: October 25, 2025

https://doi.org/10.13052/2025.ACES.J.401101

and falls as $1/R^2$ due to the acceleration terms of $\mathbf{E}$ and $\mathbf{H}$. This means that over an enclosing spherical surface the total power radiated by the acceleration of q becomes a constant independent of $\mathbf{R}$ in what is called the radiation field.

Equation (1) may appear to be somewhat intimidating but is not used to obtain the results to be presented. Rather, it is included to emphasize the point that charge acceleration is the root cause of EM radiation. However, equation (1) is not routinely involved in solving most engineering EM problems whose solutions are developed from the Maxwell differential equations or their integral counterparts. It should be appreciated that charge acceleration does not explicitly appear in these equations. Indeed, charge acceleration is not needed to solve typical antenna, propagation or scattering problems. While this may appear to be a fortunate simplification, it can obscure important aspects of radiation physics and the insight that knowledge could reveal about where charge acceleration occurs on an antenna or scatterer and radiation actually originates.

Any valid EM computational or numerical model must include the effect of charge acceleration if it is to correctly account for radiation. Thus it is reasonable to expect that where charge acceleration occurs in any such numerical model should be identifiable. While this should be true however a given problem is modeled, a time-domain approach seems more attractive since acceleration is a time-domain phenomenon. Observe that there are two principle types of time-domain EM models based on either differential or integral equations. A differential-equation-based computer model samples the fields on a mesh having the dimensionality of the problem being solved. Thus for a general three-dimensional object the sampling is done on a 3D mesh, with a popular approach known as finite-difference time domain (FDTD) [3].

Here, however, the focus is instead on a time-domain integral equation model specialized for wires, the Thin-Wire Time Domain (TWTD) [4] code. This is an especially relevant model for the charge-acceleration cause of EM radiation. The time domain results derived from TWTD will be demonstrated to provide insight into EM radiation physics that is less obvious in the frequency domain. A time-domain model also has the advantage of yielding broadband frequency results in a single computation.

Instead of sampling fields on a mesh, an integral-equation approach is instead based on integrating over an object whose current and charge produce electric and magnetic fields. In the results to be presented below, this is done by deriving from ME an expression for the electric field due to the charge and current on a thin wire. This is a "standard" boundary-value problem in electromagnetics where the wire object of interest is usually, but not necessarily, a perfect electric conductor (PEC). Equation (1) applies to a point charge in free space but also accounts for the role of equivalent charge on a PEC.[1] The goal is to find the current and charge flow, or induced sources, on a wire of some specified geometry when excited by some specified electric field. Note that both time-domain models also have frequency-domain counterparts. For a wire the perpendicular or normal electric field (E-field) terminates on equivalent charge and the circular or tangential magnetic field terminates on equivalent current.

The thin-wire approximation, an exceptionally well-validated approach used in TWTD and other wire computational models as shown in Fig. 1, assumes: (a) that the current on the wire surface can be modeled as a filament flowing on the wire axis; and (b) that the boundary condition of the electric field can be applied a distance of the wire radius a away from the current filament. The electric field of the filamentary current in TWTD is given by [5]:

$$\mathbf{E}(\mathbf{r},t) = -\frac{\mu_o}{4\pi}\int_{C(r)}\left[\frac{\mathbf{s}'}{R}\frac{\partial}{\partial t'}I\left(s',t'\right) + c\frac{\mathbf{R}}{R^2}\frac{\partial}{\partial s'}I\left(s',t'\right) - c^2\frac{\mathbf{R}}{R^3}q\left(s',t'\right)\right]ds', \tag{5}$$

where $I\left(s'.t'\right)$ and $q\left(s'.t'\right)$ are the current and charge density respectively, and where $C(\mathbf{r})$ is the spatial geometry of the wire with $\mathbf{s}$ is a unit tangent vector at the wire surface.

Also, $s = s(\boldsymbol{r}), s' = s\left(\boldsymbol{r}'\right), ds' = ds\left(\boldsymbol{r}'\right), R = |\mathbf{R}| = |\mathbf{r} - \mathbf{r}'|$ and the unprimed coordinates $\boldsymbol{r}$ and t denote the observation point location and the primed coordinates $\mathbf{r}'$ and $t' = t - R/c$ the source location which accounts for the propagation time delay between the source and observation points. The differential operators in (5) are with respect to the observation coordinates. If we let $\mathbf{s} = \mathbf{s}(\mathbf{r})$ and $\mathbf{s}' = \mathbf{s}\left(\mathbf{r}'\right)$ be the unit tangent vectors to $C(\mathbf{r})$ at $\mathbf{r}$ and $\mathbf{r}'$ then for a PEC wire the boundary condition is

$$\mathbf{s}\cdot\left(\mathbf{E} - \mathbf{E}^A\right) = 0, \tag{6}$$

with $\mathbf{E}^{\mathrm{A}}$ the applied field that causes the current and charge. When equation 6 is combined with equation 5,

[1] Assuming an object to be a PEC is a common boundary condition used in EM computer modeling and is acceptably accurate for most materials used for antennas and radar targets. This means that EM fields originate or terminate at the surface of an object on what are called equivalent sources. In particular, the normal electric field creates an excess of charge at its termination point depending on whether the E-field originates, causing positive charge or terminates, to cause negative charge at that point on the wire's surface. The equivalent, essentially massless, charge density this creates follows the propagating EM field moving at light speed in the external medium. The validity of this model is confirmed by experimental measurements.

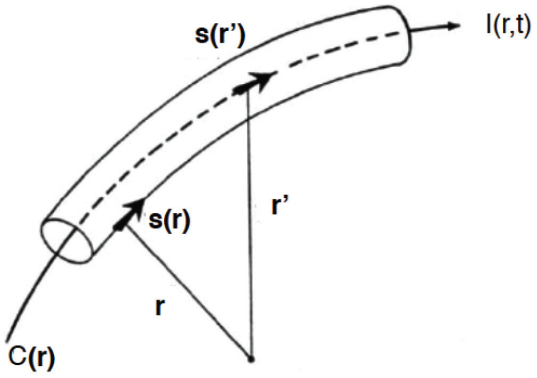

Fig. 1. Geometry for thin-wire electric-field integral equation (from [7]).

the following integral equation results:

$$\mathbf{s}\cdot\mathbf{E}^A(\mathbf{r},t)=\frac{\mu_o}{4\pi}\int_{C(r)}\left[\mathbf{s}\cdot\mathbf{s}'\frac{\partial}{R}\frac{\partial}{\partial t'}I\left(s',t'\right)+c\frac{\mathbf{s}\cdot\mathbf{R}}{R^2}\frac{\partial}{\partial s'}I\left(s',t'\right)-c^2\frac{\mathbf{s}\cdot\mathbf{R}}{R^3}q\left(s',t'\right)\right]ds', \tag{7}$$

where $\mathbf{r}\in C(\mathbf{r})+a(\mathbf{r})$ and $a(\mathbf{r})$ is the wire radius at point $\mathbf{r}$ and he charge is given by

$$q\left(s',t'\right)=-\int_{-\infty}^{\prime}\frac{\partial}{\partial s'}I\left(s',\tau\right)d\tau. \tag{8}$$

Equation (7) provides the analytical basis for TWTD and is called an integral equation because the unknown quantities requiring solution are under the integral sign. The procedure used to develop a solution is called the moment method [6, 7]. Most of the numerical examples in the next section are obtained from TWTD, but for illustrative comparison some frequencydomain results obtained from the NEC (Numerical Electromagnetics Code) [8] are also included.

To conclude this introductory discussion it's relevant to point out that there is a graphical approach to demonstrate the effects of charge acceleration known as the "E-Field Kink Method [8, 9] described next. This method is useful for developing a dynamic visualization of the radiation from a point charge as shown next in Section II but is unlikely to be feasible for the current and charge sources on an extended object.

II. THE E-FIELD KINK MODEL OF RADIATION

Graphical displays of EM radiation fields can be developed without actually solving the MEs using what is known as the "E-field Kink Model of Radiation" [9, 10]. This is made possible by two properties of EM fields, (a) that a charge produces continuous electric-field lines of force and (b) that the speed of light has a finite value.

Consider a point charge located at the origin of a spherical coordinate system in an infinite, homogenous medium. The charge emanates or terminates a radially directed electric field whose lines of force are uniformly distributed in angle with a density proportional to the charge magnitude as in Fig. 2 (a). By convention these field lines originate on positive charge and terminate on negative charge or extend to infinity.

If the charge is instantaneously accelerated to velocity v and coasts for time t_1 its E -field lines will be as shown in Fig. 2 where a "kink" has developed in its field lines which has propagated a radial distance ct_1 from the origin where c is the speed of light. Abruptly stopping the charge at time t_1 causes another E-field kink to be produced that at time t_2 later has now propagated a radial distance ct_2 from the origin as illustrated in Fig. 2.

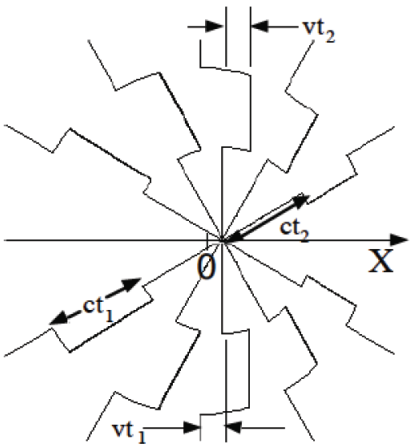

Fig. 2. A snapshot of the E-field of a point charge that has been instantaneously accelerated to a speed v, abruptly stopped at time t_1 and at an additional time interval t_2 later (Fig. 1 from [15]).

Observe that following any of the field lines outward the two kinks are of opposite sign. This is a consequence of the acceleration term in equation (8) since the starting and stopping accelerations are of opposite sign. Note also in Fig. 2 that the length of the field kink gets longer in proportion to distance from the charge, associated with the $1/R$ fall off of the radiated E field and that there is no field kink, or radiation, in the direction of charge motion. Not shown in these plots is the accompanying H-field component with their vector cross product accounting for the Poynting vector power flow in equation (9).

A computer program, Radiation 2, was developed at Stanford University by Professor Blas Cabrerra and his students [11, 12] that develops a time sequence of

plots to create a movie of the E-field lines for several kinds of chargeacceleration motion such as oscillatory, circular, etc. Two stills from this program are presented in Fig. 3. Included in the program are a choice of the geometrical motion and a selection of the peak charge speed and acceleration.

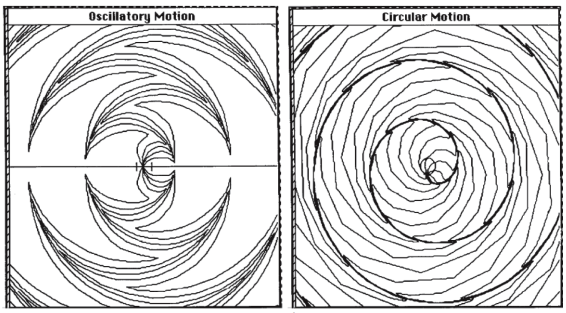

(a) (b)

Fig. 3. Single frames taken from an E-field kink computer program [12] for a point charge undergoing oscillatory linear motion (a) and moving at constant speed around a circle (b) (from [15]).

III. TIME-DOMAIN RESULTS USING TWTD

Electromagnetic radiation is obviously a time-domain phenomenon as it results from the acceleration of charge. Consequently it is most appropriate to examine the details of EM radiation from a time-domain perspective as is done below for a variety of problems. The well-validated computer model based on a time-domain electric-field integral equation for perfect electric conducting (PEC) wires called TWTD (thin wire time domain [5] was used to obtain the results that follow. Basically, these results can be characterized, as computer experiments that emulate what might be done using laboratory measurements were the appropriate equipment to be available. Further examples of the results that follow can be found in [9]. For time-domain modeling of antennas or scatterers, a Gaussian-shaped impulsive excitation is normally used. This produces time and space-limited current and charge pulses on the object whose impulsive far-fields can be associated with locations where they originate from the object being modeled. A Gaussian time-dependent excitation pulse used in TWTD is given by

$$V = V_0 e^{-a(t-t+\text{trax})]^2}, \tag{9}$$

where a is a width parameter and $t_{\max}$ determines the time at which the pulse maximum V_o occurs. The simplest timedomain wire geometry is a straight wire, known as a dipole antenna when excited by a local voltage source. A dipole of length of 5.99 m is modeled with 599 segments of length $\Delta x = 0.01$ m. A wire radius of 10^{-3} m and time step of $\Delta t = \Delta x/c$ are used throughout unless otherwise stated. The current I and charge-density Q times light speed c are shown at several time steps in Fig. 4 for excitation of the dipole antenna at segment 300 by a $1-$V peak Gaussian pulse, an excitation used for all time-domain results presented in the following.

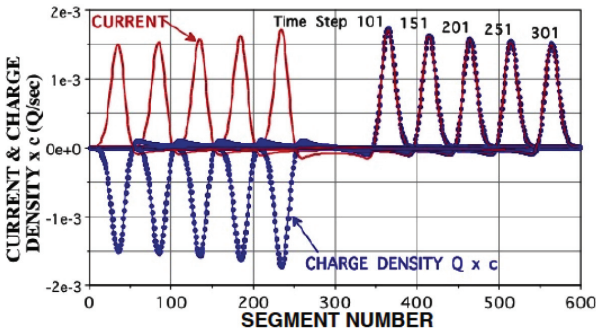

Fig. 4. Charge density Q times light-speed c and the current I for a 599-segment wire excited at its center by a Gaussian voltage pulse at several time steps (Fig. 3.2 from [10]).

Several interesting observations can be made of the results of Fig. 4.

(a) The positive I and Qc_pulses_are numerically equal on the right-hand side of the dipole (i.e. $Qc = I$) but are of opposite signs on the left-half side. This is because a positive charge moving to the right produces a positive current, as also does a negative charge moving in the opposite direction to the left. Their numerical equality implies that the current and charge carry the same amount of energy, an effect that is discussed further in connection with Fig. 9.

(b) The amplitudes of the I and Qc pulses decay as they propagate outwards towards the ends of the wire dipole.

(c) The uniformly spaced pulses are apparently moving at a constant speed.

The latter observation is confirmed in Fig. 5 where a best-fit straight line is shown on a time-distance plot for the 599 segment dipole based on the peaks of the rightward-propagating pulses some of which are included in Fig. 6. There is no apparent discontinuity effect upon to end reflection. The average speed of these pulses as determined from the best-fit line is 2.9868×10^8 m/sec, within $1/3\%$ of the 3×10^8m/sec input in TWTD. Time on this plot is measured from the pulse at 367 time steps on Fig. 4.

The electric far fields normal to dipole antennas of variable lengths as a function of time is plotted in

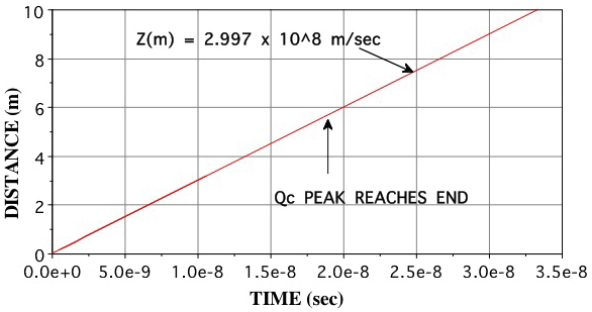

Fig. 5. A time-distance plot for the data of Fig. 4 using additional time steps and a best-fit straight line.

Fig. 6 up to the time just beyond the time of the first end reflection of the outward propagating pulses. This plot reveals three different types of radiation. The first is due to the initial charge acceleration caused by the center-located voltage pulse. The second radiation pulses are due to the I/Qc pulses reaching the wire ends and where they reflect and reverse direction. The source-caused radiation pulse is about half that of the L = 99 segment wire, due to the fact that the source imparts a speed of c to the outward-propagating pulses while end reflection involves a speed change of $2c$. The end-reflected peaks decrease with increasing dipole lengths due to an intermediate, or traveling-wave reflection effect that causes the decreasing magnitude of the reflected pulses.

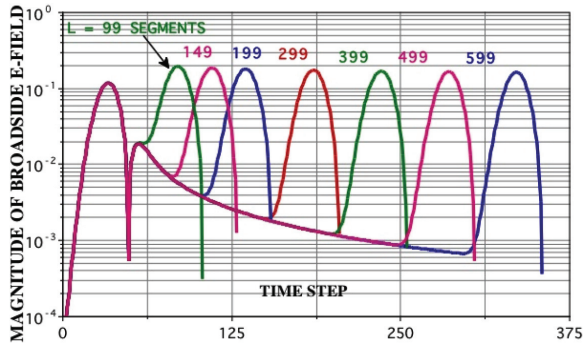

Fig. 6. The magnitude of the relative broadside radiated electric fields in for various dipole lengths in 0.01 m long segments (Fig. 3.4 from [10]).

This reflection is continuous as the I/Q_c pulses propagate down the dipole arms due to the wave impedance of a constant-radius wire varying with distance from the feedpoint as shown by the admittance in Eq. (10) [13]. This would not occur if the arms of the dipole were cones instead, resulting in a length-independent wave impedance as shown in Eq. (11) [14]. The wave-impedance reflection is also responsible for the decreasing end radiation exhibited in Fig. 6.

$$Y_W(z) \sim \frac{4\pi}{\eta_o}\left[\ln\left(\frac{2z}{k_o a^2 \Gamma}\right) + \frac{i\pi}{2}\right]^{-1}, \tag{10}$$

$$Y_C = \frac{I(r)}{V(r)} = \frac{\pi}{\eta_o}\left[\cot\left(\frac{\alpha}{4}\right)\right]^{1}. \tag{11}$$

A plot of this propagation-caused radiated electric field is presented in Fig. 7 normalized to the amount of charge reflected per time step. The latter is obtained by integrating the amount of charge in the outgoing pulse at each time step to compute how much has been reflected. This plot is somewhat jagged since it involves the subtraction of two nearly equal numbers. Nevertheless, the match between the electric field and the reflected charge is on average within a few percent.

It's interesting to compute the numerical ratio between Qc and the corresponding radiated electric field for these 3 radiation mechanisms, defined here as an "Acceleration Factor" (AF). This is demonstrated in Fig. 8 where the charge time variation multiplied by its AF is plotted with its associated radiated E-field. Although the AF values must be considered approximate as their computation is somewhat imprecise, the endreflected AF_{E} is estimated at 1.95 times that for the source AF_{S}, or about 2.5% different from the value of 2 that might be expected. On the other hand the propagation AF_{P} is only 1.21 times that for the source. This might be inferred to be so much less than 2 because the reflection mechanism is "smoother" than reflecting from an open wire end.

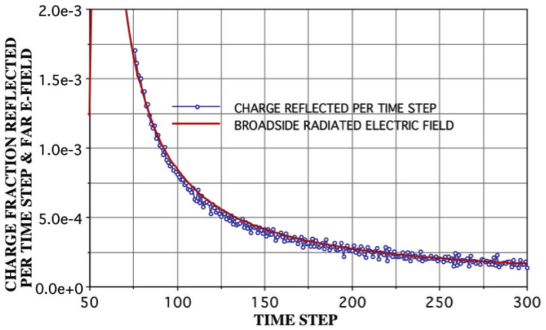

Fig. 7. The time variation of the traveling-wave radiated electric field and the reflected charge steps (Fig. 13 from [16]).

The acceleration factors presented in Fig. 8 and using the equivalent approach for some other radiation mechanisms are summarized for reference in Table 1. While computing their values may be somewhat uncertain in an absolute sense, their ratios may be useful for comparing their relative influences in producing a radiated field.

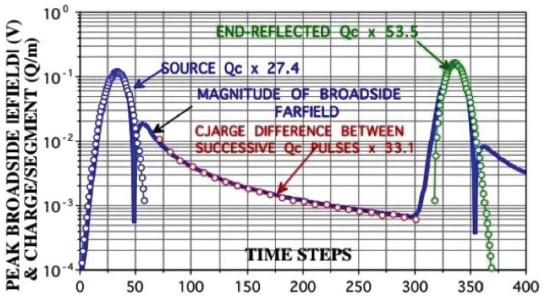

Fig. 8. A combined plot of the propagation, source and end-reflected broadside E-field magnitudes and the respective time varying accelerated charges that produce them (Fig. 12 (b) from [10]).

Table 1: AF values for various radiation types

Radiation Type	**Acceleration Factor**
Source: AF_S	27.4
Variable Wire Radius: AF_{WR}	29.2
Right-Angle Bend: AF_B	47.0
Propagation: AF_P	33.1
Resistance Load: AF_{RL}	59.4
End Reflection: AF_E	53.5

A different way of demonstrating radiation effects for the 599-segment dipole is illustrated in Fig. 9. The current energy $W_I(t)$ and charge energy $W_{Qc}(t)$ measures integrated over the dipole as a function of time are obtained from

$$W_i(t) = \int_0^1 I^2(x,t)dt, \tag{12}$$

and

$$W_{Qc}(t) = c^2 \left[\int_{-\frac{L}{2}+\Delta}^{\frac{L}{2}-\Delta} Q^2(x,t) + \frac{1}{3}\int_{-\frac{L}{2}}^{-\frac{L}{2}+\Delta} Q^2(x,t)dx + \frac{1}{3}\int_{\frac{L}{2}-\Delta}^{\frac{L}{2}} Q^2(x,t)dx \right]. \tag{13}$$

The Qc energy computation in Eq. (13) treats the end segments of the dipole differently to account for the end current going to 0 on those segments.

The current, charge and total energy measures plotted as a function of time in Fig. 9. The initial energy buildup is dominated by the charge but after about 50 time steps the current and charge energies become equal, decaying smoothly together until the first end reflection. These effects are due to the source and propagation radiations. At each end reflection the current energy falls to 0 when all of the energy is due to the charge with a sharp decrease in the total energy. The opposite effect occurs when the end-reflected pulses meet at the center feedpoint with an almost imperceptible loss of the total energy.

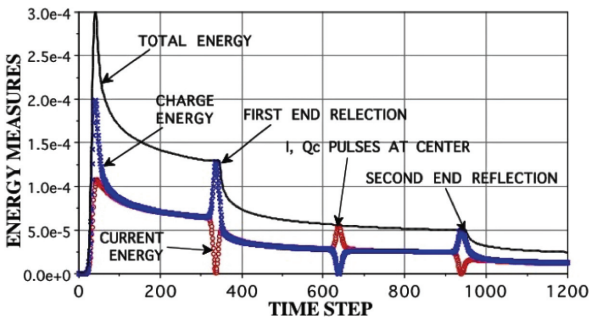

Fig. 9. The current, charge and total energy measures as a function of time for an impulsively excited straight wire as a dipole antenna (Fig. 4.6 from [10]).

Differentiating the total energy of Fig. 9 with respect to time is useful to show the rate of the total energy loss as displayed in Fig. 10. These rate curves are rather noisy in appearance as this again involves the difference of nearly equal numbers, an effect that increases as the loss rate decreases by more than 2 orders of magnitude. It's interesting to see that the loss rate is quite similar in each sequence. There is, however, between the first and second end reflections a slight "bump" of about 2 during the time interval when the charge pulses overlap as they pass through the center feedpoint.

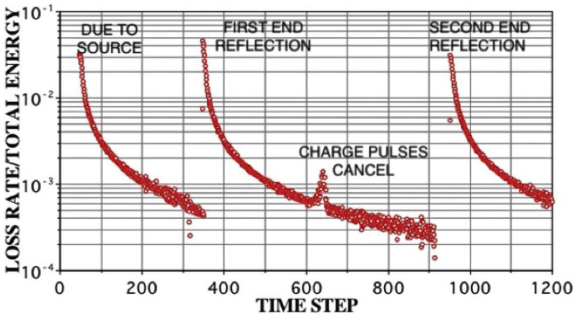

Fig. 10. The differentiated total energy plot of Fig. 6 illustrating the doubling of the radiation-loss rate as the counter-propagating charge pulses meet at the center of the dipole (Fig. 4.8 from [10]).

This phenomenon occurs because the propagation of the counter-propagating-pulse radiation becomes coherent or additive over the far-field sphere. This effect is similar to what happens when 2 one-watt, frequency-domain point sources are brought together, the result of which is shown in Fig. 11. Their total radiated power increases in an oscillatory fashion as they are moved closer together until it doubles at zero separation.

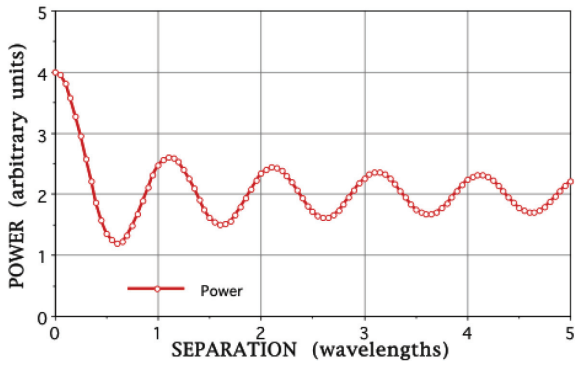

Fig. 11. The power radiated by 2 unit-amplitude point sources as a function of their separation in wavelengths (Fig. 1 (b) from [17]).

The current, charge and total energy measures as a function of time for a 1.99 m straight wire excited by a normally incident impulsive plane wave is shown in Fig. 12. There is a periodic interchange between the charge and current energies as they each pass through successive oscillations of zero energy. The current (red) and charge (blue) distributions at 9 time samples to demonstrate this effect are exhibited in Fig. 13.

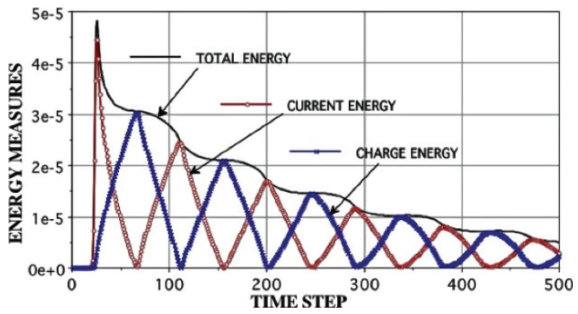

Fig. 12. The current, charge and total energy measures as a function of time for an wire impulsively excited by a normally incident plane wave dipole (Fig. 4.18 from [10]).

The frequency-domain normalized Poynting vector along a 10-wavelength dipole obtained from $\mathrm{Re}\left[(IQ^{*}c)/2\right]$ is plotted in Fig. 14. It is somewhat analogous to the energy-measure time-domain result of Fig. 9 over the time of the exciting source turn on to the first end reflection. Differentiating this result yields the rate of radiated power-loss as a function of position in Fig. 15 for comparison with the energy-loss rate in the time domain of Fig. 10 [15]. Whereas the time-domain energy loss is monotonic except for the charge-pulse overlap, that for the frequency domain is lobed because the latter supports a standing-wave current.

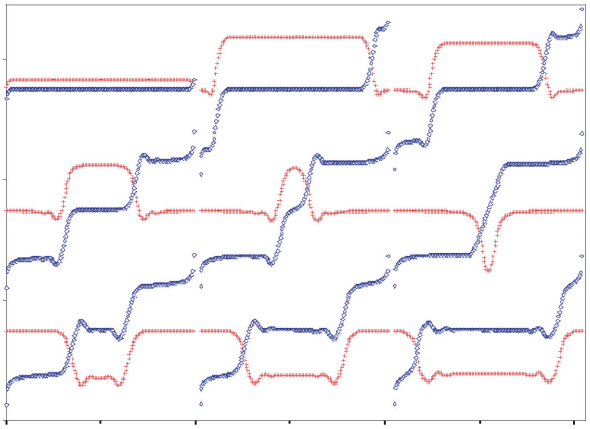

Fig. 13. The current (red) and charge (blue) distributions at 9 time samples for an impulsive plane wave at normal incidence scattering from a straight wire reading left to right from the top dipole (Fig. 4.16 from [10]).

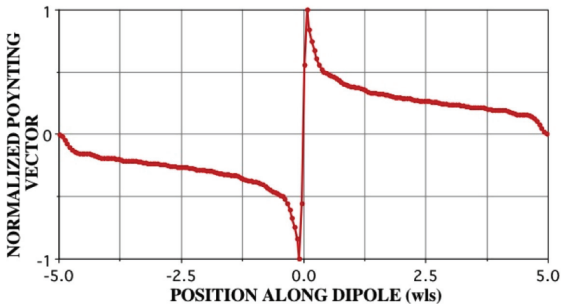

Fig. 14. The on-surface Poynting vector obtained from NEC for a center-fed, 10-wavelength dipole with power flow to the left negative and to the right positive (Fig. 5 from [18]).

A circular wire loop should be expected to exhibit a higher energy loss versus distance than a straight wire because the charge acceleration is greater than the dipole due to the loop's curvature. This effect is illustrated in Fig. 16 where Qc pulses are shown in the time domain at 100 time-step intervals on a dipole and loop 1,200 segments long. The loop peak is at time step 600 is incomplete because it is partially obscured by the counter-propagating pulse meeting it at the side opposite the feedpoint. The dipole is excited at segment 49 to avoid the first end reflection. Note that the loop pulses are moving slightly faster than those on the dipole because their associated electric fields straight-line path is shortened by the loop curvature.

In a fashion similar to Fig. 9 for the dipole, the current, charge and total energies for the circular loop are presented in Fig. 17. There are two especially interesting features to be seen here as the current and total energies asymptotically approach constant values while the

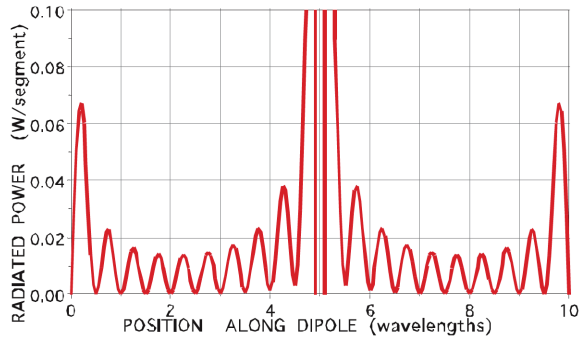

Fig. 15. The differentiated Poynting-vector of Fig. 14 for a 10 -wavelength dipole (Fig. 6.8 (a) from [10]).

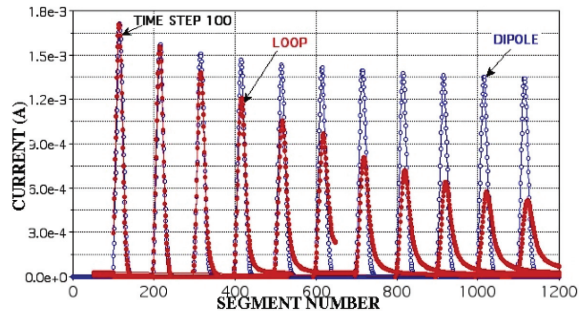

Fig. 16. Comparison of the Qc pulses on 1,200 segment dipoles and circular loops at 100-segment time steps (Fig. 3.5 (a) from [10]).

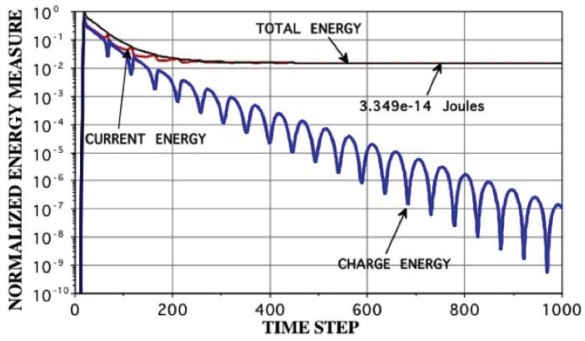

Fig. 17. The current, charge, and total energies as a function of time step for a loop of 5 m (100 segment) circumference and wire radius of 0.02 m as a function the time step (Fig. 5.2 from [10]).

charge energy decreases towards zero in an oscillatory fashion. The oscillatory decay it exhibits occurs because each time the opposite-signed, oppositely propagating charge pulses meet moving around the loop, they cancel to produce alternating minima because their accelerations are radially inward and thus cancel. The charge energy eventually becomes zero as the loop radiates the time-dependent energy deposited by the impulsive excitation.

This results in a uniform, non-radiating, late-time current I_o and charge neutrality around the loop. Interestingly, this current can be used to compute the inductance of the loop [16]. Actually, this is possible for literally any closed loop that can be modeled using TWTD or a similar computer model. Note the contrast with the late-time current and charge on an open object such as a dipole where both decay to zero as charge neutrality is restored.

IV. CONCLUSION

The results presented here demonstrate how EM radiation is caused by various kinds of impulsive charge acceleration for simple wire geometries using a time-domain computer model derived from the Maxwell Equations. The excitation, either a local voltage for an antenna or a distributed electric field for a scatterer, causes the initial acceleration. This excitation essentially begins the process and results in an effective speed increase of c for the charge induced by the applied electric fields. Other various reflection mechanisms subsequently exhibit somewhat different acceleration effects and produce speed changes of $2c$, due to reversing the direction of the charge motion. These include propagation radiation because of the location-dependent wave impedance of a uniform-radius wire. Other reflection radiation is caused by open wire ends, changes in wire radius, sharp bends, smooth curves and impedance loads. These reflection accelerations are due to the electric fields that are terminated by charge on the wire and whose speed must match that of the fields in the medium

APPENDIX

The following information is provided for readers who might like to perform similar computer "experiments" using NEC or TWTD. The latest version of NEC, 4.2, continues to be distributed by Lawrence Livermore National Laboratory. Information concerning its availability and cost can be obtained at "https://softwarelicensing.llnl.gov/product/nec-v42".

The TWTD code in a pdf Fortran file is available from the author via email at no cost, along with a user's manual. Contact me at e.miller@ieee.org for any questions that you might have. Note that both codes include a feature called FARS (Far-field Analysis of Radiation Sources) [10] for determining the spatial distribution of radiated power from a PEC object. FARS was not included above because it wasn't necessary to for this introductory presentation.

REFERENCES

[1] A. Liénard, "Champ électrique et magnétique produit par une charge électrique concentrée en un point et animée d'un movement quelconque," *L'éclairage Électrique*, vol. 16, pp. 16–21, 1898.

[2] E. Wiechert, "Elektrodynamische elementargesetze," *Ann. Phys*., vol. 4, pp. 667–689, 1901.

[3] K. Yee, "Numerical solution of initial boundary value problems involving Maxwell's equations in isotropic media," *IEEE Transactions on Antennas and Propagation*, vol. 14, no. 3, pp. 302–307, 1966.

[4] J. A. Landt, E. K. Miller, and M. L. Van Blaricum, *WT-MBA.LL1B: A Computer Program for the Time-Domain Response of Thin-Wire Structures*, Livermore, CA: Lawrence Livermore Laboratory, 1974.

[5] E. K. Miller, A. J. Poggio, and G. J. Burke, "An integro-differential equation technique for the time-domain analysis of thin-wire structures. Part I: The numerical method," *Journal of Computational Physics*, vol. 12, pp. 24–48, 1973.

[6] R. F. Harrington, *Field Computation by Moment Methods*. New York, NY: Macmillan, 1968.

[7] E. K. Miller, "Computational electromagnetics," in *The Electrical Engineering Handbook*, Richard C. Dorf, Ed. Boca Raton, FL: CRC Press, pp. 1028–1049, 1993.

[8] G. J. Burke, E. K. Miller, and A. J. Poggio, "The numerical electromagnetics code (NEC) – A brief history," in *2004 IEEE Int. Antennas Propagat. Symp. Dig.*, vol. 42, pp. 2871–2874, June 2004.

[9] G. S. Smith, *Classical Electromagnetic Radiation* Cambridge: Cambridge University Press, 1997.

[10] E. K. Miller, *Charge Acceleration and the Spatial Distribution of Radiation Emitted from Antennas and Scatterers*. London: Institution of Engineering and Technology, 2023.

[11] B. Cabrera, *Physics Simulations II: Electromagnetism, Academic Version*. Santa Barbara, CA: Intellimation Library for the Macintosh, 1990.

[12] B. Cabrera and E. K. Miller, "Macintosh Movies for Teaching Undergraduate Electricity and Magnetism," in *1986 International IEEE APS Symposium*, Philadelphia, PA, 9–13 June 1986.

[13] J. Bach Anderson, "Admittance of infinite and finite cylindrical metallic antenna," *Radio Science*, vol. 3, no. 6, pp. 607–621, 1968.

[14] C. A. Balanis, *Antenna Theory: Analysis and Design*. New York: Harper & Row Publishers, 1982.

[15] E. K. Miller and G. J. Burke, "A multi-perspective examination of the physics of electromagnetic radiation," *Applied Computational Electromagnetics Society (ACES) Journal*, vol. 16, no. 3, pp. 190–201, 2001.

[16] E. K. Miller, "Comparison of the radiation properties of a sinusoidal current filament and a pec dipole of near zero radius," *IEEE Antennas and Propagation Society Magazine*, vol. 48, no. 4, pp. 37–47, Aug. 2006.

[17] E. K. Miller, "Time-Domain Far-Field Analysis of Radiation Sources and Point-Source Coherence," *IEEE Antennas and Propagation Society Magazine*, vol. 54, no. 2, pp. 100–108, Apr. 2012.

[18] E. K. Miller, "The differentiated on-surface Poynting vector as a measure of radiation loss from wires," *IEEE Antennas and Propagation Society Magazine*, vol. 48, no. 6, pp. 21–32, Dec. 2006.

Edmund K. Miller earned a B.S. (EE) in 1957 from Michigan Technological University (then known as Michigan College of Mining and Technology. His graduate work was done at the U. of Michigan, with an M.S. (Nuclear Engineering) in 1958, an M.S. (EE) in 1963 and a Ph.D. (EE) in 1965. His working career included 4 universities (Michigan Tech 1958–59, U. of Michigan 1959–68, Kansas U. 1985–1987 and Ohio U.1994–95); 3 companies (MBAssociates (1969–71, Rockwell International Science Center 1985–1987, and General Research Corporation (1987–1988); and 2 National Laboratories (Lawrence Livermore (1971–85 and Los Alamos (1989–1993). He has been actively retired since 1995 and has lived in Lincoln, CA since 2003.

His involvement in Computational Electromagnetics began in 1959 and continues to the present. He wrote a regular column "PCs for AP and Other EM Reflections" from 1985 to 2000 for the IEEE Antennas and Propagation Society. In addition to his nearly 200 journal articles and various society proceedings he edited the book "Time Domain Measurements in Electromagnetics" in 1986 and co-edited the IEEE reprint volume "Computational Electromagnetics: Frequency-Domain Moment Methods". He wrote the 2023 book "Charge Acceleration and the Spatial Distribution of Radiation Emitted by Antennas and Scatterers" that summarized his work on radiation physics over the years, and another about to be published "Model-Based Parameter Estimation in Electromagnetics".

Dr. Miller was the first president of ACES, of which he was a founding member, and is a Fellow of the IEEE and ACES.

Distributed Heterogeneous Conformal Meter-Wave Phased Array Using Characteristic Mode for Airship Platform

Yuhao Feng and Zijian Yang

Department of Electronic Science and Engineering
University of Electronic Science and Technology of China, Chengdu 611731, China
yuhao.feng@uestc.edu.cn, 923679355@qq.com

Abstract – This paper presents an advanced characteristic mode (CM)-based synthesis and optimization framework for designing conformal meter-wave phased array antennas on airship platforms. Unlike previous studies that focused on planar or small UAV (Unmanned Aerial Vehicle) surfaces, this work extends CM analysis to a large-scale, irregular, fully metallic airship structure in the low-frequency band. The CMs of the airship body are analyzed to extract dominant modal currents and field distributions. To achieve controllable beam scanning and polarization characteristics, a decomposition-based multi-objective evolutionary algorithm (MOEA/D) is integrated with the modal synthesis process, enabling physics-informed optimization of co-/cross-polarization energy and sidelobe level. Guided by the synthesized modal currents, distributed heterogeneous coupling elements (CEs) are conformally arranged on the platform. The fabricated 1:40 scale model demonstrates a $\pm 60^{\circ}$ beam scanning range and a measured gain exceeding 10 dBi with over 80% radiation efficiency, in good agreement with simulations. The proposed method bridges CM theory and practical conformal array realization, providing a generalized approach for large-scale, platform-integrated antenna design.

Index Terms – Characteristic mode (CM), distributed heterogeneous array, meter-wave, platform-integrated antenna.

I. INTRODUCTION

As a highly maneuverable platform, the aircraft carries an electronic system that can communicate with other end users at various weather, terrains, and visibility conditions [1]. To enhance gain and electronic beam scanning, antenna arrays, instead of single-element antennas, are commonly installed on the aircraft platform [2, 3]. However, designing integrated phased array antennas for aircraft presents challenges. Firstly, meter-wave phased array radar is effective for stealth and long-range detection [4, 5]. Yet, the resonant length of meter-wave antennas equals their wavelength, making it challenging to form arrays on platforms with limited space [6]. Secondly, larger antennas negatively impact aerodynamics, stability, and increase the radar cross-section (RCS) of the platform. Thirdly, platforms with complex electromagnetic materials may experience coupling issues, affecting radiation performance.

Designing conformal antenna arrays on space-constrained platforms is challenging. Current integration of platforms and antennas faces deficiencies, with electromagnetic full-wave analysis being the predominant optimization method [7]. While joint simulation reduces development time, it has limited physical explanations for antenna radiation mechanisms. Addressing these challenges, the low-frequency platform-integrated antenna design, based on the characteristic mode (CM) theory, offers advantages.

For instance, in a shipboard antenna system embedded in the platform [8], CMs synthesize radiating currents for a desired radiation pattern. Designs with multiple beam directions and consideration of polarization information offer versatile applications. In examples like [9] and [10], three beams with different directions on an aircraft platform were synthesized, and [11] achieved the switching ability of four angle beams. While some designs, like [12], focus on using polarization characteristics for incident wave detection in aircraft platforms, beam scanning is limited. In [13], coupling elements (CEs) on both sides of the platform allow $\pm 45^{\circ}$ beam scanning, considering polarization characteristics and beam switch ability during CM analysis and pattern synthesis. However, not all aircraft platforms have sufficient regular edge structures for placing CEs.

Compared with existing CM-based antenna designs [9–13], which primarily target local or planar aircraft structures, the proposed work introduces a distributed heterogeneous conformal array framework suitable for large, irregular, and low-frequency airship platforms. First, the CM theory is extended to analyze and synthesize the global radiation modes of a fully metallic airship body, enabling efficient mode selection and field synthesis over complex surfaces. Second, a

Submitted On: August 29, 2025
Accepted On: October 26, 2025

https://doi.org/10.13052/2025.ACES.J.401102

decomposition-based multi-objective evolutionary algorithm (MOEA/D) is integrated with the modal analysis to achieve physics-informed optimization of co- or cross-polarization energy, beam direction, and sidelobe control. Third, a practical conformal coupling-line excitation structure is designed according to the synthesized modal currents, realizing an experimentally validated $\pm 60^\circ$ beam scanning with over 10 dBi gain and 80% radiation efficiency. These advancements bridge the gap between theoretical CM analysis and the engineering implementation of large-scale conformal phased arrays at meter-wave frequencies.

CM-based platform-integrated antenna research has been extensively applied in low-frequency aircraft and vehicular systems. For instance, Wang et al. [19] proposed a CM-based multiantenna system in the HF band (8–28 MHz) for aircraft platforms. Their approach achieved omnidirectional and directional radiation patterns by combining dominant modes and manually selecting exciter locations, but it was limited to discrete-frequency operation without beam scanning capability.

Subsequently, Wang et al. [20] extended this framework to the VHF band ($\approx$100 MHz) and demonstrated switchable-beam array synthesis using a MOEA/D. Although effective for low-frequency flush-mounted metallic aircraft, their design required more than 10 exciters and did not consider aerodynamic constraints or scalable array realization.

In contrast, the present work proposes a closed-loop methodology that integrates platform CM analysis, multiobjective optimization, and distributed CE excitation synthesis. The use of CMs as a "hidden aperture" enables conformal array beam scanning at meter-wave frequencies without modifying the airship geometry. Furthermore, the proposed framework maintains modal continuity, physical scalability, and aerodynamic compatibility, representing a fundamental advancement beyond the HF/VHF fixed-aperture designs in [19, 20].

This article discusses designing integrated antennas for low-frequency airship platforms. Airships are ideal for long-term use in communication systems, weather forecasting, surface remote sensing, and aerial monitoring due to their cost-effectiveness.

II. RADIATION PATTERN SYNTHESIS

We aim to streamline analysis of the airship in communication systems, focusing on a distributed heterogeneous array design. Treating the airship as a fully metallic body based on electromagnetic theory, we propose an antenna for a simplified model with dimensions of 20.6×8.384×5.68 m (L×W×H), as illustrated in Fig. 1. To meet remote detection requirements, we design a conformal array with high gain at 100 MHz. In specific scenarios, the array must generate a horizontally

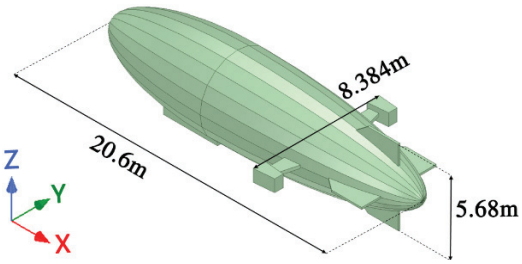

Fig. 1. Geometry of a simplified airship model.

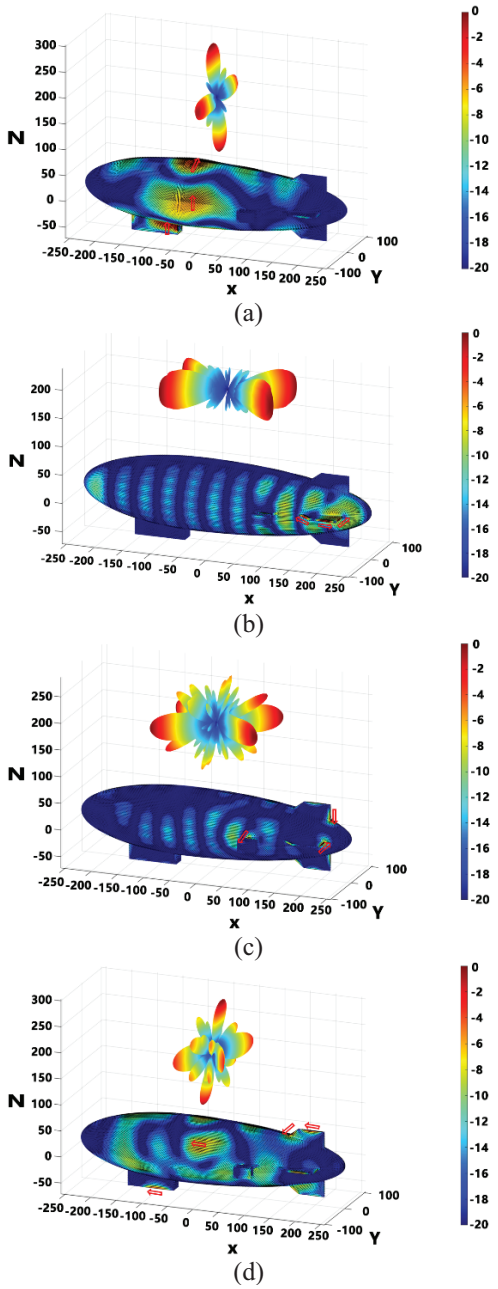

Fig. 2. Normalized characteristic fields and currents of the airship at 4 GHz (units: dB). (a) 1st mode. (b) 11th mode. (c) 31th mode. (d) 61th mode.

polarized switchable beam within a designated range of the XOY plane. For practical experimental verification, we reduce the airship model to a 1:40 scale, and the working frequency is adjusted to 4 GHz.

A. Characteristic modes of the airship

For any metal conductor, distinct CM currents exist on its surface, and their distribution is an intrinsic property of the conductor [14, 15]. These CMs are independent of the excitation source and are solely determined by the shape, size, and materials of the electromagnetic structure. This independence offers a clear physical basis for investigating the inherent radiation mechanism.

It should be noted that in equation (1), $\mathbf{R}$ and $\mathbf{X}$ denote the symmetric and antisymmetric parts of the impedance matrix $\mathbf{Z}$, rather than its strict real and imaginary components. This definition follows the classical Hermitian decomposition of the impedance operator proposed by Harrington and Mautz and later applied to microstrip structures by Angiulli et al. [16].

First, we decompose the impedance matrix $\mathbf{Z}$ into a combination of Hermitian real and imaginary parts:

$$\mathbf{Z} = (\mathbf{R} + j\mathbf{X}). \tag{1}$$

Among them are:

$$\mathbf{R} = \frac{\mathbf{Z} + \mathbf{Z}^*}{2}, \tag{2}$$

$$\mathbf{X} = \frac{\mathbf{Z} - \mathbf{Z}*}{2j}. \tag{3}$$

If the impedance matrix $\mathbf{Z}$ is symmetric, then both $\mathbf{R}$ and $\mathbf{X}$ are real symmetric matrices, and $\mathbf{R}$ is positive semidefinite. Consider the following weighted eigenvalue equation:

$$\mathbf{Z}\mathbf{J}_n = \upsilon_n \mathbf{W}\mathbf{J}_n, \tag{4}$$

where $\mathbf{J}_n$ is the eigenvector, υ_n is the eigenvalue, and $\mathbf{W}$ is a constructed matrix that diagonalizes the impedance matrix $\mathbf{Z}$ on the left. It is easy to see that as long as $\mathbf{W}$ is a symmetric matrix, the requirement is met. However, to ensure orthogonality in the far field of the mode, $\mathbf{W} = \mathbf{R}$ and $\upsilon_n = 1 + j\lambda_n$ is chosen. Substituting into equation (4) get equation (5). The CMs of a perfectly electrically conducting (PEC) body can be determined through a generalized eigenvalue equation [17]:

$$\mathbf{X}\mathbf{J}_n = \lambda_n \mathbf{R}\mathbf{J}_n. \tag{5}$$

Here $\mathbf{J}_n$ and λ_n are characteristic current and eigenvalue of the nth CM, n is the index of the order, and $\mathbf{R}$ and $\mathbf{X}$ are the real and imaginary parts of a method of moment (MoM) impedance matrix calculated for the electric field integral equation (EFIF) [18].

Figure 2 displays normalized characteristic electric field and characteristic current distribution diagrams for four randomly chosen significant modes (mode 1, mode 11, mode 31, and mode 61) out of the 90 identified modes. In mode 1, dominant currents spread in four directions along both sides of the pod and the airship gasbag. Mode 11 exhibits maximum transverse currents along the three edges of the two tail fins. Mode 31 resonates along the edges of the tail and the propulsion unit. Mode 61's maximum current is distributed across multiple structures.

To ensure that only physically meaningful modes contribute to pattern synthesis, a quantitative criterion was used to define "significant" modes. The modal significance (MS) is expressed as:

$$\mathrm{MS} = 1/|1 + j\lambda_n|, \tag{6}$$

where λ_n is the eigenvalue of the nth mode. Modes with $MS_n > 0.1$ and radiation efficiency exceeding 80% were selected as significant modes. In total, 90 modes were calculated, from which four representative significant modes (1st, 11th, 31st, and 61st) were extracted for optimization and synthesis. This formal selection criterion aligns with the classical CM theory proposed by Harrington and Mautz [18], ensuring both physical interpretability and numerical robustness of the optimization process.

For exciting a specific mode, a suitable current excitation should align with the characteristic current distribution. Modes 1 and 11 have radiation patterns with four beams of nearly equal amplitude, but their distribution planes differ (XOZ for mode 1 and XOY for mode 11). The lobes of modes 31 and 11 are relatively close, and the maximum radiation direction of mode 61 is also close to that of mode 1. However, these higher-order modes exhibit high sidelobe levels (SLL), as predicted from their current distributions. The selected modes are representative, and other significant modes lack scanning beams in their characteristic electric fields. Although a single mode is insufficient, their characteristic fields provide sufficient degrees of freedom for scanning pattern synthesis.

Table 1: Modal significance for a metal platform's first four modes. Mode 1 resonates at 4 GHz, with no other significant modes at this frequency

Mode No.	**1**	**2**	**3**	**4**	**5**
MS	0.898951	0.294527	0.189356	0.136325	0.0504503

B. Radiation pattern synthesis

Conventionally, the cost function of the multi-objective optimization algorithm is set according to the

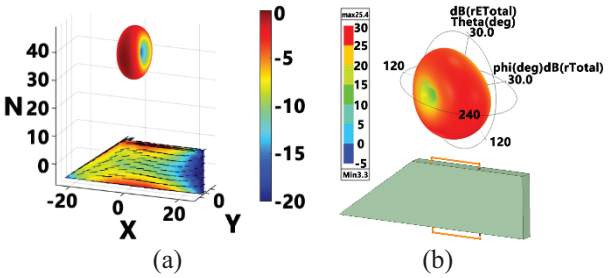

(a) (b)

Fig. 3. (a) Characteristic electric field and characteristic current of the significant mode of a metal platform. (b) Schematic diagram of significant mode and electric field of metal platform excited by half loop antenna.

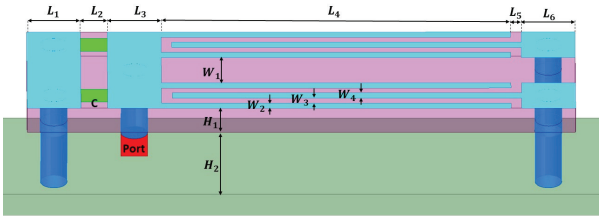

Fig. 4. Top view of couple-line CE integrated on the platform.

parameters of desired radiation patterns. In this design, to optimize the beam direction and the energy distributions, the following three cost functions are set:

$$f_1(\boldsymbol{\alpha}^{(k)}) = |\theta_{co}^{\max} - \theta_{\text{desired}}^{\max}| + |\varphi_{co}^{\max} - \varphi_{\text{desired}}^{\max}|, \quad (7)$$

$$f_2(\boldsymbol{\alpha}^{(k)}) = -\frac{\iint_{S_{MR}} |\mathbf{E}_{co}(\theta,\varphi)|^2 ds}{\iint_{S_\infty} |\mathbf{E}_{\text{total}}(\theta,\varphi)|^2 ds}, \quad (8)$$

$$f_3(\boldsymbol{\alpha}^{(k)}) = \frac{\iint_{S_{MR}} |\mathbf{E}_{\text{cross}}(\theta,\varphi)|^2 ds}{\iint_{S_\infty} |\mathbf{E}_{\text{total}}(\theta,\varphi)|^2 ds}. \quad (9)$$

Here $\boldsymbol{\alpha}^{(k)} = \{\alpha_1^{(k)}, \ldots \alpha_i^{(k)}, \ldots \alpha_N^{(k)}\}$ is the complex weighting coefficient of the ith significant mode in the kth iteration of the MOEA/D. The magnitude and phase of $\boldsymbol{\alpha}^{(k)}$ $(1 \le i \le \mathrm{N})$ are in the range of [0, 1] and [0, 2π], respectively. $(\theta_{\text{desired}}^{\max}, \varphi_{\text{desired}}^{\max})$ is the elevation and azimuth angle of the maximum beam pointing of desire radiation $\theta_{co}^{\max}$ and $\varphi_{co}^{\max}$ is the elevation and azimuth angle of the maximum beam pointing of co-polarized field components for the complex weighting coefficient $\boldsymbol{\alpha}^{(k)}$. The beam pointing of the synthesized pattern is constrained by the cost function $f_1(\boldsymbol{\alpha}^{(k)})$. By changing the constants, optimization at different scanning angles can be achieved. The cost function $f_2(\boldsymbol{\alpha}^{(k)})$ is the ratio of the co-polarization energy in the main lobe range (S_{MR}) to the total energy on the entire sphere (S_∞), to ensure that the energy is concentrated in the set range as much as possible. Since the MOEA is to optimize

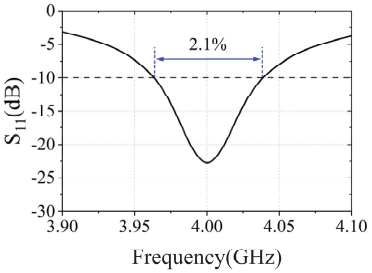

(a)

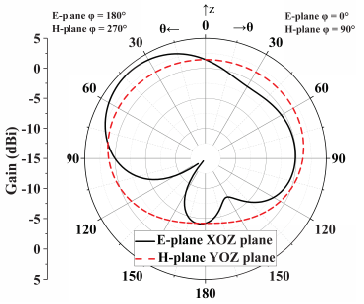

(b)

Fig. 5. Couple-line CE: (a) reflection coefficient and (b) radiation pattern.

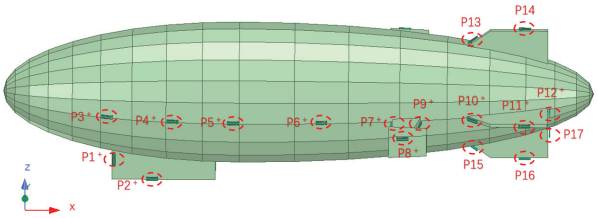

Fig. 6. Excitation locations over the airship platform.

each objective to the minimum value, a negative sign is added before the ratio. The cost function $f_3(\boldsymbol{\alpha}^{(k)})$ is defined to minimize the ratio of the cross-polarization energy in the main lobe range (S_{MR}) to the total energy on the entire sphere (S_∞).

CM analysis and modal impedance extraction were conducted using an in-house C++ MoM solver compiled with Code::Blocks (MinGW64), following the workflow described in the program instruction manual, where the HFSS-derived mesh model (.nas) was imported and solved in Release mode for improved numerical stability. The subsequent beam synthesis optimization employed a C++ implementation of the MOEA/D multi-objective differential evolution algorithm, targeting main-lobe steering accuracy, polarization purity, and sidelobe suppression, while post-processing and visualization were performed in MATLAB. Each optimization run included 300 generations with about 178500 fitness evaluations, executed on a workstation equipped with an 11th Gen Intel Core i7-1165G7 CPU (2.80 GHz, 4 cores), 16 GB RAM, and Intel Iris Xe Graphics,

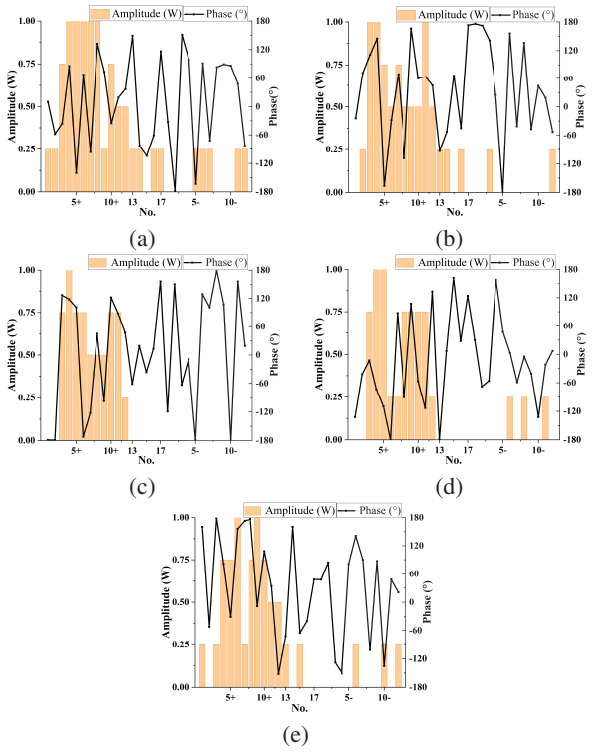

Fig. 7. Excitation amplitudes and phases for couple-line CE at the locations P1-P29 (No.1-29): (a) $-30°$, (b) $-15°$, (c) $0°$, (d) $15°$, (e) $30°$.

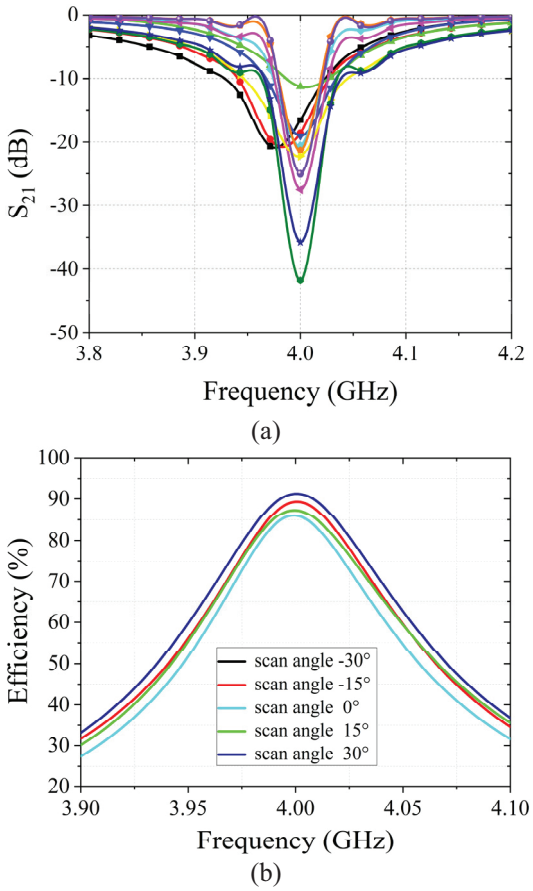

Fig. 8. (a) S_{21} in the array environment active reflection coefficient at scan angle of $0°$. (b) Radiation efficiency of antenna array at different scan angles.

requiring a total runtime of approximately 57574 s ($\approx$16 h). This configuration confirms that the proposed CM-MOEA/D closed-loop framework can be efficiently implemented on a standard PC.

Based on the cost function established by the MOEA/D, the characteristic field and current component obtained from the CM analysis platform can be utilized to solve at the current scanning angle. Subsequently, the solver produces a set of Pareto-optimal solutions for the synthesized field and current solution.

III. DISTRIBUTED HETEROGENEOUS CONFORMAL ARRAY DEVELOPMENT

This paper focuses on the current distribution of the synthesized mode as the main basis for designing a distributed heterogeneous conformal array for an airship platform. The design and arrangement of CEs will be based on this distribution, and MOEA/D will be used to obtain the normalized excitation amplitude and phase of multiple CEs at various scan angles. This section also presents the measured results.

A. Coupling elements design

The excitation structure can stimulate single mode or synthesized mode current using electric field or magnetic field induction methods. The metal platform, based on the airship is tail structure, demonstrates this. Figure 3 (a) shows characteristic fields and currents for the platform's dominant mode at 4 GHz, with currents mainly along the platform's longest edges. In Fig. 3 (b), a half-ring antenna is positioned vertically along the platform's long edge, with a 0.066 pF capacitor at the port. The electric field excited by inductive coupled element (ICE)aligns well with the characteristic electric field. It is also important to mention that the CM isn't linked to the external excitation source. Thus, CEs don't need to be included in the airship is CM analysis. However, the CEs' physical size should be minimized to avoid a significant impact on the characteristic value and electric field of the airship.

The airship platform structure, including the airbag, must ensure continuity. Embedded schemes are avoided in the design of CEs, and conformal requirements are met through low profile and electrically small size. The interdigital coupling line's deformation structure is based on the classical half-ring CE, as shown in Fig. 4.

Table 2: Performances comparison for proposed airship-based CM-MOEA/D framework with existing CM-based designs, showing a wider $\pm 60^\circ$ continuous scanning range, lower sidelobes, and improved polarization control compared with prior VHF and side

Ref.	Operating Band	Number of Effective Modes	Beam Scanning Range	Radiation Efficiency	Sidelobe Level (SLL)
[19]	VHF band (118–137 MHz)	3–4 dominant modes	$\leq \pm 45^\circ$ discrete beams	75–80 % (main beam)	-10 dB typical
[20]	2.4 GHz WLAN band	2 magnetic modes	Fixed broadside dual-pol radiation	70–78 %	-15 dB (E/H planes)
This Work	Meter-wave (100 MHz, scaled to 4 GHz model)	12 dominant modes	$\pm 60^\circ$ continuous scan with stable gain	>85 % (full scan)	<-13 dB across scan

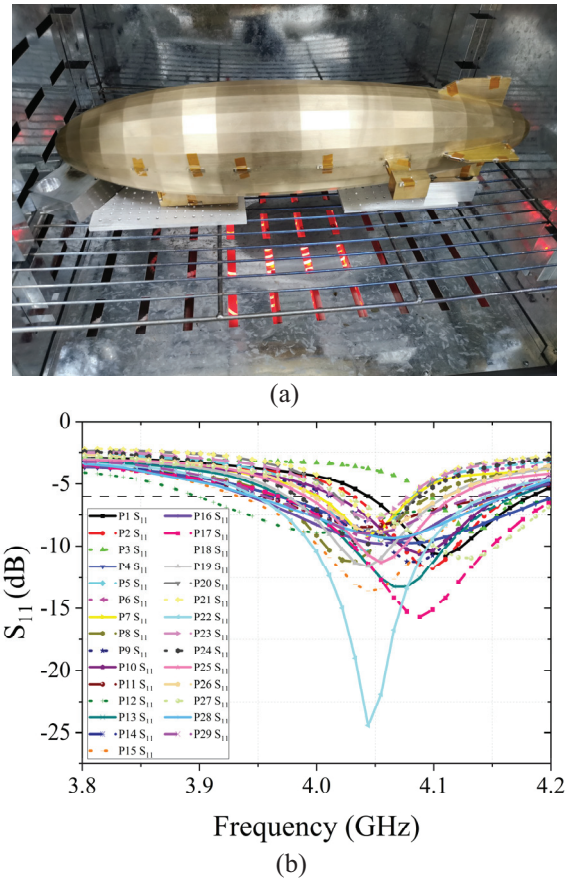

Fig. 9. (a) Prototype of the fabricated antenna array. (b) Measured reflection coefficient.

A lumped capacitor of C = 0.6 pF is added to the structure for impedance matching, with a dielectric plate of $\varepsilon_r = 2.2$. Figure 5 depicts the reflection coefficient and radiation pattern of the coupled line CE, with a maximum realized gain of 4.2 dBi. The distributed inductance, created by deforming part of the half-ring radiator into an interdigital coupling line, has a tuning effect on the CE. Additionally, the coupled line CE includes two deformation structures that simultaneously stimulate the CM of the platform, thereby enhancing the bandwidth to a certain extent.

Compared with modal synthesis results in [19], where four dominant aircraft modes produced discrete $\pm 45^\circ$ scanning with -9 dB SLL, the present design utilizes 12 significant modes to realize continuous $\pm 60^\circ$ beam scanning and SLL below -13 dB. This indicates that the proposed CM-MOEA/D framework approaches the modal-limited directivity bound while balancing beamwidth and side.

In this paper, a scaled prototype was employed, the operating frequency was proportionally scaled, maintaining the same electrical size and equivalent number of effective CEs as in a full-scale airship. This approach, also adopted in [21], ensures electromagnetic equivalence while facilitating laboratory measurement. The proposed array is fully conformal with the airship body, where the CEs function as distributed excitation structures rather than protruding antennas, avoiding added aerodynamic and structural loads. For large apertures, modular subarray optimization can be applied within the same CM-MOEA/D framework, ensuring scalability and practical feasibility.

B. Distributed heterogeneous phased array design

The CEs (P18 to P29) are positioned as shown in Fig. 6. The beam scans in the negative Y-axis direction and transforms into symmetric excitation to obtain the scanning beam on the other side. Fine-tuning the CE size and patch capacitance is necessary to match the input port impedance.

This paper proposes a method to determine excitation amplitude and phase of CEs at different scan angles. It involves: (a) adjusting excitation amplitude based on current distribution; (b) conducting full-wave simulation on the airship platform; (c) using MOEA/D based on far-field information to solve for excitation amplitude and phase. The excitation power of CEs is discretized,

and the optimized excitation amplitudes for the radiation beams are shown in Fig. 7. Additionally, some CEs will have small amplitudes of excitation to optimize side lobe and cross-polarization level. The array S_{21} is depicted in Figs. 8 (a) and 8 (b), the radiation efficiency exceeds 80% at different scan angles near the working frequency, enhancing the platform's radiation efficiency and increasing the radiation aperture compared to traditional meter-wave antennas.

C. Antenna performance

The scale airship platform and CEs were fabricated. The length of the platform is 515 mm, and the material is brass for easy welding. As for the coupling line CE, it is difficult for the short-circuit column to weld and support the weight of the coaxial transmission line under the scaled size. The overall coupling line structure is not changed. A Taconic RF-35 dielectric plate with thickness 1.52 mm and $\varepsilon_r = 3.5$ is adopted. The short-circuit column is redesigned as a metallic via, allowing the entire bottom surface of the CE to be brought into contact with and mechanically fixed to the platform. In addition, since no lumped elements are employed, no extra matching network is required, thereby avoiding the associated tolerance and mismatch errors.

Figure 9 (a) displays the fabricated prototype of the distributed heterogeneous phased array system. Figure 9 (b) illustrates the measured reflection coefficient of the array. Despite machining errors in the platform and CEs, deviation in the fixed position of the CEs, and error amplification during scaling, the reflection coefficient experiences a certain degree of deterioration and frequency deviation. Nevertheless, with the exception of a few CEs, the reflection coefficient satisfies the requirement of being less than -6 dB near 4.06 GHz. As a result, the simulated and measured radiation patterns in the E-plane (XOY plane) at 4 GHz is shown in Fig. 10.

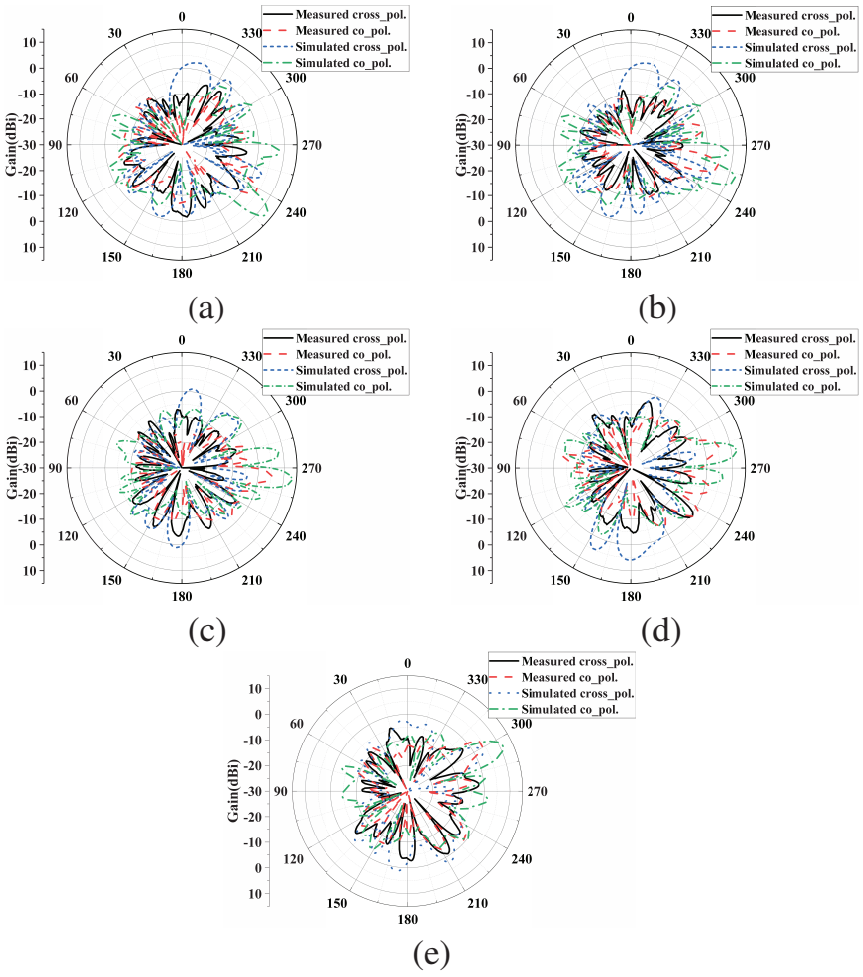

Fig. 10. Simulated and measured radiation patterns in the E-plane (XOY plane) at 4 GH. (a) Beam steered $[(\theta,\varphi) = (90^\circ, 330^\circ)]$, (b) beam steered $[(\theta,\varphi) = (90^\circ, 345^\circ)]$, (c) broadside $[(\theta,\varphi) = (90^\circ, 0^\circ)]$, (d) beam steered $[(\theta,\varphi) = (90^\circ, 15^\circ)]$, (e) beam steered $[(\theta,\varphi) = (90^\circ, 30^\circ)]$.

To facilitate easy coaxial line fixation and minimize radiation impact with small unit spacing, we adopted a thin coaxial line with an outer diameter of 0.9 mm, which results in relatively large insertion losses. Furthermore, the CEs' reflection coefficient displays varying degrees of frequency deviation, and installation position and platform structure errors lead to a decrease in measured gain. However, the beam direction at various scan angles correspond well with the simulation results and has low levels of cross-polarization and sidelobes.

The airship-based conformal array is designed with system-level integration in mind. The low-profile structure conforms to the curved envelope, effectively minimizing aerodynamic drag and payload protrusion. The number of active modes is determined using the modal significance threshold (MS ≥ 0.707), ensuring efficient excitation without unnecessary modal expansion. This constraint not only reduces structural and computational complexity but also maintains stable directivity and low sidelobe levels. Furthermore, the smooth surface integration helps reduce RCS and improve stealth compatibility for high-altitude platforms.

IV. CONCLUSION

This paper outlines a CM-based approach for designing a distributed heterogeneous conformal phased array system. It considers polarization characteristics and beam switchable ability for specific communication requirements. This guides the placement of the designed coupling line CEs. The system achieves a 60° beam scanning range on both sides of the airship platform, with a gain of over 10 dBi at different scan angles. A 1:40 scale model was fabricated and measured to validate the design method. This approach can be applied to the design of conformal phased array antennas on other platforms.

ACKNOWLEDGMENT

This work was supported in part by the Postdoctoral Innovative Talent Support Program (Boshi Plan) of China under Grant No. GZB20250133, National Natural Science Foundation of China (No. 62531021) and in part by the Open Fund of the State Key Laboratory of Millimeter Waves, Southeast University under Grant KN202502-01.

REFERENCES

[1] L. V. Berkner, "Naval airborne radar," *Proceedings of the IRE*, vol. 34, pp. 671–706, Sep. 1946.

[2] F. W. Cipola, "A 7.5-GHz microstrip phased array for aircraft-to-satellite communication," *IEEE Trans. Antennas Propag.*, vol. 29, no. 1, pp. 166–170, Jan. 1981.

[3] Z. Li, K. Wang, Y. Lv, S. Qian, X. Zhang, and X. Cui, "Wing conformal load-bearing endfire phased array antenna skin technology," *IEEE Trans. Antennas Propag.*, vol. 71, no. 3, pp. 2064–2069, Mar. 2023.

[4] J.-J. Peng, S.-W. Qu, M. Xia, and S. Yang, "Conformal phased array antenna for unmanned aerial vehicle with $\pm 70^{\circ}$ scanning range," *IEEE Trans. Antennas Propag.*, vol. 69, no. 8, pp. 4580–4587, Aug. 2021.

[5] W. F. Bahret, "The beginnings of stealth technology," *IEEE Transactions on Aerospace and Electronic Systems*, vol. 29, no. 4, pp. 1377–1385, Oct. 1993.

[6] V. Manohar, S. Bhardwaj, S. B. Venkatakrishnan, and J. L. Volakis, "VHF/UHF ultrawideband tightly coupled dipole array for CubeSats," *IEEE Open J. Antennas Propag.*, vol. 2, pp. 702–708, 2021.

[7] J. D. Hawkins, L. B. Lok, P. V. Brennan, and K. W. Nicholls, "HF wiremesh dipole antennas for broadband ice-penetrating radar," *IEEE Antennas Wireless Propag. Lett.*, vol. 19, no. 12, pp. 2172–2176, Dec. 2020.

[8] Y. Gao, D. Wu, and Q. Wu, "Analysis of conformal antenna arrays using cylindrical periodic Green's function and RWG basis function," *IEEE Trans. Antennas Propag.*, vol. 72, no. 2, pp. 1385–1396, Feb. 2024.

[9] Y. Chen and C. F. Wang, "HF band shipboard antenna design using characteristic modes," *IEEE Trans. Antennas Propag.*, vol. 63, no. 3, pp. 1004–1013, Mar. 2015.

[10] Y. Chen and C.-F. Wang, "Electrically small UAV antenna design using characteristic modes," *IEEE Trans. Antennas Propag.*, vol. 62, no. 2, pp. 535–545, Feb. 2014.

[11] C. Wang, Y. Chen, and S. Yang, "Application of characteristic mode theory in HF band aircraft-integrated multiantenna system designs," *IEEE Trans. Antennas Propag.*, vol. 67, no. 1, pp. 513–521, Jan. 2019.

[12] R. F. M. Delgado Castillo, R. Ma, and N. Behdad, "Platform-based, electrically-small HF antenna with switchable directional radiation patterns," *IEEE Trans. Antennas Propag.*, vol. 69, no. 8, pp. 4370–4379, Aug. 2021.

[13] K. Ren, M. Ranjbar Nikkhah, and N. Behdad, "Design of dual polarized platform-based HF antennas using the characteristic mode theory," *IEEE Trans. Antennas Propag.*, vol. 68, no. 7, pp. 5130–5141, Feb. 2020.

[14] R. Ma and N. Behdad, "Design of platform-based HF direction-finding antennas using the characteristic mode theory," *IEEE Trans. Antennas Propag.*, vol. 67, no. 3, pp. 1417–1427, Mar. 2019.

[15] C. Wang, Y. Chen, G. Liu, and S. Yang, "Aircraft-integrated VHF band antenna array designs using

characteristic modes," *IEEE Trans. Antennas Propag.*, vol. 68, no. 11, pp. 7358–7369, Nov. 2020.

[16] G. Angiulli, G. Amendola, and G. Di Massa, "Application of characteristic modes to the analysis of scattering from microstrip antennas," *Journal of Electromagnetic Waves and Applications*, vol. 14, no. 8, pp. 1063–1081, 2000.

[17] R. J. Garbacz and R. H. Turpin, "A generalized expansion for radiated and scattered fields," *IEEE Trans. Antennas Propag.*, vol. 19, no. 3, pp. 348–358, May 1971.

[18] R. Harrington and J. Mautz, "Theory of characteristic modes for conducting bodies," *IEEE Trans. Antennas Propag.*, vol. 19, no. 5, pp. 622–628, Sep. 1971.

[19] C. Wang, Y. Chen, G. Liu, and S. Yang, "Aircraft-integrated VHF band antenna array designs using characteristic modes," *IEEE Trans. Antennas Propag.*, vol. 68, no. 11, pp. 7358–7369, Nov. 2020.

[20] C. Wang, Y. Chen, and S. Yang, "Bandwidth enhancement of a dual-polarized slot antenna using characteristic modes," *IEEE Antennas Wireless Propag. Lett.*, vol. 17, no. 6, pp. 988–992, June 2018.

[21] C. Wang, Y. Chen, and S. Yang, "Application of characteristic mode theory in HF band aircraft-integrated multiantenna system designs," *IEEE Trans. Antennas Propag.*, vol. 67, no. 1, pp. 513–521, Jan. 2019.

Yuhao Feng received the B.S. degree in information science and technology from the University of Arizona, Tucson, AZ, USA, in 2018, the M.S. degree in electronic engineering from the Colorado School of Mines, Golden, CO, in 2020, and the Ph.D. degree in electronic science and technology from the University of Electronic Science and Technology of China (UESTC), Chengdu, China, in 2024. His research interests include antennas, filters, and RF circuits.

Zijian Yang received the M.S. degree in electronic science and technology from the University of Electronic Science and Technology of China (UESTC), Chengdu, China, in 2022, and is currently an RF antenna engineer with Shenzhen.

A Multi-GPU Accelerated DGTD Method for Solving Electrically Large-Scale Problems

Ziang Shen[1] and Lei Zhao[2]

[1]College of Electronic and Information Engineering
Nanjing University of Aeronautics and Astronautics, Nanjing 211106, China
shenziang@nuaa.edu.cn

[2]School of Information and Control Engineering
China University of Mining and Technology, Xuzhou 221116, China
leizhao@cumt.edu.cn

Abstract – In this paper, we proposed a multiple graphics processing units (GPU) platform accelerated discontinuous Galerkin time-domain (DGTD) method for solving electrically large-scale problems. Rather than simply porting the code to a GPU, we proposed a cache optimization strategy tailored to the GPU architecture. Furthermore, by grouping and reordering the elements and employing asynchronous techniques, we achieve a linear speedup ratio when scaling across multiple GPUs. The numerical examples not only validate accuracy of the proposed method, but also demonstrate excellent performance, achieving up to 40 times speedup even compared to parallelism CPU implementations.

Index Terms – Discontinuous Galerkin time-domain (DGTD) method, multiple graphics processing units (multi-GPU).

I. INTRODUCTION

Electrically large-scale problems have always been a challenge in computational electromagnetics (CEM). Their considerable computational complexity demands a combination of high-performance hardware and efficient algorithms. Among various electromagnetic numerical methods, the discontinuous Galerkin time-domain (DGTD) method [1–4] has attracted growing attention from researchers. As an efficient algorithm, DGTD offers greater flexibility than traditional approaches when dealing with complex problems, as it supports non-conformal, unstructured, and mixed-type meshes while maintaining reliable accuracy [5–7]. The numerical flux introduced by the finite-volume time-domain (FVTD) method [8] allows the boundaries between adjacent elements to be non-conformal. Moreover, models can be decomposed into several subdomains with different time iteration step increments [9, 10], facilitating the solution of multiscale problems. DGTD also exhibits strong potential for parallel computing [11–13]. During the time iteration process, computations within each element are entirely independent, making DGTD highly suitable for high-performance computing (HPC).

However, traditional CPU-based parallelization is still unable to handle such large computational loads. Consequently, GPU-based acceleration has attracted significant attention in DGTD research. In [14], DGTD was deployed on the GPU, achieving approximately 50 times speedup over serial computation. The authors of [15] implemented a hybrid MPI/GPU DGTD algorithm with local time stepping (LTS). In [16], the GPU-accelerated DGTD method was used to solve the scattering problem of electrically large targets. In [17], GPU-DGTD is used to solve hybrid meshes. The authors of [18] implemented GPU acceleration of a low-storage Runge-Kutta (LSRK) time iteration method. The authors of [19] used GPU-accelerated DGTD to simulate EM systems with field-circuit interactions. A common limitation in the above studies is that they do not fully leverage systems equipped with two or more GPU, and the use of multiple GPUs has been widely applied in other numerical methods. The authors of [20] assembled the finite-element method (FEM) matrices on both single GPU and multiple GPUs. The authors of [21, 22] discuss strategies for load balancing and for reducing cross-GPU communication. The authors of [23] solved FEM using a distributed message passing interface (MPI) approach. Unlike these algorithms, the DGTD has lower memory requirements when solving electrically large-scale problems, but its challenge lies in the massive amount of computation. Therefore, using multiple clusters actually increases unnecessary communication overhead. DGTD is better suited to a shared-memory programming model, using OpenMP to control multiple GPU devices, and also offers the practical advantage of minimal intrusion into the existing codebase. For example, a multi-GPU leap-frog scheme was proposed in [24].

Submitted On: September 03, 2025
Accepted On: November 13, 2025

https://doi.org/10.13052/2025.ACES.J.401103

This paper proposes a multi-GPU DGTD method. Combined with an asynchronous multi-GPU strategy to hide data transmission time and cache optimization strategy to minimize data access latency, our method delivers superior performance, enabling the solution of electrically large-scale problems that are intractable with traditional CPU-based approaches due to excessive computational demands.

II. FORMULATIONS AND GPU ACCELERATED IMPLEMENTATION

A. DGTD method

In the source-free region Ω, consider Maxwell's equations in the time domain:

$$\mu\frac{\partial \mathbf{H}}{\partial t} = -\nabla\times\mathbf{E}, \tag{1}$$

$$\varepsilon\frac{\partial \mathbf{E}}{\partial t} = \nabla\times\mathbf{H} - \sigma\mathbf{E}, \tag{2}$$

where ε is the permittivity, μ is the permeability, σ is the conductivity, $\mathbf{E}$ is the electric field intensity, and $\mathbf{H}$ is the magnetic field intensity. To solve equations (1) and (2), the computational domain Ω is divided into K non-overlapping tetrahedral elements as $\Omega \approx \bigcup_{k=1}^{K}\Omega_k$.

Here we express (1) and (2) as the conservation formulation [25]:

$$\mathbf{Q}\partial_t\mathbf{q} + \nabla\cdot\mathbf{F} = 0, \tag{3}$$

in which

$$\nabla\cdot\mathbf{F} = \partial_x\begin{bmatrix}\mathbf{e}_x\times\mathbf{E}\\ -\mathbf{e}_x\times\mathbf{H}\end{bmatrix} + \partial_y\begin{bmatrix}\mathbf{e}_y\times\mathbf{E}\\ -\mathbf{e}_y\times\mathbf{H}\end{bmatrix} + \partial_z\begin{bmatrix}\mathbf{e}_z\times\mathbf{E}\\ -\mathbf{e}_z\times\mathbf{H}\end{bmatrix}, \tag{4}$$

$$\mathbf{Q} = \begin{bmatrix}\mu & 0\\ 0 & \varepsilon\end{bmatrix}, \tag{5}$$

$$\mathbf{q} = \begin{bmatrix}\mathbf{H}\\ \mathbf{E}\end{bmatrix}, \tag{6}$$

where $\mathbf{e}_x$, $\mathbf{e}_y$, and $\mathbf{e}_z$ are the unitary vectors along the axis in the cartesian coordinate system.

In each tetrahedral element Ω_k, we assume that the approximation solution of (3) is $\tilde{\mathbf{q}}^k(\mathbf{r},t)$ and can be expressed as:

$$\tilde{\mathbf{q}}^k(\mathbf{r},t) = \sum_{i=1}^{N_p} q(\mathbf{r}_i,t)l_i(\mathbf{r}), \tag{7}$$

where $l_i(\mathbf{r})$ is the Lagrange polynomial basis function, N_p is the number of degrees of freedoms (DOFs) and its relationship with the number of Lagrange order n is:

$$N_p = \frac{(n+1)(n+2)(n+3)}{6}. \tag{8}$$

Since $\tilde{\mathbf{q}}^k(\mathbf{r},t)$ and $\mathbf{q}^k(\mathbf{r},t)$ are not identical, we use Galerkin's method to force the projection between the test function and residual to be zero. We have the semi-discrete system of Maxwell's equations:

$$\varepsilon\mathbf{M}^k\frac{\partial \mathbf{E}}{\partial t} = \mathbf{S}^k\times\mathbf{H} + \oint_{\partial\Omega_k}\mathbf{n}\times(\mathbf{F}_E^k - \mathbf{F}_E^*)l_i^k(\mathbf{r})d\mathbf{r}, \tag{9}$$

$$\mu\mathbf{M}^k\frac{\partial \mathbf{H}}{\partial t} = -\mathbf{S}^k\times\mathbf{E} + \oint_{\partial\Omega_k}\mathbf{n}\times(\mathbf{F}_H^k - \mathbf{F}_H^*)l_i^k(\mathbf{r})d\mathbf{r}, \tag{10}$$

where $\mathbf{M}^k$ and $\mathbf{S}^k$ are the local mass matrix and stiffness matrix, respectively, and n denotes the unit normal vector points from the element Ω_k to the neighbor element.

In the DGTD method, the fields inside each element must remain continuous, while discontinuous are allowed across the boundaries of adjacent elements. These adjacent elements are connected through the numerical fluxes, so the solving process inside each element is independent and parallelizable. There are a variety of types of numerical fluxes to choose from, and here we list only the formulation of the central numerical flux:

$$\mathbf{n}\times\mathbf{E}^* = \frac{1}{2}\mathbf{n}\times(\mathbf{E}^+ + \mathbf{E}^-), \tag{11}$$

$$\mathbf{n}\times\mathbf{H}^* = \frac{1}{2}\mathbf{n}\times(\mathbf{H}^+ + \mathbf{H}^-), \tag{12}$$

where $\mathbf{E}^-$ or $\mathbf{H}^-$ denote the field inside the element Ω_k on the boundary, and $\mathbf{E}^+$ or $\mathbf{H}^+$ denotes the field in the neighbor element on the boundary.

The equations above can be solved by various methods. Considering that the memory resources of the GPU are limited, we employ the LSRK [18] method to solve the DGTD equations:

$$\begin{aligned}&\mathbf{P}_0 = \mathbf{q}_n(t)\\ &\begin{cases}\mathbf{K}_i = a_i\mathbf{K}_{i-1} + \Delta t f(\mathbf{P}_{i-1}, t + c_i\Delta t)\\ \mathbf{P}_i = \mathbf{P}_{i-1} + b_i\mathbf{K}_i\end{cases},\\ &\mathbf{q}_n(t+\Delta t) = \mathbf{P}_5\end{aligned} \tag{13}$$

where subscript i is taken to be 1, 2, 3, 4, and 5, which means the number of stages, coefficients a_i, b_i, and c_i define the properties of the LSRK, and Δt is the time step of DGTD.

B. Multi-GPU accelerated DGTD implementation

Among the various GPU programming frameworks, compute unified device architecture (CUDA) was selected as the primary platform for our multi-GPU DGTD implementation, owing to its mature architecture, comprehensive toolchain, and widespread community

support. To fully leverage the floating-point computing power brought by GPUs, DGTD must be parallelized as fine-grained as possible. According to the previous section, during each iterative step, the electric and magnetic field at each Lagrange-Gauss-Lobatto (LGL) point can be computed independently. These field components, such as $\mathbf{E}_x$ and $\mathbf{E}_y$, are defined as the smallest parallel tasks, as shown in Fig. 1.

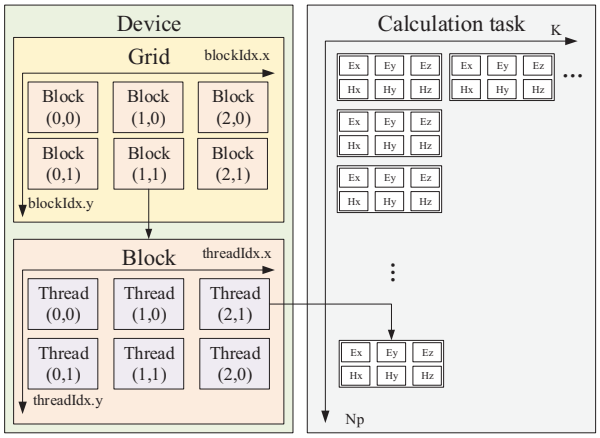

Fig. 1. Computing tasks of six scalar fields on one LGL point are packed as the minimum parallel unit and distributed to a Thread of a CUDA kernel function.

When using multiple GPU devices, it is better to use GPUs with the same specifications to ensure balanced computational load distribution. Maintaining a balanced load across devices is important to avoid a situation where one device is working while others are idle. Especially when the complex problems require a large number of iterations, the efficiency loss cannot be ignored. Assume that the computing platform has N_{device} CUDA devices. During the iterative process, the host will launch N_{device} CPU Threads, and each GPU is assigned to its corresponding CPU Thread. Each GPU is assigned an equal share of the total tasks, which is $(K \times N_p)/N_{device}$.

The key distinction between multi-GPU and single-GPU execution lies in the data dependency for numerical flux calculations. Each element requires field data from its neighbors to compute the numerical flux. When using a single GPU to execute time step iterations, the data can be stored in the device memory, and there is no need to exchange data with the host memory during the iteration. However, when using multiple GPUs for iterations, if the neighboring elements are in the same device, they can be directly obtained, but if they are in different devices, they need to be obtained from the storage of other devices. Consequently, in each time step of iteration, although the calculation time of multi-GPU is reduced, the additional data exchanges will cause performance loss.

C. Rearrange elements and asynchronous iteration

Load distribution does not simply divide the mesh elements into several equal parts and assign them to different devices. Because the mesh generated by the pre-processing software is not always ordered, direct distribution will cause a large amount of information to be exchanged between devices. Therefore, we need to reduce the number of exchanged elements as much as possible when grouping mesh elements. In this paper, the mesh is partitioned into several equal sections along its longest axis, as shown in Fig. 2.

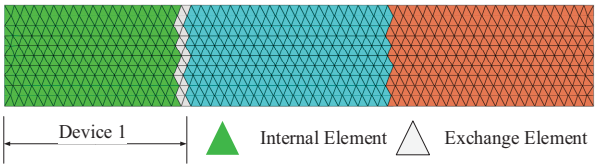

Fig. 2. Schematic diagram of the elements grouping of the target. Elements that are not connected to other groups are called internal elements, otherwise they are called exchange elements. Elements in the same group will be assigned to the same CUDA device.

During each iteration, the data of the exchange elements in each group needs to be transferred to other devices. While grouping only reduces the number of these elements, the storage order of exchange and internal elements becomes interleaved. Since data transfer between GPU and host is most efficient when performed as a single contiguous Block, we rearrange the element order within each group. In this paper, all data of exchange elements within a group are placed at the head of the array, as shown in Fig. 3.

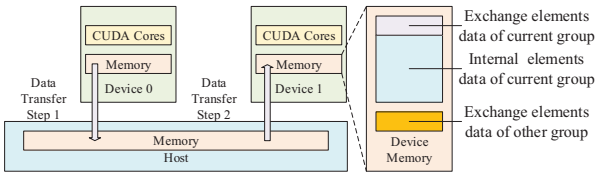

Fig. 3. Schematic diagram of data transfer during time step iterations.

Since the data transfer is significantly slower than computation, reducing only the amount of exchanged data does not yield satisfactory acceleration. However, the asynchronous characteristics of CUDA provide a solution by allowing the GPU to overlap computation with data transmission. To leverage this, we propose an asynchronous iteration strategy. In each time step, the

exchange elements are computed first, and then different CUDA streams are used to simultaneously execute two tasks: transferring the exchange elements data and computing the internal elements. Because the number of internal elements is much larger than the exchange elements, the time of data exchange can be covered by the calculation time, thereby masking the latency of data exchange.

D. Cache optimization strategy

The low memory consumption of DGTD mitigates the constraints of limited GPU memory capacity, thereby leveraging its advantages in speed and bandwidth. Furthermore, this section introduces an on-chip caching strategy designed to further accelerate data access.

As shown in Fig. 1, when a CUDA kernel function is launched, the kernel initializes a Grid containing multiple Blocks. These Blocks are distributed to streaming multiprocessors (SMs) for execution. Within each Block, Threads can transmit data through on-chip Shared Memory, which offers lower latency than global memory. In our implementation, all tasks on one element are packed as a Block, which means they can share the same set of geometric and material data, and only need to access the global memory once. In addition, we utilize texture memory to accelerate data retrieval from global memory. By binding the texture references to the corresponding global memory regions, CUDA cores can access the required data in fewer clock cycles. Additionally, the data that has been accessed will be stored in the on-chip cache, avoiding accessing the global memory again, which further optimizes memory performance.

III. NUMERICAL RESULTS

In this section, we will use several numerical examples to demonstrate the accuracy and efficiency of the multi-GPU DGTD method proposed in this paper.

A. Cache optimization and asynchronous data exchange strategy

The first example will be used to verify the accuracy and efficiency of the multi-GPU DGTD in solving radiation problems. As shown in the Fig. 4, we built a 50*60 mm patch antenna model and divided into 24080 tetrahedron elements. The substrate material has $\varepsilon = 4.4$ and $\mu = 1$. We solved the S11 parameters from 1 GHz to 10 GHz. As can be seen from the Fig. 4, the proposed method also has reliable accuracy compared with software HFSS [26] in solving radiation problems.

In this example, the performance of our strategy was evaluated on a Dell workstation equipped with three Nvidia Quadro K6000 GPUs. We first use one GPU to test our cache optimization strategy, and the computation times are shown in Table 1. In the baseline code without cache optimization, CUDA cores directly read and write to the device memory. In the cache-optimized version, the CUDA core will read data through the texture memory, and the data during the calculation process is temporarily stored in registers and Shared Memory and are written to the device memory after the calculation is completed, which minimizes interaction with the device memory. It can be seen from Table 1 that using cache instead of device memory as much as possible can effectively improve computing efficiency.

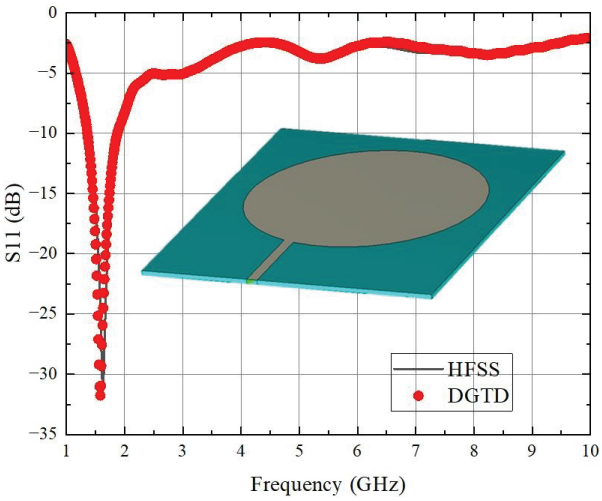

Fig. 4. Patch antenna model and comparison of numerical results of Multi-GPU DGTD and HFSS.

Table 1: Time comparison of antenna model with and without cache optimization

Method	Number of GPUs	Calc. Time (s)
no cache opt.	1	4370.1
cache opt.	1	1869.1

Table 2: Time comparison between synchronous and asynchronous data exchange

Method	Number of GPUs	Calc. Time (s)	Acc. Ratio
Synchronous	3	715.06	2.61
Asynchronous	3	687.73	2.72

Next, we validated the multi-GPU implementation based on the asynchronous data exchange strategy. The cache-optimized single-GPU program from the previous test will be used as the baseline because it does not require data exchange. The computation times of synchronous and asynchronous strategy program are

compared in Table 2. Acc. Ratio in Table 2 denotes the acceleration ratio and represents the ratio of the solving speed of different methods to the baseline, calculated as the execution time of the baseline divided by our proposed approach. From the time comparison, it can be seen that multi-GPU implementation has a significant acceleration compared to single GPU. Furthermore, the efficiency improvement brought by the asynchronous strategy makes the speedup of multi-GPU implementation setups closer to linear.

B. Efficiency Comparison Between GPU and CPU

In this example, we expand the problem size to demonstrate the advantages of the multi-GPU strategy over traditional CPUs. We designed a perfect electric conductor (PEC) ship model as shown in Fig. 5. The ship model has a length of 50 m and 125477 tetrahedron elements. The bistatic radar cross-section (RCS) of the ship at 100 MHz frequency is solved and compared with the results of Feko [27] and CST [28] in Fig. 5. It can be seen that our method has reliable accuracy in calculating complex electrically large-scale targets.

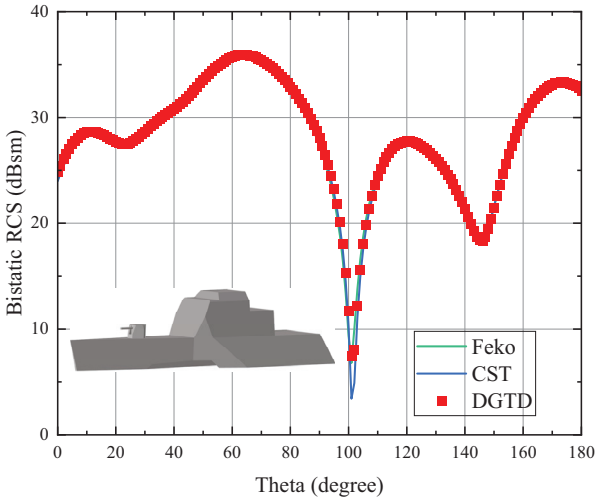

Fig. 5. Ship model and comparison of numerical results of Multi-GPU DGTD, Feko, and CST.

Table 3: Comparison of calculation time of ship model between CPU and GPU

Hardware	Calc. Time
CPU	18 h
GPU	1649.7 s

We believe that it is unfair to use products with different positioning or release times when comparing the efficiency between CPU and GPU. Therefore, in this example, the GPU program was executed by two Nvidia RTX 2080Ti, the CPU program was parallel executed by Intel i9-9900k with all eight physical cores. Hardware used in this example are flagship products of the same period. Furthermore, the GPU program is compiled by nvcc, and CPU program is compiled by icpx, which can provide more aggressive optimizations for Intel CPU to maximize performance, making them several times faster than CPU programs compiled by nvcc. From the time comparison in Table 3, we can see that the efficiency improvement of our multi-GPU DGTD is very impressive.

IV. CONCLUSION

In this paper, we proposed a multi-GPU accelerated DGTD method for solving electrically large-scale problems. Through cache optimization strategy and asynchronous data exchange strategy, we improved the efficiency of GPU programs and achieved linear speedup when using multiple devices. The several numerical examples not only prove that the proposed method is effective and accurate but also show that, when encountering complex electric large-scale problems that the CPU program cannot solve in a limited time, using GPU is the only option.

REFERENCES

[1] J. S. Hesthaven and T. Warburton, *Nodal Discontinuous Galerkin Methods, Algorithms, Analysis, and Applications*. New York: Springer, 2008.

[2] L. E. Tobón, Q. Ren, and Q. H. Liu, "A new efficient 3D discontinuous Galerkin time-domain (DGTD) method for large and multiscale electromagnetic simulations," *Journal of Computational Physics*, vol. 283, pp. 374–387, 2015.

[3] J. Chen and Q. H. Liu, "Discontinuous Galerkin time-domain methods for multiscale electromagnetic simulations: A review," *Proceedings of the IEEE*, vol. 101, pp. 242–254, 2013.

[4] J. J. Jin, "From FETD to DGTD for computational electromagnetics," *ACES Tutorial*, Williamsburg, VA, Mar. 2015.

[5] R. Sevilla, O. Hassan, and K. Morgan, "The use of hybrid meshes to improve the efficiency of a discontinuous Galerkin method for the solution of Maxwell's equations," *Computers & Structures*, vol. 137, pp. 2–13, 2014.

[6] S. Yan, C. P. Lin, R. R. Arslanbekov, V. I. Kolobov, and J.-M. Jin, "A discontinuous Galerkin time-domain method with dynamically adaptive cartesian mesh for computational electromagnetics," *IEEE Transactions on Antennas and Propagation*, vol. 65, pp. 3122–3133, 2017.

[7] I. Hussain, H. Li, and Q. Cao, "Multiscale structure simulation using adaptive mesh in DGTD method," *IEEE Journal on Multiscale and Multiphysics*

Computational Techniques, vol. 2, pp. 115–123, 2017.

[8] P. Bonnet, X. Ferrières, F. Issac, F. Paladian, J. Grando, J. Alliot, and J. Fontaine, "Numerical modeling of scattering problems using a time domain finite volume method," *Journal of Electromagnetic Waves and Applications*, vol. 11, pp. 1165–1189, 1997.

[9] J. Diaz and M. J. Grote, "Energy conserving explicit local time stepping for second-order wave equations," *SIAM Journal on Scientific Computing*, vol. 31, pp. 1985–2014, 2009.

[10] A. Taube, M. Dumbser, C. D. Munz, and R. Schneider, "A high-order discontinuous Galerkin method with time-accurate local time stepping for the Maxwell equations," *International Journal of Numerical Modelling: Electronic Networks, Devices and Fields*, vol. 22, pp. 77–103, 2009.

[11] L. Zhao, G. Chen, W. Yu, and J. M. Jin, "A fast waveguide port parameter extraction technique for the DGTD method," *IEEE Antennas and Wireless Propagation Letters*, vol. 16, pp. 2659–2662, 2017.

[12] G. Chen, L. Zhao, W. Yu, and J. M. Jin, "Discontinuous Galerkin time domain method for devices with lumped elements," in *International Applied Computational Electromagnetics Society* (*ACES*) *Symposium*, Suzhou, China, pp. 1–2, 2017.

[13] W. Yu, L. Zhao, and G. Chen, "A novel DGTD method and engineering applications," in *International Conference on Electromagnetics in Advanced Applications* (*ICEAA*), Cairns, QLD, Australia, pp. 324–327, 2016.

[14] A. Klöckner, T. Warburton, J. Bridge, and J. S. Hesthaven, "Nodal discontinuous Galerkin methods on graphics processors," *Journal of Computational Physics*, vol. 228, pp. 7863–7882, 2009.

[15] S. Dosopoulos, J. D. Gardiner, and J.-F. Lee, "An MPI/GPU parallelization of an interior penalty discontinuous Galerkin time domain method for Maxwell's equations," *Radio Science*, vol. 46, 2011.

[16] L. Zhao, G. Chen, and W. H. Yu, "GPU accelerated discontinuous Galerkin time domain algorithm for electromagnetic problems of electrically large objects," *Progress in Electromagnetics Research B*, vol. 67, pp. 137–151, 2016.

[17] J. Chan, Z. Wang, A. Modave, J. F. Remacle, and T. Warburton, "GPU-accelerated discontinuous Galerkin methods on hybrid meshes," *Journal of Computational Physics*, vol. 318, pp. 142–168, 2016.

[18] Z. Shen, Z. Li, J. Yu, C. Gu, X. Chen, and L. Zhao, "GPU accelerated DGTD method for analyzing electromagnetic scattering problems," in *International Applied Computational Electromagnetics Society Symposium* (*ACES-China*), Xuzhou, China, pp. 1–3, 2022.

[19] S. Wang, Q. Zhu, Y. Wu, R. Xu, and L. Zhao, "Accelerating DGTD-based field-circuit coupling simulations using CUDA," in *Cross Strait Radio Science and Wireless Technology Conference* (*CSRSWTC*), Macao, China, pp. 1–3, 2024.

[20] H. T. Meng, B. L. Nie, S. Wong, C. Macon, and J. M. Jin, "GPU accelerated finite-element computation for electromagnetic analysis," *IEEE Antennas and Propagation Magazine*, vol. 56, no. 2, pp. 39–62, Apr. 2014.

[21] C. Richter, S. Schöps, and M. Clemens, "Multi-GPU acceleration of algebraic multi-grid preconditioners for elliptic field problems," *IEEE Transactions on Magnetics*, vol. 51, no. 3, pp. 1–4, Mar. 2015.

[22] A. Dziekonski, P. Sypek, A. Lamecki, and M. Mrozowski, "Communication and load balancing optimization for finite element electromagnetic simulations using multi-GPU workstation," *IEEE Transactions on Microwave Theory and Techniques*, vol. 65, no. 8, pp. 2661–2671, Aug. 2017.

[23] D. Herrero-Pérez and H. Martínez-Barberá, "Multi-GPU acceleration for finite element analysis in structural mechanics," *Appl. Sci.*, vol. 15, no. 8, 2025.

[24] T. Cabel, J. Charles, and S. Lanteri. "Multi-GPU acceleration of a DGTD method for modeling human exposure to electromagnetic waves," *Hal Inria*, p. 27, 2011.

[25] B. Cockburn, S. Hou, and C.W. Shu, "The Runge–Kutta local projection discontinuous Galerkin finite element method for conservation laws. IV: The multidimensional case," *Mathematics of Computation*, vol. 54, pp. 545–581, 1990.

[26] Ansys-HFSS [Online]. Available: https://www.ansys.com/products/electronics/ansys-hfss.

[27] Altair-Feko [Online]. Available: https://www.altair.com/feko.

[28] CST-Studio-Suite [Online]. Available: https://www.3ds.com/products/simulia/cst-studio-suite.

Ziang Shen received his bachelor's degree in 2017 and his master's degree in 2020. He is presently pursuing a Ph.D. degree. His research focuses on high-performance computational electromagnetics, specifically frequency-domain, time-domain, and high-frequency asymptotic algorithms.

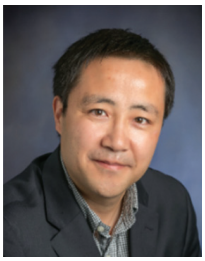

Lei Zhao is a professor at China University of Mining and Technology, ACES Fellow, IEEE senior member, member of the Antenna Branch of the Chinese Institute of Electronics, and chairman of IEEE AP-S Chapter Xuzhou. His main research directions are RF microwave devices, new electromagnetic materials, vortex wave communications, and computational electromagnetics.

Grey Wolf Optimization for Uplink Power Control in User-Centric Cell-Free Massive MIMO

Nguyen Van Cuong, Hoang Manh Kha, and Tong Van Luyen

School of Electrical and Electronic Engineering
Hanoi University of Industry, Hanoi, Vietnam
cuongnv@haui.edu.vn, khahoang@haui.edu.vn, luyentv@haui.edu.vn

Abstract – User-Centric Cell-Free Massive Multiple-Input Multiple-Output (UC-CFmMIMO) is a promising architecture for B5G networks, offering improved spectral efficiency (SE) and fairness by enabling joint transmission from distributed access points. However, uplink power control remains challenging due to inter-user interference and the decentralized network structure. This paper introduces a Grey Wolf Optimization (GWO)-based uplink power control scheme tailored for UC-CFmMIMO, targeting two practical objectives: maximizing sum SE and enhancing user fairness. Inspired by the hunting behavior of grey wolves, the proposed algorithm efficiently navigates the non-convex solution space without relying on convex assumptions. Numerical results demonstrate that the proposed scheme significantly improves fairness among users (e.g., achieving 3.39-bit/s/Hz at a cumulative distribution function (CDF) of 0.1) while maintaining high throughput performance (e.g., 118.99-bit/s/Hz at a CDF of 0.5). Moreover, the algorithm exhibits excellent scalability and computational efficiency, making it a practical and effective solution for large-scale B5G deployments.

Index Terms – Grey wolf optimization, max-min fairness, sum-rate maximization, uplink power control, user-centric cell-free massive MIMO.

I. INTRODUCTION

Next-generation wireless networks (B5G/6G) are envisioned to support massive connectivity, ultra-reliable low-latency communication, and pervasive intelligence across diverse industrial and urban scenarios [1–6]. User-Centric Cell-Free Massive Multiple-Input Multiple-Output (UC-CFmMIMO) represents a pivotal component in the architectural evolution toward B5G networks, where densely distributed access points (APs) collaboratively serve users without cell boundaries. This cell-free and user-centric paradigm enhances spectral efficiency (SE), fairness, and scalability, enabling seamless connectivity in ultra-dense and Industry 4.0/5.0 environments such as smart factories, autonomous systems, and intelligent logistics [5–9]. Through centralized coordination and flexible resource allocation, UC-CFmMIMO supports the hierarchical and distributed computing architecture fundamental to B5G network design.

Power control remains a key enabler for UC-CFmMIMO performance optimization by mitigating inter-user interference and regulating transmission power efficiency [5]. Conventional convex-based optimization methods, including geometric programming and bisection search [7–10], provide analytical tractability but exhibit limitations in large-scale non-convex settings due to their high computational complexity and reliance on convexity assumptions [11–14]. The fixed-point algorithm (FPA), while effective for convex formulations, encounters convergence degradation under user-centric interference coupling and dynamic channel conditions [5]. These pitfalls restrict adaptability to rapidly varying topologies and heterogeneous quality of service requirements in dense B5G deployments.

Recent research has explored advanced computational intelligence to overcome these challenges. In particular, Grey Wolf Optimization (GWO) has gained attention as a population-based metaheuristic that efficiently explores non-convex search spaces and mitigates premature convergence [15–17]. Beyond classical optimization, machine learning and intelligent control have emerged as complementary approaches for adaptive communication and control systems. For instance, machine learning-enabled channel estimation (CE) frameworks, such as distributed compressed sensing-based MIMO-filter bank multicarrier estimation for Industrial Internet of Things (IIoT) [18], low-complexity sparse CE for industrial big data [19], and sparse Bayesian learning-based CE for Filter bank multicarrier with offset quadrature amplitude modulation IIoT networks [20], demonstrate the capability of learning-assisted models to address sparsity, interference, and channel uncertainty. Likewise, intelligent control models, including fuzzy-tuned brain emotional

Submitted On: March 30, 2025
Accepted On: October 25, 2025

https://doi.org/10.13052/2025.ACES.J.401104

learning-based intelligent controller for satellite attitude regulation [21] and linear matrix inequalities-based stabilization of input derivative positive systems [22], illustrate the adaptability of learning-driven optimization and control paradigms across dynamic environments.

Motivated by these developments, this study proposes a GWO-based centralized uplink power control framework for UC-CFmMIMO networks, aligned with the B5G vision of sustainable, intelligent, and energy-efficient connectivity. Two distinct optimization formulations are considered: a fairness-oriented design maximizing the minimum SE among users and a throughput-oriented design maximizing the aggregate SE. The GWO algorithm is adapted to efficiently solve each non-convex problem without convex approximation, enabling scalable operation under dense user and AP deployments. Simulation results demonstrate that the proposed GWO-based schemes achieve superior trade-offs in fairness, throughput, and computational efficiency compared with conventional FPA, full power control (FPC), and bat algorithm (BA) benchmarks.

The main contributions of this paper are summarized as follows:

- We formulate two uplink power control problems in UC-CFmMIMO networks, one designed to enhance user fairness and the other to maximize system throughput.
- We adapt and integrate the GWO algorithm into the UC-CFmMIMO uplink power control framework, marking its first application in this context to effectively solve the formulated non-convex problems.
- We provide extensive simulation-based comparisons with conventional schemes (FPA, FPC) and BA to evaluate the performance of each proposed formulation in terms of SE, fairness, computational complexity, and scalability.

The remainder of this paper is structured as follows. Section II presents the system model. Section III formulates the optimization problem. Section IV details the proposed GWO-based solution. Section V provides numerical results validating the effectiveness of our approach. Section VI concludes the study and discusses its implications for sustainable wireless networks.

II. SYSTEM MODEL

We consider a UC-CFmMIMO network consisting of K single-antenna user equipment (UE) and L APs, each having N antennas as indicated in Fig. 1. The wireless channel is assumed to follow the block-fading model, where the channel remains constant over a coherence block and changes independently between blocks. A coherence block is a time-frequency block whose time duration equals the coherence time and whose bandwidth equals the coherence bandwidth. Hence, the channel between each AP-UE pair is constant and frequency-flat within a coherence block and can therefore be represented by a single channel realization.

In the considered time-division duplex protocol, each coherence block consists of τ_c transmission symbols, which are divided into three parts: τ_p symbols for uplink pilots, τ_u symbols for uplink data, and τ_d symbols for downlink data, satisfying $\tau_c = \tau_p + \tau_u + \tau_d$. The uplink pilots are transmitted prior to downlink data so that channel estimates can be obtained and used for precoding.

The channel between the lth AP and the kth UE in an arbitrary coherence block is denoted by $\mathbf{h}_{kl} \in \mathbb{C}^N$, modeled as a correlated Rayleigh fading distribution $\mathbf{h}_{kl} \sim \mathcal{N}_{\mathbb{C}}(\mathbf{0}_N, \mathbf{R}_{kl})$. Here $\mathcal{N}_{\mathbb{C}}(\mathbf{0}_N, \mathbf{R}_{kl})$ denotes a circularly symmetric complex Gaussian distribution with zero mean vector and covariance matrix $\mathbf{R}_{kl} \in \mathbb{C}^{N\times N}$. The vector $\mathbf{0}_N$ represents an $N \times 1$ all-zero vector. $\mathbf{R}_{kl} \in \mathbb{C}^{N\times N}$ is the spatial correlation matrix between the lth AP and the kth UE. The Gaussian distribution is utilized to represent the effects of small-scale fading, while the positive semidefinite correlation matrix $\mathbf{R}_{kl}$ characterizes large-scale fading, which encompasses factors such as geometric path loss, shadowing, antenna gains, and spatial channel correlation [3–5].

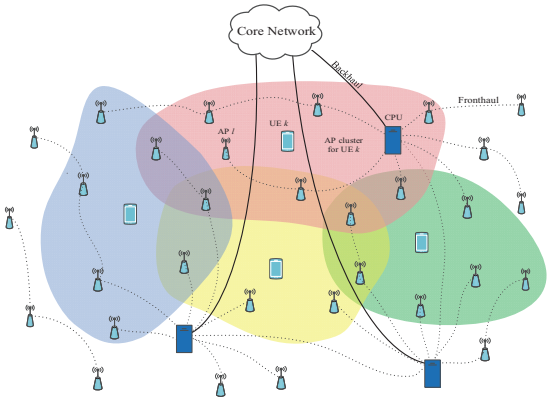

Fig. 1. UC-CFmMIMO network with L access points jointly serving K user equipment.

The uplink transmission powers can be represented as a vector $\mathbf{p} = [p_1, \ldots, p_K]^{\mathrm{T}}$, influencing all UEs. The uplink SE of the kth UE is determined by its effective signal-to-interference-plus-noise ratio (SINR), which depends on $\mathbf{p}$. Specifically, the numerator of the SINR is influenced by the transmission power p_k of the desired signal, while the interference term in the denominator is affected by all power components in $\mathbf{p}$. The effective SINR for the $k$thUE, applicable to centralized uplink operations, can be expressed in a

generalized form as [5]:

$$\mathrm{SINR}_k(\mathbf{p}) = \frac{b_k p_k}{\mathbf{c}_k^T \mathbf{p} + \sigma_k^2}, \tag{1}$$

where b_k represents the average effective channel gain of the desired signal for the kth UE, $\mathbf{c}_k = [\mathbf{c}_{k1}, \ldots, \mathbf{c}_{kK}]^{\mathrm{T}} \in \mathbb{R}^K_{\geq 0}$ contains the average interference coefficients, and σ_k^2 denotes the effective noise variance. These parameters are given by

$$b_k = |\mathbb{E}\{\mathbf{v}_k^{\mathrm{H}} \mathbf{D}_k \mathbf{h}_k\}|^2 \quad \forall k, \tag{2}$$

$$c_{kk} = \mathbb{E}\{|\mathbf{v}_k^{\mathrm{H}} \mathbf{D}_k \mathbf{h}_k|^2\} - b_k \quad \forall k, \tag{3}$$

$$c_{ki} = \mathbb{E}\{|\mathbf{v}_k^{\mathrm{H}} \mathbf{D}_k \mathbf{h}_i|^2\} - b_k \quad \forall k, \forall i \neq k, \tag{4}$$

$$\sigma_k^2 = \sigma^2 \mathbb{E}\{\|\mathbf{D}_k \mathbf{v}_k\|^2\}, \tag{5}$$

where $\mathbb{E}\{\cdot\}$ denotes the statistical expectation operator. The combining vector $\mathbf{v}_k$ denotes the centralized receive filter used at the CPU to extract the data of the kth UE from the aggregated uplink signal. In a centralized architecture the CPU collects (or has access to) the received signal components from all the L APs and applies a single global linear combiner $\mathbf{v}_k \in \mathbb{C}^{LN}$ to the stacked receive vector. Concretely, $\mathbf{v}_k$ is formed by stacking the local combining vectors from each AP $\mathbf{v}_k = [\mathbf{v}_{k1}^{\mathrm{T}}, \ldots, \mathbf{v}_{kL}^{\mathrm{T}}]^{\mathrm{T}}$, where $\mathbf{v}_{kl} \in \mathbb{C}^N$ is the local combiner applied to the N-antenna signal at the lth AP. The combined scalar observation used to detect the kth UE is $\mathbf{v}_k^H \mathbf{y}$, where $\mathbf{y}$ is the full LN-dimensional received signal stacked across APs. $\mathbf{D}_k = \mathrm{diag}\{\mathbf{D}_{k1}, \ldots, \mathbf{D}_{kL}\}$ is a block-diagonal matrix. $\mathbf{h}_i : i = \{1, \ldots, K\}$ is the channel vectors from all K UEs. Therefore, the uplink SE of the kth UE depends on $\mathbf{p}$ and can be written as [5]:

$$\mathrm{SE}_k(\mathbf{p}) = \frac{\tau_u}{\tau_c} \log_2(1 + \mathrm{SINR}_k(\mathbf{p})). \tag{6}$$

Here τ_u and τ_c are the numbers of symbols for uplink data and the total symbols in a coherence block, respectively.

Equations (1)–(6) represent the standard centralized SE formulation for uplink UC-CFmMIMO, derived from the general SINR structure given in [5, Theorem 5.2]. This formulation enables a unified optimization of the transmission powers across all UEs.

III. PROBLEM FORMULATION

The uplink power control process involves determining the appropriate uplink power levels for UEs to maximize a specific utility function, typically related to SE. In this study, we address two key power control problems: max-min SE fairness and sum SE maximization, each defined by its corresponding objective function $\mathrm{F1}(\mathbf{p})$ and $\mathrm{F2}(\mathbf{p})$, respectively.

Here, $\mathrm{F1}(\mathbf{p})$ represents the minimum SE among all users, aiming to enhance user fairness, while $\mathrm{F2}(\mathbf{p})$ denotes the aggregate SE of the system, focusing on maximizing total throughput. These functions are formulated as:

$$\mathrm{F1}(\mathbf{p}) = \min_{k \in \{1,\ldots,K\}} \mathrm{SE}_k(\mathbf{p}), \tag{7}$$

$$\mathrm{F2}(\mathbf{p}) = \sum_{k=1}^{K} \mathrm{SE}_k(\mathbf{p}). \tag{8}$$

Accordingly, the two optimization problems can be expressed as:

$$\textbf{(P1):} \max_{\mathbf{p}} \ \mathrm{F1}(\mathbf{p}) \quad \text{s.t.} \quad 0 < p_k \leq p_{\max}, \quad k = 1, \ldots, K. \tag{9}$$

$$\textbf{(P2):} \max_{\mathbf{p}} \ \mathrm{F2}(\mathbf{p}) \quad \text{s.t.} \quad 0 < p_k \leq p_{\max}, \quad k = 1, \ldots, K. \tag{10}$$

While max-min SE fairness prioritizes users with poor channel conditions, it may not fully exploit the potential for higher SE in large networks. In contrast, the sum SE maximization problem focuses on maximizing the total number of transmitted bits, regardless of their distribution among UEs. This approach is particularly suitable for scenarios where each UE interferes only with a small subset of neighboring users.

These two optimization problems highlight different objectives: max-min SE fairness ensures equitable resource allocation, whereas sum SE maximization prioritizes overall throughput. In the following section, we develop a GWO-based approach to efficiently solve both formulations.

IV. PROPOSED APPROACH

We propose an uplink power control scheme using the GWO to address optimization challenges in UC-CFmMIMO systems. GWO efficiently explores high-dimensional solution spaces, overcoming the limitations of conventional methods by avoiding local optima and ensuring robust performance in complex wireless environments [23–25].

A. Fitness function formulation

Our approach addresses two distinct objectives: max-min fairness and sum SE maximization. To this end, we design separate fitness functions that directly represent each goal under system constraints, enabling the GWO algorithm to efficiently search for optimal power control solutions.

For the identified problems (**P1**) and (**P2**) defined in section III, each defined as a single-objective

optimization, we construct two corresponding fitness functions, F1($\mathbf{p}$) and F2($\mathbf{p}$), to guide the GWO algorithm toward fairness and throughput optimization, respectively.

The constraints define the allowable power control range for each user, ensuring compliance with system limitations. We set the feasible search space within $[0, p_{\max}]$, where $p_{\max}$ represents the maximum transmission power. This ensures that all solutions generated by GWO satisfy power constraints while optimizing performance.

These formulations allow the algorithm to target distinct power control objectives in UC-CFmMIMO systems. This separation of objectives highlights the flexibility of the GWO framework in addressing diverse optimization goals under a unified metaheuristic paradigm.

B. Proposed algorithm

The GWO is a metaheuristic optimization technique inspired by the hierarchical leadership and cooperative hunting strategies of grey wolves. It categorizes wolves into four roles (alpha, beta, delta, omega), where the alpha leads the search process. The key strength of GWO lies in its ability to balance exploration and exploitation, efficiently navigating complex solution spaces while avoiding local optima [16].

Leveraging these properties, we develop a GWO-based algorithm to optimize uplink power control in UC-CFmMIMO systems. The detailed mathematical formulation of the proposed procedure is provided in Algorithm 1, which outlines the initialization, fitness evaluation, position update, boundary control, and termination criteria for achieving the optimal power allocation vector $\mathbf{p}* \leftarrow \mathbf{p}^{\alpha}$.

First, system-specific parameters such as the number of APs, UEs, antennas, and maximum transmission power are initialized, together with the GWO parameters including population size, search limits, and the fitness function. The initial power control vectors p_i are then randomly generated within the search domain to ensure solution diversity.

Each wolf's fitness is evaluated according to the optimization objective, and the top three wolves (alpha, beta, delta) are identified to guide the search. Subsequently, all wolves update their positions using adaptive coefficients that simulate encircling and attacking behaviors, balancing exploration and exploitation.

A random exploration factor is introduced to mitigate premature convergence. The iterations continue until a stopping condition is met, either the maximum iteration count or convergence in the fitness value. Finally, the best solution $p*$ is returned, representing the optimal power control vector that ensures an effective trade-off between efficiency and fairness in uplink power control.

Algorithm 1. Proposed GWO-based uplink power control algorithm.

Input: UC-CFmMIMO parameters; number of APs, number of UEs K, population size n_{pop}, maximum iterations n_{iter}, lower bound 0, upper bound $p_{\max}$, fitness function $\mathrm{F}(\mathbf{p}) \in \{\mathrm{F1}(\mathbf{p}), \mathrm{F2}(\mathbf{p})\}$
Output: Optimal transmission powers $\mathbf{p}^* \leftarrow \mathbf{p}^{\alpha}$
for $i \leftarrow 1$ **to** n_{pop} **do**
  if i = 1 then
    $\mathbf{p}_1 \leftarrow p_{\max}\mathbf{1}_{1\times K}$
  else
    $\mathbf{p}_i \leftarrow \mathscr{U}([0, p_{\max}]_{1\times K})$
  end
  Evaluate $\mathrm{F}(\mathbf{p}_i)$ and update $\mathbf{p}^{\alpha}, \mathbf{p}^{\beta}, \mathbf{p}^{\delta}$
end
$\mathbf{p}^* \leftarrow \mathbf{p}^a$
for $t \leftarrow 1$ **to** n_{itter} **do**
  $a \leftarrow 2 - 2t/n_{iner}$
  for $i \leftarrow 1$ **to** n_{pop} **do**
    $A^j \leftarrow \mathscr{U}([-a, a]_{1\times K}), j \in \{\alpha, \beta, \delta\}$
    $C^j \leftarrow 2\mathscr{U}([0, 1]_{1\times K}), j \in \{\alpha, \beta, \delta\}$
    $X^j \leftarrow \mathbf{p}^j - A^j \odot |C^j \odot \mathbf{p}^j - \mathbf{p}_j|, j \in \{\alpha, \beta, \delta\}$
    $\mathbf{p}_i \leftarrow (X^{\alpha} + X^{\beta} + X^{\delta})/3$
  if $\mathbf{p}_i > p_{\max}$ or $\mathbf{p}_i < 0$ then
    Project $\mathbf{p}_i$ back into $[0, p_{\max}]$
  end
  Evaluate $\mathrm{F}(\mathbf{p}_i)$ and update $\mathbf{p}^{\alpha}, \mathbf{p}^{\beta}, \mathbf{p}^{\delta}$
  end
end
return

V. NUMERICAL RESULTS

To evaluate the proposed GWO-based uplink power control scheme in UC-CFmMIMO scenarios, a network is deployed over a 1×1 km area with 100 randomly distributed APs and 20 UEs. Each AP is equipped with a single antenna, resulting in a total of 100 antennas across the network. Both AP and UE positions vary across 1000 independent network setups, each simulated over 50 channel realizations to ensure statistical robustness.

Communication occurs over a 20 MHz bandwidth, with a receiver noise power $\sigma^2 = -94$ dBm accounting for both thermal noise and a 7 dB receiver noise figure. UEs have a maximum uplink transmission power of $p_{\max} = 100$ mW, reflecting power constraints in practical deployments. The coherence block consists of samples aligned with a 2 ms coherence time and a 100 kHz coherence bandwidth, accommodating user mobility and outdoor propagation in sub-6 GHz bands. Large-scale fading follows the 3GPP Urban Microcell model, with

Rayleigh fading channels exhibiting spatial correlation based on a local scattering model.

For performance benchmarking, the proposed GWO-based schemes are compared with conventional methods, including FPA, FPC, and BA [26]. The BA approach follows the same centralized uplink operation and optimization objectives as the proposed formulations, ensuring consistent evaluation criteria across all algorithms.

For optimization, both GWO and BA operate with a population size of 300 and 50 iterations to ensure a fair comparison. The BA parameters are configured as loudness of 0.5 and pulse rate of 0.5. The GWO algorithm and its procedural steps are fully presented in section IV in algorithmic form to facilitate reproducibility.

The chosen population size and iteration count were determined based on the theoretical balance between exploration and exploitation in population-based metaheuristics. In GWO, a larger population enhances global exploration capability, reducing the risk of premature convergence, while an excessive number of iterations primarily improves local refinement at the cost of higher computational complexity. In this study, the selected configuration of 300 agents and 50 iterations achieves stable convergence behavior and consistent optimization performance, as evidenced in section V part A. The convergence profiles confirm that this setting allows GWO to reach near-optimal solutions efficiently without requiring additional computational overhead. Therefore, the adopted parameters are both theoretically motivated and empirically validated to ensure robust and efficient operation for the UC-CFmMIMO uplink power control problem. SE serves as the main performance metric, evaluated through cumulative distribution function (CDF) curves and average SE measures to characterize both fairness and throughput trends across various network configurations.

A. Effectiveness of proposed scheme

The effectiveness of the proposed uplink power control schemes is validated through extensive numerical experiments, as illustrated in Figs. 2–5. The experiments were performed on a Windows Server 2019 using MATLAB R2023a with two Intel® Xeon® Gold 5115 Processors to assess computational performance and convergence efficiency.

Figure 2 depicts the convergence behavior of the normalized fitness functions corresponding to the two optimization formulations (F1-GWO for fairness-oriented P1 and F2-GWO for throughput-oriented P2). Both formulations exhibit rapid convergence toward optimality, with F1-GWO stabilizing after approximately 220 iterations and an average computation time of 5.25 ms. The slower convergence of F1-GWO reflects the complexity of achieving balanced SE distribution among UEs. In contrast, F2-GWO reaches convergence almost instantly because maximizing the sum SE inherently corresponds to full-power transmission, which is evaluated at initialization.

After 50 iterations, the normalized fitness values of F1-GWO and F2-GWO reach 0.96214 and 0.99991, respectively, confirming the high convergence efficiency of the proposed algorithm. These results demonstrate that the selected configuration (a population size of 300, 50 iterations) achieves near-optimal performance with minimal computational cost, providing a strong balance between convergence accuracy and runtime efficiency.

The strong convergence behavior observed in both F1-GWO and F2-GWO highlights the algorithm's potential for near real-time applicability in UC-CFmMIMO systems. With an average computation time of only a few milliseconds per optimization round, the proposed framework can efficiently adapt to moderate variations in user distribution or channel conditions within a coherence block. Given that the uplink power control problem is quasi-static over short time intervals, the GWO process can be periodically reinitialized or triggered by network dynamics to update transmission powers with negligible latency. These attributes make the proposed approach particularly suitable for practical deployments requiring low-latency adaptation and consistent trade-offs between fairness and throughput.

To benchmark SE performance, Figs. 3–5 compare the proposed F1-GWO and F2-GWO schemes against conventional FPA and FPC. At CDF $= 0.1$, the F1-GWO scheme achieves 3.39-bit/s/Hz, outperforming FPA (3.18-bit/s/Hz). At CDF $= 0.5$, F1-GWO reaches 4.24-bit/s/Hz, while F2-GWO attains 5.66-bit/s/Hz, exceeding FPA (3.90-bit/s/Hz). These improvements indicate that GWO enhances SE optimization through dynamic adaptation of search agents, leading to superior power allocation.

The fairness performance comparison in Fig. 4 reveals that F1-GWO consistently achieves higher minimum SE than both FPC and F2-GWO, confirming its robustness in supporting users with weak links. At CDF $= 0.5$, F1-GWO records 3.87-bit/s/Hz, surpassing FPC (3.15-bit/s/Hz) and F2-GWO (3.14-bit/s/Hz). The gain in minimum SE demonstrates that GWO effectively mitigates interference in decentralized UC-CFmMIMO networks, where local AP-UE associations cause heterogeneous link qualities.

Figure 5 illustrates the sum SE performance. At CDF $= 0.1$, F2-GWO and FPC both reach 107.0-bit/s/Hz, while F1-GWO achieves 76.6-bit/s/Hz, outperforming FPA (63.7-bit/s/Hz). At CDF $= 0.5$, F2-GWO maintains parity with FPC (118.99-bit/s/Hz), and

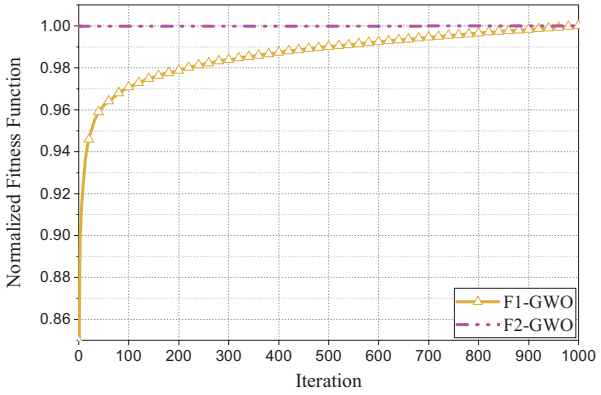

Fig. 2. Convergence of the normalized fitness functions for the two optimization objectives: F1-GWO (fairness-oriented) and F2-GWO (throughput-oriented). The F1-based GWO scheme converges after around 220 iterations, whereas the F2-based GWO converges instantly, confirming the rapid convergence and computational efficiency of GWO.

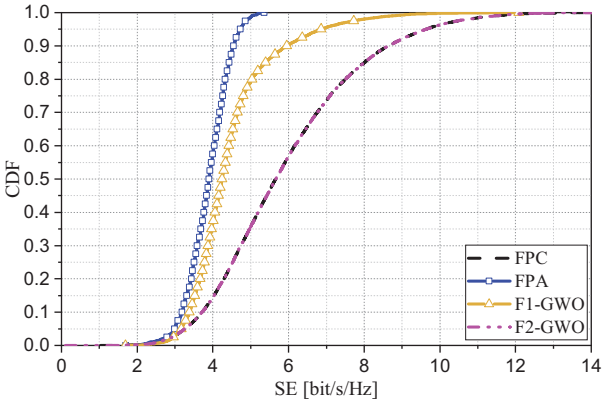

Fig. 3. Cumulative distribution of SE per user for different uplink power control schemes. The proposed F1- and F2-based GWO schemes outperform conventional FPA and FPC methods, achieving higher median and tail SE values.

F1-GWO continues to exceed FPA (89.98-bit/s/Hz vs. 77.97-bit/s/Hz). These results confirm that GWO can achieve comparable or superior throughput performance to conventional benchmark schemes while maintaining better fairness balance.

In summary, the proposed GWO-based schemes provide a comprehensive balance between fairness and SE while demonstrating computational efficiency and scalability advantages. The additional comparative insights and interpretation presented here strengthen the understanding of the proposed method's value and its distinction from prior optimization approaches in UC-CFmMIMO systems.

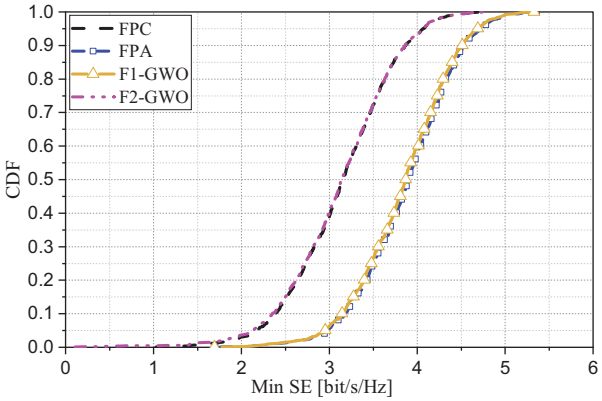

Fig. 4. Minimum SE comparison among power control schemes. The fairness-oriented F1-GWO scheme provides the highest minimum SE, demonstrating improved user fairness relative to FPC, FPA, and F2-based GWO.

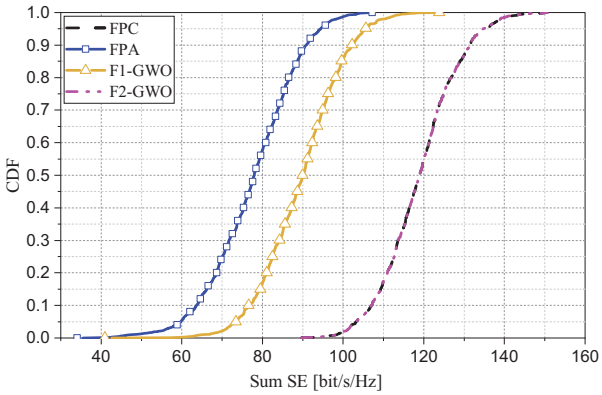

Fig. 5. Sum SE comparison among power control schemes. The F2-GWO scheme achieves throughput comparable to FPC while the F1-GWO surpasses FPA, confirming the efficiency of GWO in optimizing both fairness and throughput.

B. Impact of number of APs and UEs

This section investigates the influence of AP and UE scaling on system performance in terms of the average minimum SE and sum SE. The evaluation further includes the BA for comparative analysis, employing the same optimization objectives as the proposed GWO schemes. The additional F1-BA and F2-BA cases provide a relevant benchmark, as BA has been previously adopted for centralized uplink power control in UC-CFmMIMO systems [26].

Figure 6 demonstrates that increasing the number of APs enhances average minimum SE due to improved spatial diversity and reduced signal attenuation. At 200 APs, F1-GWO achieves 6.02-bit/s/Hz, higher than FPA (5.95-bit/s/Hz) and F1-BA (5.84-bit/s/Hz), confirming the superior fairness control capability of

GWO. The F2-GWO scheme also attains 5.28-bit/s/Hz, outperforming FPC (5.18-bit/s/Hz) and F2-BA (5.21-bit/s/Hz). These results indicate that GWO achieves better exploitation of distributed resources and faster convergence toward balanced power allocation compared with BA.

Figure 7 shows that the average sum SE improves with more APs, benefiting throughput-oriented schemes. At 200 APs, F2-GWO reaches 157.85-bit/s/Hz, exceeding both FPC (156.44-bit/s/Hz) and F2-BA (157.07-bit/s/Hz). Similarly, F1-GWO attains 130.62-bit/s/Hz, outperforming FPA (119.04-bit/s/Hz) and F1-BA (124.86-bit/s/Hz). The consistent gain over BA highlights the adaptability of GWO in complex multi-dimensional search spaces and its robustness to local optima.

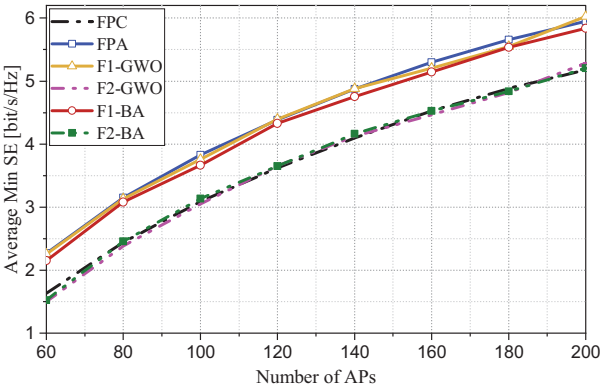

Fig. 6. Average minimum SE versus number of APs. Increasing APs enhances spatial diversity and fairness. F1-GWO achieves the highest SE (6.02-bit/s/Hz at 200 APs), outperforming F1-BA and FPA, highlighting GWO's superior resource utilization and convergence.

When the number of UEs increases, inter-user interference becomes dominant, causing a reduction in minimum SE for all schemes. Figure 8 shows that F1-GWO maintains higher minimum SE across all user densities. For instance, at 30 UEs, F1-GWO records 2.78-bit/s/Hz, compared to 2.53-bit/s/Hz (F1-BA), 2.80-bit/s/Hz (FPA), and 1.83-bit/s/Hz (FPC). This confirms that the fairness-oriented F1 formulation stabilizes user performance even under increased network loading.

In contrast, Fig. 9 reveals that total SE rises with the number of UEs because more concurrent uplink transmissions contribute to overall throughput. F2-GWO shows the highest growth, from 69.42 to 148.32-bit/s/Hz as UEs increase from 10 to 30, outperforming both FPC (70.46- to 146.85-bit/s/Hz) and F2-BA (70.63- to 147.24-bit/s/Hz). Furthermore, F1-GWO consistently surpasses FPA (51.99- to 115.63-bit/s/Hz versus 49.91- to 84.12-bit/s/Hz) and F1-BA (46.84- to

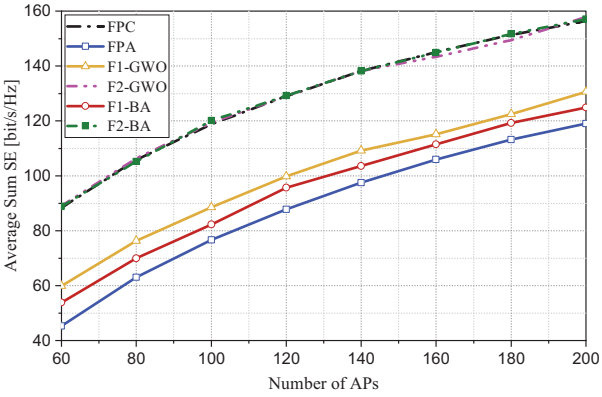

Fig. 7. Average sum SE versus number of APs. Both GWO-based schemes show steady throughput improvement as APs increase. F2-GWO attains 157.85-bit/s/Hz at 200 APs, exceeding FPC and F2-BA, confirming better scalability and optimization robustness.

105.23-bit/s/Hz), proving that fairness-oriented GWO retains competitive throughput.

Overall, the results confirm that both proposed schemes, F1-GWO for fairness optimization and F2-GWO for throughput maximization, achieve superior trade-offs compared with BA and conventional benchmarks. The study differs from our prior work by extending power-control optimization to the UC-CFmMIMO framework under centralized uplink operation, incorporating GWO as an adaptive metaheuristic alternative to BA, and providing a more detailed scalability analysis with respect to both AP and UE densities. These outcomes emphasize the efficiency, robustness, and generalization capability of the proposed GWO-based formulations for UC-CFmMIMO uplink systems.

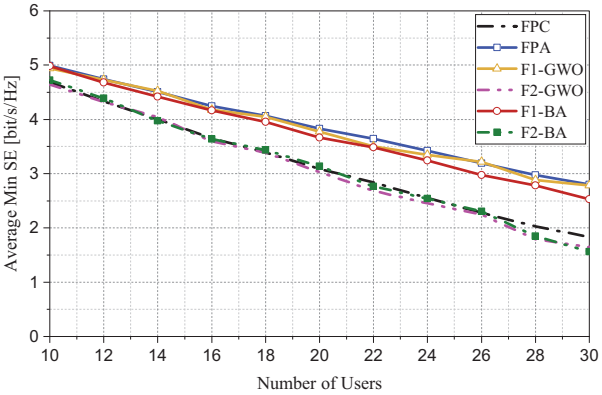

Fig. 8. Average minimum SE versus number of UEs. As UE density rises, inter-user interference reduces SE for all methods. F1-GWO consistently maintains higher fairness, outperforming F1-BA and FPC, especially under heavy network loading.

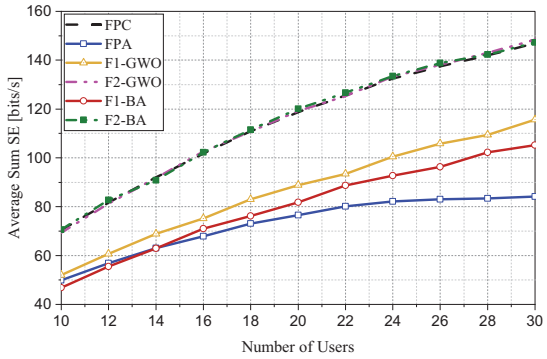

Fig. 9. Average sum SE versus number of UEs. Throughput increases with user density, and F2-GWO exhibits the steepest growth, outperforming both BA- and FPC-based counterparts. F1-GWO also achieves superior throughput compared with FPA and F1-BA, verifying its robustness across network scales.

Although the simulations are conducted for sub-6 GHz UC-CFmMIMO systems, the proposed GWO-based optimization framework is not limited to a specific frequency band or communication standard. Its metaheuristic structure can accommodate varying system models by redefining the spectral-efficiency function or power constraints according to the target standard (e.g., mmWave or 6G massive MIMO). Moreover, the algorithmic scalability demonstrated across different AP and UE densities suggests strong adaptability to heterogeneous and evolving network environments. Future work may extend this analysis to include diverse communication standards and dynamic user distributions to further validate the robustness and generalization capability of the proposed approach.

VI. CONCLUSION

This paper presents a GWO-based uplink power control framework for UC-CFmMIMO systems, addressing fairness and throughput optimization through two formulations: F1-GWO for max-min fairness and F2-GWO for sum-SE maximization. The proposed approach achieves rapid and stable convergence, with F1-GWO reaching approximately 96% of its optimal normalized fitness and F2-GWO nearly full convergence (approximately equal to 100%) within 50 iterations. The average computation time of only a few milliseconds per optimization cycle highlights its feasibility for near real-time implementation. Numerical evaluations demonstrate that F1-GWO significantly enhances user fairness, while F2-GWO achieves throughput comparable to full-power transmission, both outperforming BA and conventional optimization schemes across various AP and UE densities. These outcomes confirm the robustness, scalability, and practical potential of the GWO framework for centralized UC-CFmMIMO uplink power control in future intelligent and adaptive wireless networks.

Despite its efficiency and adaptability, the GWO-based approach remains a data-agnostic metaheuristic that relies on iterative search rather than learning from prior network states. As such, it performs reactive optimization after network changes rather than proactive adaptation. Additionally, the current analysis focuses on static user distributions and sub-6 GHz operation, without explicitly modeling long-term temporal correlations or heterogeneous communication standards.

Future work will extend this study toward learning-based optimization frameworks that integrate GWO with machine learning or reinforcement learning. Such hybrid models could predict user mobility, channel variations, or traffic dynamics to enable proactive and context-aware power control. Further research will also investigate multi-objective formulations, joint uplink-downlink optimization, and online adaptation across diverse communication standards (e.g., mmWave and 6G networks), enhancing the generalization capability of the proposed framework in dynamic and large-scale wireless environments.

REFERENCES

[1] J. Wei and F. Luo, *6G Key Technologies: A Comprehensive Guide*. New Jersey, NJ: Wiley-IEEE Press, pp. 447–463, 2023.

[2] Y. Zhao, I. G. Niemegeers, and S. H. D. Groot, "Power control in cell-free massive MIMO: A deep learning method," *IEEE Access*, vol. 8, pp. 87185–87200, 2020.

[3] E. Björnson and L. Sanguinetti, "Making cell-free massive MIMO competitive with MMSE processing and centralized implementation," *IEEE Trans. Wireless Com.*, pp. 77–90, 2020.

[4] A. Zhou, J. Wu, E. G. Larsson, and P. Fan, "Max-min optimal beamforming for cell-free massive MIMO," *IEEE Commun. Lett.*, vol. 24, no. 10, pp. 2344–2348, 2020.

[5] Ö. T. Demir , E. Björnson, and L. Sanguinetti, "Foundations of user-centric cell-free massive MIMO," *Foundations and Trends in Signal Processing*, vol. 14, no. 3–4, pp. 162–472, 2021.

[6] T. V. Luyen, N. V. Cuong, and P. D. Hung, "Convex optimization-based linear and planar array pattern nulling," *Progress in Electromagnetics Research M*, vol. 128, pp. 21–30, 2024.

[7] M. Bashar, K. Cumanan, A. G. Burr, M. Debbah, and H. Q. Ngo, "On the uplink max-min SINR of cell-free massive MIMO systems," *IEEE Trans. Wireless Commun.*, vol. 18, no. 4, pp. 2021–2036, 2019.

[8] M. Bashar, K. Cumanan, A. G. Burr, H. Q. Ngo, M. Debbah, and P. Xiao, "Max-min rate of cell-free

massive MIMO uplink with optimal uniform quantization," *IEEE Trans. Commun.*, vol. 67, no. 10, pp. 6796–6815, 2019.

[9] Y. Zhang, H. Cao, and L. Yang, "Max-min power optimization in multigroup multicast cell-free massive MIMO," *Proc. IEEE WCNC*, pp. 1–6, 2019.

[10] H. Q. Ngo, L. N. Tran, T. Q. Duong, M. Matthaiou, and E. G. Larsson, "On the total energy efficiency of cell-free massive MIMO," *IEEE Trans. Green Com. Netw.*, pp. 25–39, 2018.

[11] M. Bashar, K. Cumanan, A. G. Burr, H. Q. Ngo, and H. V. Poor, "Mixed quality of service in cell-free massive MIMO," *IEEE Commun. Lett.*, vol. 22, no. 7, pp. 1494–1497, 2018.

[12] M. Bashar, H. Q. Ngo, A. G. Burr, D. Maryopi, K. Cumanan, and E. G. Larsson, "On the performance of backhaul constrained cell-free massive MIMO with linear receivers," in *Proc. 52nd Asilomar Conf. Signals Syst. Comput.*, pp. 624–628, 2018.

[13] E. Nayebi, A. Ashikhmin, T. L. Marzetta, H. Yang, and B. D. Rao, "Precoding and power optimization in cell-free massive MIMO systems," *IEEE Trans. Wireless Commun.*, vol. 16, no. 7, pp. 4445–4459, 2017.

[14] H. Q. Ngo, A. Ashikhmin, H. Yang, E. G. Larsson, and T. L. Marzetta, "Cell-free massive MIMO versus small cells," *IEEE Trans. Wireless Commun.*, vol. 16, no. 3, pp. 1834–1850, 2017.

[15] L. T. Trang, N. V. Cuong, H. T. P. Thao, and T. V. Luyen, "An unknown interference suppression scheme for advanced antenna systems," *Applied Computational Electromagnetics Society (ACES) Journal*, vol. 50, no. 3, pp. 192–202, 2025.

[16] S. Mirjalili, S. M. Mirjalili, and A. Lewis, "Grey wolf optimizer," *Advances in Eng. Soft.*, vol. 69, pp. 46–61, 2014.

[17] T. V. Luyen and N. V. Cuong, "Metaheuristics-based hyperparameter tuning for convolutional neural networks," *Springer Nature Switzerland*, pp. 41–54, 2024.

[18] H. Wang, F. H. Memon, X. Wang, X. Li, N. Zhao, and K. Dev, "Machine learning-enabled MIMO-FBMC communication channel parameter estimation in IIoT: A distributed CS approach," *Digit. Commun. Netw.,* vol. 9, no. 2, pp. 306–312, 2023.

[19] H. Wang, L. Xu, Z. Yan, and T. A. Gulliver, "Low-complexity MIMO-FBMC sparse channel parameter estimation for industrial big data communications," *IEEE Trans. Ind. Inf.,* vol. 17, no. 5, pp. 3422–3430, 2021.

[20] H. Wang, X. Li, R. H. Jhaveri, T. R. Gadekallu, M. Zhu, T. A. Ahanger, and S. A. Khowaja, "Sparse Bayesian learning based channel estimation in FBMC/OQAM industrial IoT networks," *Computer Communications*, vol. 176, pp. 40–45, 2021.

[21] K. Safari and F. Imani, "A novel fuzzy-BELBIC structure for the adaptive control of satellite attitude", in *Proceedings of the ASME 2022 International Mechanical Engineering Congress and Exposition. Volume 3: Advanced Materials: Design, Processing, Characterization and Applications; Advances in Aerospace Technology*, Columbus, Ohio, USA, 30 October–3 November 2022.

[22] B. Shafai, F. Zarei, and A. Moradmand, "Stabilization of input derivative positive systems and its utilization in positive singular systems," in *2024 10th International Conference on Control, Decision and Information Technologies*, vol. 5, pp. 615-620, 2024.

[23] L. T. Trang, N. V. Cuong, and T. V. Luyen, "Efficient constraint handling technique-based beamformer for advanced antenna systems," *Journal of Communications*, pp. 506–515, 2024.

[24] X.-S. Yang, *Nature-Inspired Optimization Algorithms*, 2nd ed. London: Academic Press, pp. 197–237, 2020.

[25] K. X. Thuc, H. M. Kha, N. Van Cuong, and T. Van Luyen, "A metaheuristics-based hyperparameter optimization approach to beamforming design," *IEEE Access*, vol. 11, pp. 52250–52259, 2023.

[26] T. V. Luyen and N. V. Cuong, "Metaheuristics-based uplink power control scheme for user-centric cell-free massive MIMO systems," *IEEE Access*, vol. 12, pp. 96603–96616, 2024.

Nguyen Van Cuong received the engineer's and master's degrees from Hanoi University of Industry, Vietnam, in 2020 and 2022, respectively. He is currently pursuing the Ph.D. degree at Vin University, Vietnam. His research interests include wireless communications, optimization, smart EV charging, green communications, and energy-efficient wireless networks.

Hoang Manh Kha received the B.E. and M.E. degrees in electronics and telecommunications engineering from the Hanoi University of Science and Technology, Vietnam, in 2002 and 2004, respectively, and the Ph.D. degree in communications engineering from the University of Paderborn, Germany, in 2016. His research interests include wireless communication, positioning engineering, and deep learning.

Tong Van Luyen has been a lecturer at Hanoi University of Industry, Vietnam, since 2002. He received the B.S. degree and M.S. degree from Hanoi University of Science and Technology in 2002 and 2004, respectively, and the Ph.D. degree from VNU University of Engineering and Technology in 2019. His research interests are beamforming and artificial intelligence.

Optimized Design of Shielding Structure for High Offset Tolerance WPT System Based on Fused Uncertainty Surrogate Model

T. H. Wang, K. F. Zhao, H. W. Duan, G. Lv, Q. Y. Yu, and S. S. Guan

College of Instrumentation & Electrical Engineering
Jilin University, Changchun 130026, China
wangtianhao@jlu.edu.cn, zhaokf23@mails.jlu.edu.cn, duanhw24@mails.jlu.edu.cn,
lvgang23@mails.jlu.edu.cn, qyyu20@mails.jlu.edu.cn, guanshanshan@jlu.edu.cn

Abstract – In the practical application of wireless power transfer (WPT), an offset between the coupling mechanisms can lead to an increase in harmful leakage of magnetic fields around the system and a decrease in the efficiency of energy transfer. In this paper, we propose to use the uncertainty quantitative surrogate model to guide optimal design of the shielding structure in order to reduce the leakage magnetic field and improve energy transfer efficiency, taking into account the positional offsets of the WPT system in use. In this paper, the uncertainty of the leakage magnetic field and the energy transfer efficiency of the WPT system is quantified based on the improved Transformer surrogate model of the Kolmogorov-Arnold Network, and computational time cost is reduced by 90.97%. The multi-objective exponential distribution optimizer is combined with a surrogate model to obtain the robust optimal structure under the influence of bias. Finally, it is experimentally verified that the robust optimal structure is able to maintain both low leakage magnetic field and high energy transfer efficiency under the influence of offset. Compared with the traditional deterministic optimal structure, the mean of the energy transfer efficiency of the robust optimal structure is increased by 4.95%, and the probability of overrun is reduced to 0. Experiments demonstrate that the robust structure can improve the offset tolerance of the system more effectively and ensure the electromagnetic safety of users at the same time.

Index Terms – Exponential distribution optimizer, robust optimization, transformer, uncertainty quantification, wireless power transfer.

I. INTRODUCTION

Electromagnetic safety issues generated during the operation of wireless power transmission (WPT) are current research hotspots in the field of WPT. WPT technology realizes safe and convenient charging, which is widely used in the fields of medical devices [1], electric bicycles [2], unmanned aerial vehicles [3], and electric vehicles [4–6]. However, the energy transfer structure of the WPT system is a loosely coupled form, which inevitably generates leakage electromagnetic fields (LMF) during operation, thus the energy transfer efficiency becomes lower. In addition, due to the effect of offset uncertainty between the coupling mechanisms of the WPT system in the actual application process, the operating state of the system also has uncertainty [7, 8]. To ensure the safety of WPT products in use, the International Commission on Non-Ionizing Radiation Protection (ICNIRP) and the Institute of Electrical and Electronics Engineers (IEEE) have developed LMF standard limits for WPT systems to guide electromagnetic safety assessment [9–11]. Among them, ICNIRP uses the operating frequency of WPT systems as the basis for division and establishes limit values for different frequency bands for guidance. The WPT system used in this paper operates at a frequency of 85 kHz, with magnetic flux density B in the environment serving as the evaluation target for the electromagnetic safety of the WPT system. Therefore, it is necessary to design a reasonable electromagnetic shielding structure so as to limit the LMF caused by the uncertainty of the operating state of the WPT system, in order to improve the electromagnetic safety and energy transfer efficiency of the WPT system [12, 13].

Various electromagnetic active and passive shielding measures have been proposed for LMF of WPT systems. Among them, passive shielding is highly flexible, secure, adaptable to the environment, and used in a wide range of scenarios [14, 15]. The use of transmitting or receiving coils in combination with aluminum plates and ferrite materials is the most common passive shielding measure. Fu et al. [16] proposed a new ferrite composite structure that can effectively control the magnetic flux and improve efficiency. Covering a large area with ferrite poses a challenge in designing a compact WPT system since ferrite is limited by its weight, fragility, and large variation of magnetic properties with temperature. Li et al. [17] considered nanocrystalline as an alternative to ferrite cores because of the superior magnetic properties

Submitted On: June 07, 2025
Accepted On: October 25, 2025

https://doi.org/10.13052/2025.ACES.J.401105

and mechanical properties. Gaona et al. [18] utilized nanocrystalline cores to design magnetically conductive structures, achieving higher efficiency and power density with lower LMF compared to ferrite cores. The electromagnetic shielding structures in the above studies are usually designed based on deterministic state optimization. However, since the offset uncertainty between coupling mechanisms of WPT systems is unavoidable, the traditional optimization method is not applicable to cases where there is an offset between coupling mechanisms, resulting in an incomplete analysis of the above results. Therefore, the optimization design work of shielding structures considering the effect of offset uncertainty between coupling mechanisms of WPT systems is necessary.

The idea of optimizing the design while considering the uncertainty factors of the actual operating state of the system is called robust design optimization (RDO). The uncertainty quantification method based on agent model can solve the problems of the many variables involved in the RDO process and the high optimization costs. Lagouanelle et al. [19] considered the uncertainty of WPT systems and evaluated the uncertainty of the LMF of WPT systems using Kriging and the polynomial chaotic unfolding agent model, which helps in the design of shielding structures for EV-WPT systems. However, PCE will be limited by the probability-driven limitation, and the accuracy of the realized surrogate model is somewhat insufficient. In recent years, deep learning-based surrogate modeling methods have been widely used. Wang et al. [20] proposed a Bayesian neural network-based uncertainty quantification method to realize electromagnetic safety assessment of a human body containing medical implants around WPT systems. Transformer architecture is widely used in the solution of various nonlinear problems and is able to achieve accurate surrogate models using fewer training samples and training time [21, 22]. However, the above studies did not incorporate the uncertainty factor into the robust optimization design. Since the offset between the coupling mechanisms of WPT systems will lead to an increase of LMF and decrease of energy transfer efficiency at the same time, this paper considers the effects of the uncertainty of the offset between the coupling mechanisms of the WPT system in the optimization design of the shielding structure of the WPT system, which can strengthen the offset tolerance of the WPT system, and it is of great significance to enhance the stability of the energy transfer efficiency and electromagnetic safety. The main contributions of this paper are as follows.

Firstly, a WPT electromagnetic shielding structure with the combined effects of ferrite cells, aluminum plates and nanocrystals are proposed to realize the shielding of LMF with high efficiency energy transfer. Further, an uncertainty quantification method based on the Kolmogorov-Arnold Network (KAN) improved Transformer (K-Trans) surrogate model is proposed to realize the quantification of offset uncertainty among coupled bodies of WPT systems. Finally, combining the K-Trans surrogate model with the multi-objective exponential distribution optimizer (MOEDO) optimization algorithm for the robust optimization of the electromagnetic shielding structure of the WPT system. Experimental results show that the LMF of the WPT system is significantly reduced under the influence of offset uncertainty, while the energy transfer efficiency is significantly improved.

The main contents of this paper are as follows. Section II describes the working principle of WPT systems and the mechanism of shielding structures. Section III describes the mechanism of implementing the multi-objective robust optimization algorithm based on the K-Trans surrogate model combined with MOEDO. Section IV introduces the combined shielding structure proposed in this paper and implements the robust optimization of the shielding structure based on K-Trans combined with MOEDO and compares the shielding effect of different optimized structures under the influence of offset uncertainty. Section V describes the experimental part of this paper and verifies the superiority of the robust optimal structure of this paper by building the experimental platform of the WPT system. Section VI summarizes the work in this paper.

II. WPT SYSTEM AND ELECTROMAGNETIC SHIELDING

A. WPT system

The overall structure of the WPT system is shown in Fig. 1. The WPT system established in this paper is realized based on the principle of magnetic coupling resonance, where a current flows in the coupling coil and, since the transmitting coil and the receiving coil have the same resonance frequency, a resonant electromagnetic field can be generated to realize efficient wireless transmission of electric energy through the electromagnetic field. In order to ensure maximum efficiency of the WPT system during normal operation, a bilateral S-S compensation circuit is used in this paper, as shown in Fig. 2, where U_S is the excitation source, R_{S1} is the equivalent resistance of Tx, C_{S1} is the series compensation capacitor at the Tx end, L_1 and L_2 are the coil self-inductance at the Tx and Rx ends, M is the coil mutual inductance between Tx and Rx, C_{S2} is the series compensation capacitor at the Rx end, R_{S2} is the equivalent resistance of Rx, and R_L is the load resistance. To ensure the transmission efficiency of the

WPT system, the S-S compensation circuit should be in resonance. The circuit parameters at the transmitter and receiver ends are shown in equations (1) and (2).

$$\omega L_1 = \frac{1}{\omega C_1}, \tag{1}$$

$$\omega L_2 = \frac{1}{\omega C_2}, \tag{2}$$

where ω is the resonant angular frequency, $\omega = 2\pi f$, and f is the resonant frequency. In this paper, f is chosen to be 85 kHz for the WPT system, which is the most likely candidate frequency for the WPT system [22].

B. Electromagnetic shielding

In the WPT system, the coupled electromagnetic field between the coupling coils is the core of realizing energy transfer. The shielding structure directs the electromagnetic field through the nature of the material, increasing the efficiency of energy transfer and simultaneously weakening the electromagnetic field in non-operating areas. Electrical shielding materials exploit their high electrical conductivity to induce eddy currents when exposed to a magnetic field. These eddy currents generate an opposing magnetic flux that suppresses field leakage and simultaneously dissipates energy as Joule heat, thereby attenuating the LMF.

The equation for the eddy current induced electromotive force E generated by the alternating electromagnetic field on the outside of the shielding material is:

$$\nabla \times E = -\frac{\partial B}{\partial t}. \tag{3}$$

The density of eddy currents generated by the induced electromotive force is:

$$\nabla \times \frac{1}{\mu}(\nabla \times A) = (-\nabla\phi - j\omega A)(\sigma + j\omega\varepsilon), \tag{4}$$

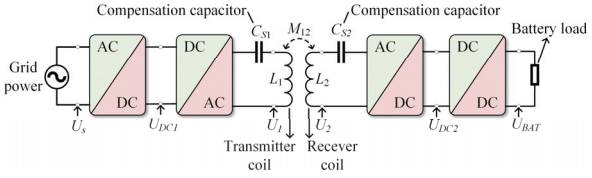

Fig. 1. WPT system schematic.

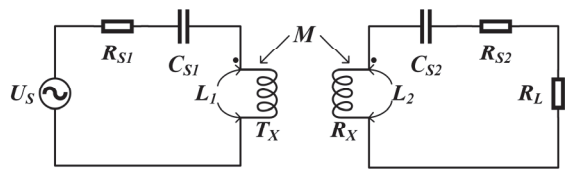

Fig. 2. S-S compensation circuit.

where ϕ represents the electric potential, A is magnetic vector, σ is material conductivity, μ is relative permeability of the material, ε is dielectric constant, and j is an imaginary unit. The eddy currents generated in the shielding mechanism can be expressed by the volume fraction:

$$I = \int_V (-\nabla\phi - j\omega A)(\sigma + j\omega\varepsilon)dV. \tag{5}$$

From equation (5) it can be seen that eddy currents are affected by the system operating angular frequency ω, the conductivity σ and dielectric constant ε of the shielding material. However, electrical materials also have drawbacks, such as affecting the magnetic field state around the receiving coil, and eddy currents generate heat, which not only increases transmission losses but also causes safety hazards. Therefore, the current WPT shielding structure is usually a combination of electrical and magnetic materials, which reduces energy loss and improves system efficiency to have better shielding performance.

The location, shape and size of the shielding material can be varied during design to suit the actual application. Because magnetic field lines naturally form closed loops and cannot be directly blocked, we can design specialized magnetic conduction pathways to keep the magnetic field primarily circulating within the equipment. This significantly reduces magnetic field leakage to the outside, achieving effective shielding. There is a relationship in the magnetic field:

$$\Phi = \frac{F_m}{R_m}, \tag{6}$$

where Φ is magnetic flux, F_m is the magnetomotive force, which is determined by the product of the number of turns of the coil and the current, and R_m is the magnetoresistance, which represents the hindering effect of the magnetic circuit on the magnetic flux. Analysis of the relationship between the quantities in equation (6) shows that magnetic flux mainly passes through the shielding material with low reluctance and high relative permeability, which reduces magnetic leakage into the air. In constructing the magnetic field shielding mechanism, the low magnetoresistance path is shown in Fig. 3.

In the design of the magnetic shielding mechanism, in addition to considering the shielding effect, it is also

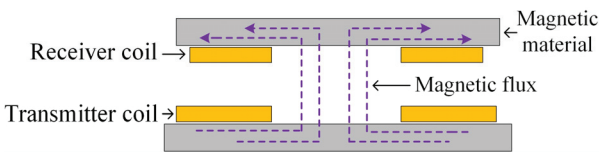

Fig. 3. Magnetic flux path.

necessary to synthesize the requirements of the use of the environment to make changes to the shape and weight of the shielding mechanism. The WPT system in this paper operates at 85 kHz, mainly utilizing a high relative permeability shield to shunt the magnetic flux and improve coupling between the transceiver coils. It can be seen that magnetic induction intensity inside the high relative permeability shield is much larger than that outside, while the magnetic lines of force in the low relative permeability material are almost perpendicular to the high relative permeability material. In this way most of the low-frequency magnetic field energy is constrained to pass inside the shield, thus providing shielding.

III. ROBUST OPTIMIZATION BASED ON K-TRANS SURROGATE MODEL

The core of solving robust optimization problems is to take offset uncertainty into account in the optimal design in order to attenuate the effect of offset uncertainty. Existing methods usually require a large number of samples and are usually handled in a probability-driven manner, which may lead to an increase in computational time cost with large errors in the results. Considering the complexity and high simulation cost of WPT systems, this paper adopts the K-Trans based method to realize the embedding of the effect of offset uncertainty among coupled mechanisms of WPT systems to achieve robust optimization.

A. K-Trans surrogate model

Transformer is able to react more sensitively to changes in the dataset due to the remote dependency of its multi-head self-attention mechanism, providing better adaptability for regression tasks [23, 24]. The traditional Transformer has a multi-layer perceptron (MLP) layer after the self-attention layer. In MLP, the neuron connections are usually a real value representing the weights, and the neuron itself is equipped with a nonlinear activation function, usually a sigmoid function. The computation process of MLP is to first weight the inputs of the weights weighting and then introducing nonlinearity through the activation function. KAN is realized based on the Kolmogorov-Arnold (K-A) representation theorem, which shows that any continuous function $f(x_1,\ldots x_n)$ can be represented as a nested combination of finitely many univariate functions:

$$f(x)=\sum_{q=1}^{2n+1}\theta_q\left(\sum_{p=1}^{n}\delta_{q,p}(x_p)\right), \tag{7}$$

where $\delta_{q,p}$ and θ_q are univariate functions. KAN utilizes the K-A representation theorem to represent the weight parameters as a kind of B-spline. The B-spline function connects the two neurons directly and is essentially a segmented polynomial function that achieves a high degree of smoothing where the polynomial blocks intersect. The K-A theorem states a high-dimensional function through equation (7), which can be reduced to learning one-dimensional functions of polynomial order. These one-dimensional functions are not always smooth functions that are easy to learn, and thus high-dimensional decomposition is achieved by parameterizing each one-dimensional function as a B-spline function [24]. In Transformer, by replacing the MLP with KAN, we can take advantage of the better interpretability of KAN to achieve self-learning of the activation function while moving the activation function to the "edge", so as to realize the smooth processing of the data, which not only learns the features, but also optimizes these learned features with high accuracy, thus obtaining a smooth function that approximates the data. This not only ensures the accurate approximation ability of high-dimensional functions but also decomposes the multi-dimensional function into a univariate function combination to simplify computational complexity. The improved model structure is shown in Fig. 4.

As can be seen from Fig. 4, the K-Trans model consists of four parts: model input, encoder, decoder and model output. The model input data $x=(x_1,x_2,\ldots,x_n)$ integrates the offset uncertainty of the WPT system with the design parameters of the shielding structure, and the maximum value of the magnetic field strength B_{max} and the system transmission efficiency η at the four fixed

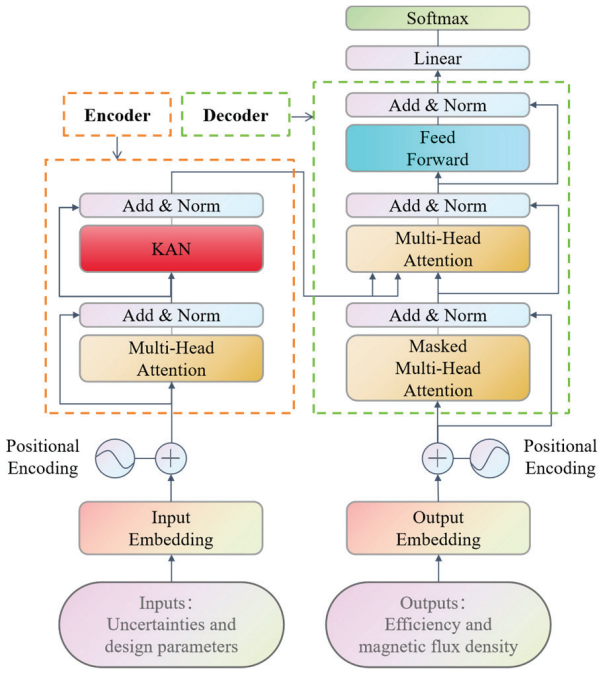

Fig. 4. K-Trans model.

observation points around the WPT system are used as the model outputs to realize the construction of the surrogate model under the uncertainty scenario.

Through the training of the above model, the LMF and energy transfer efficiency surrogate model of the WPT system containing the effect of the offset uncertainty between the coupling mechanisms of the WPT system is obtained. By calling the surrogate model through the MC method, the corresponding outputs are obtained, which are used to assist the optimization. Based on these samples, simulation can be replaced thus saving the time cost of the optimization process. The accuracy of the surrogate model in this paper is verified by comparing it with the MC method.

B. Optimization design method

Based on the above K-Trans uncertainty surrogate model, we quantify the effect of uncertainty surrogate into the optimization design process, and in the optimization stage we only consider the optimization of the design parameters, while the offset uncertainty is embedded into the optimization process, which is regarded as the optimization background factor, so as to achieve robust optimization. To address the above problems, this paper adopts an intelligent optimization algorithm for computation. MOEDO is a heuristic method [25] that utilizes the theory of exponential distribution combined with the idea of dynamic optimization. It integrates an information feedback mechanism (IFM) and transforms a multi-objective task into a single-objective sub-task, thereby overcoming the local optimum. The pseudo-code of the MOEDO algorithm is shown in Algorithm 1.

In the embedding operation of offset uncertainty, the design variables are always the same in both the robust optimization process and the traditional deterministic optimization process, the offset uncertainty variables are only used as stochastic inputs to the model, and the Pareto frontier searched by MOEDO is always for the optimization results with the design factors as variables. The optimization in the deterministic case and the robust optimization of the WPT system considering the effect of offset uncertainty can be achieved by the aforementioned MOEDO optimization method combined with the K-Trans surrogate model proposed in Appendix A.

IV. OPTIMIZED DESIGN OF SHIELDING STRUCTURE

A. Structural design

In the design of shielding structure, this paper adds ultra-thin single-layer nanocrystalline material with high relative permeability to realize the composite shielding structure based on the combination of aluminum plate and ferrite unit. The nanocrystalline material used in this study exhibits a relative permeability of 22,000 at room temperature and 85 kHz, whereas the ferrite component shows only 3300 under identical conditions. In the shielding design, inner peripheral nanocrystalline strips guide magnetic leakage from the coil center into coupling paths, while outer strips redirect leakage from non-operating regions back to active areas. Where the ferrite unit is used to compensate for the nanocrystalline material shielding loophole, and finally the aluminum plate is utilized for electrical shielding, and the three materials are placed in layers, as shown in Fig. 5.

Compared with the traditional shielding structure covered by a large area of ferrite, the use of nanocrystalline to replace part of the ferrite can achieve Compared with the traditional shielding structure covered by a large area of ferrite, the use of nanocrystalline to

Algorithm 1: MOEDO

Input: population size (*N*), maximum time (*Maxtime*), dimension (*d*), lower bound (*lb*) and upper bound (*ub*).

Output: Optimal solution $X_{winners}^{best}$.

1. Initialize population of *N* solutions: $X_{\boldsymbol{winners}}(i), \quad i=1,2,\ldots,N$.
2. Define *Fitness* vector to store the fitness of all solutions.
3. Construct the *memoryless* matrix such that $memoryless=X_{winnners}$。
4. while (*time*<*Maxtime*)
5. Define *V* matrix of size *s*. Rank the solutions in $X_{winners}$.
6. Calculate $X_{guide}^{time}=\frac{X_{winners}^{best1}+X_{winners}^{best2}+X_{winners}^{best3}}{3}$.
7. Define the EDO adaptive parameters *a*,*b*,*c*,*d* and *f*.
8. *for i*=1:*N*
9. *if* (α<0.5)
10. *Generate* ϕ， *update* V_i^{time+1} *,according to* ϕ *to selection formula*
$V_i^{time+1}=a\cdot(memoryless_i^{time}-\sigma^2)+b\cdot X_{guide}^{time}$
or
$V_i^{time+1}=b\cdot(memoryless_i^{time}-\sigma^2)+\log(\phi)\cdot X_{winners}^{time}$
else:
$V_i^{time+1}=X_{winners}^{time}-M^{time}+(cZ_1+(1-c)Z_2)$.
11. *end*
12. *end for*
13. Copy *V* to *memoryless.* Define new fitness vector to store the fitness.
14. Find the *bestfitness.* Updating the $Fitness_i$.
15. *end while*
16. *time*=*time*+1. Return $X_{winners}^{best}$ solution.

replace part of the ferrite can achieve the effect of reducing the overall weight of the WPT system, saving the space occupied by the shielding structure and improving the robustness of the overall structure. However, since the ferrite compensation unit in this paper is not symmetrically placed, the magnetic field distribution around the system is not symmetrical. In addition, the offset uncertainty between the coupling mechanisms also affects the overall shielding effect. Therefore, it is necessary to design the most suitable combination of shielding materials and placement form to ensure the best performance of the whole WPT system under the influence of offset uncertainty.

The WPT system in this paper consists of a transmitting coil *Tx*, a receiving coil *Rx*, two end-to-end shields and a converter circuit. The dimensions of both *Tx* and *Rx* are 200 × 200 cm, and the cross-sectional area of the coils is 1.3×10^{-5} mm^2. Both coils are composed of 15 turns coil, and the coil wires are made of metallic copper wrapped with an insulating layer on the outside. When *Tx* and *Rx* are aligned and the spacing between the coils is 5 cm, the system operates under ideal conditions, and the system input power of the WPT is 300 W with an operating frequency of 85 kHz. the distribution of the magnetic flux density B around the WPT before and after the addition of the shielding structure is shown in Fig. 6. Group 1 represents no shielding, Group 2 represents aluminum plate and ferrite combination shielding, and Group 3 represents aluminum plate, ferrite and nanocrystalline combination shielding before optimization. As shown in Fig. 6, during normal operation of the WPT system, the magnetic field distribution in the cross-sectional plane exhibits an outward dispersion pattern, with higher magnetic flux density concentrated at the coil center. After implementing the shielding structure, the magnetic field is effectively confined to the operating region, while the leakage fields on the upper and lower surfaces of the WPT system are significantly attenuated, thereby enhancing operational safety.

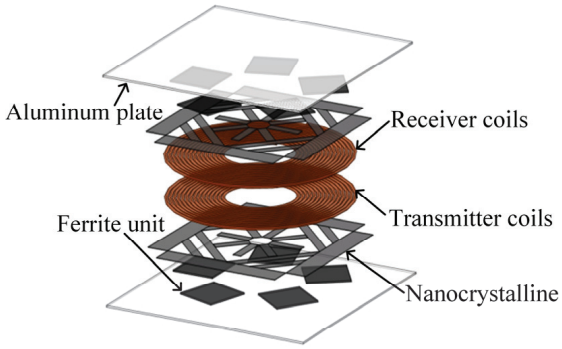

Fig. 5. WPT system combined shield structure.

The shielding structure design parameters and offset uncertainty tolerance range of the model in this paper are shown in Tables 1 and 2. Among them, the aluminum plate and the ferrite unit play a role in compensating the nanocrystalline shielding layer, so the material parameters and placement of the two are crucial. Therefore, the thickness of the ferrite unit t_1, the distance of the ferrite unit from the center of the WPT system d, the relative angle α of the upper and lower ferrite layers, and the thickness of the aluminum plate t_2 are taken as the optimization variables in this paper, so as to achieve the best matching effect with the nanocrystalline shielding layer. Since the offset between the coils of the WPT system is equiprobable in all directions, it is usually regarded as a uniform distribution in engineering applications, and U denotes a uniform distribution.

Currently, the most widely used electromagnetic exposure standard for WPT systems is the ICNIRP 2010 guideline, which divides different limit values for different WPT frequency ranges. The ICNIRP 2010 clearly states that, in order to ensure that the human body is not subjected to neurostimulation, in the frequency range of 3 kHz–10 MHz, the limit of the public's exposure to the time-varying magnetic field is 27 μT. The WPT system developed in this study operates at 85 kHz, with electromagnetic exposure compliance based on the ICNIRP 2010 occupational reference level of 27 μT for magnetic flux density. Since the magnetic flux density is higher at the vertical center located between the coils, this paper establishes four fixed observation points V_1, V_2, V_3, and V_4 in four directions in the middle of the vertical direction between the coupling mechanism, 20 cm from the center of the coils, for evaluating the shielding effect, as shown in Fig. 7.

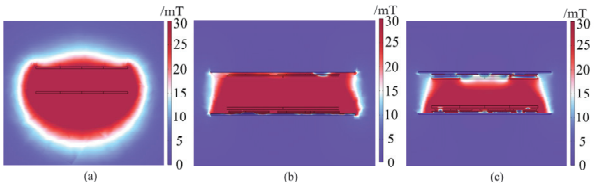

Fig. 6. Magnetic flux density distribution. (a) Group 1, (b) Group 2, (c) Group 3.

Table 1: Design variables and distribution parameters

Design Variables	Distribution Parameters	Unit
t_1	U [0,0.04]	m
d	U [0.002,0.004]	m
t_2	U [0.001,0.003]	m
α	U [0,72]	°

Table 2: Uncertainty factors and distribution parameters

Uncertainty Factors	Distribution Parameters	Unit
Horizontal offset ΔX	U [-0.05,0.05]	m
Vertical offset ΔY	U [-0.05,0.05]	m
Coil distance ΔZ	U [0.04,0.06]	m

B. Shielding performance

The magnetic field strength distribution and the energy transfer efficiency η of the WPT system at the four observation points with and without the shielding mechanism are shown in Fig. 8 and Table 3. Before and after adding Group 2 shielding to the WPT system in this paper, the maximum reduction of the B value at the four observation points reaches 85.19% but, at the same time, the system efficiency decreases by 7.2%, which is due to the fact that after adding the shielding layer, although the ambient leakage magnetic field becomes less, a part of the electrical energy is converted into thermal energy due to the eddy current effect of the aluminum plate, thus leading to a reduction of efficiency. The maximum value of the magnetic field strength at the four observation points is noted as B_{max}, which will be used as an indicator of the shielding effect of B_{max} in this paper because the shielding structure is asymmetric.

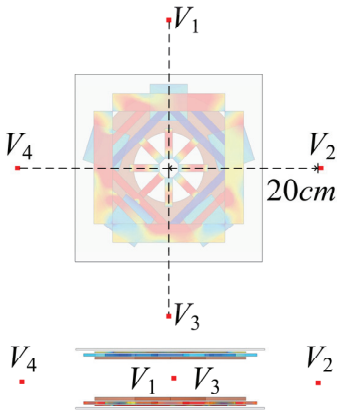

Fig. 7. Observation point.

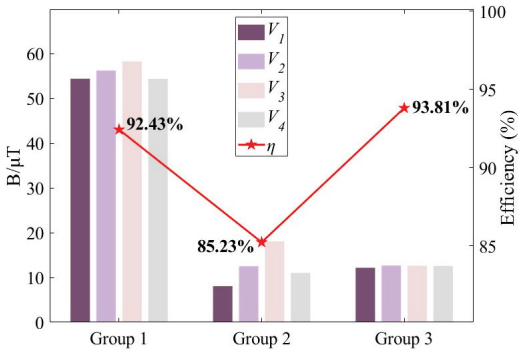

Fig. 8. Observation point indicators.

After adding the nanocrystalline shielding layer, compared with the form of Group 2 combination, the energy transfer efficiency of the WPT system is improved by 8.58% while B_{max} is reduced by 30.05%, which shows that the nanocrystalline material is able to improve the degree of system coupling due to its high relative permeability, resulting in the efficiency of the WPT system being elevated. In the optimization process of shielding structure design, what we need to find is the optimal thickness of the aluminum plate and ferrite unit as well as the optimal placement of the ferrite compensation unit, so as to achieve the optimal way of combining with nanocrystalline.

Considering the practical applications of the WPT system, according to the uncertainty factors and their distributions in Table 3, a random sampling method is used to sample and calculate the probability distribution function (PDF) of the energy efficiency of the original system and the maximum value of the magnetic field strength B_{max} at a fixed observation point. In order to validate the Transformer surrogate model before and after the improvement, the results are compared with the pre-improvement Transformer and MC calculations. Considering the cost of simulation computation, the MC method with 10,000 simulations can provide enough accuracy to meet the needs of most engineering problems. Comparison results are shown in Fig. 9. As can be seen from Fig. 9, the computational results of the K-Trans are basically consistent with those of the MC, and the computational accuracy is slightly improved over the MC and the Transformer. Under the presence of uncertainty, the mean value of the WPT system efficiency predicted by the surrogate model is 78.83%, and the mean value of the magnetic field strength B_{max} is 22.64 μT. As shown in Fig. 9 (a), the original structure of the WPT is subject to the possibility of transgressing the limit under the influence of the offset uncertainty, with a probability of 27.34%, and therefore the shielding structure needs to be optimized so as to reduce the transgressing probability.

Table 3: Observation point value

	Group 1	Group 2	Group 3
V_1/μT	54.42	8.06	12.17
V_2/μT	56.26	12.53	12.68
V_3/μT	58.27	18.07	12.64
V_4/μT	54.39	11.02	12.61

Table 4: Calculation time

	MC	Transformer	K-Tran
Time/min	22833	2290	2062

In addition, in terms of computation time, the time required to calculate the WPT system operation for a single scenario using the multi-physics field simulation software is 2 minutes and 17 seconds, and the computation time for the three methods in this paper for a single structure is shown in Table 4. It shows that under the condition of calculating the same WPT system structure, the calculation cost of 10,000 times MC method is very high, while the calculation time cost of K-Trans saves 90.97% compared to the MC method. Thus, the K-Trans method can ensure the realization of improved computational efficiency while guaranteeing accurate calculation results.

In the optimization process, determining the optimum does not consider other factors and is calculated directly through optimization. While robust optimization needs to consider the offset uncertainty among the coupled mechanisms of the WPT system, in this paper, the uncertainty effect is embedded into the optimization as a data background to realize robust optimization. For the WPT system, the B_{max} of the observation point is optimal while the system works efficiently. The design variables corresponding to the target points in the Parato solution set are shown in Table 5.

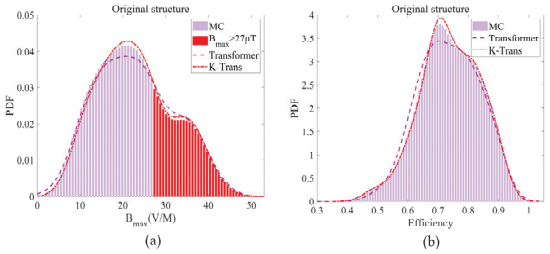

Fig. 9. PDF (a) B_{max} and (b) η.

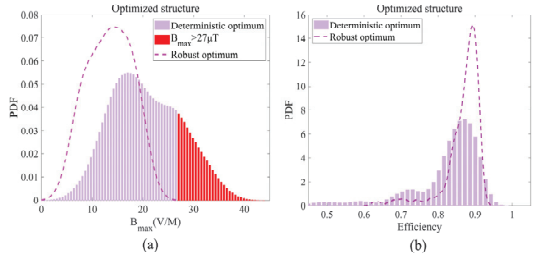

Fig. 10. Comparison of PDF of deterministic optimum and robust optimum (a) B_{max} and (b) η.

Table 5: Optimal design variables

	t_1/m	d/m	t_2/m	α/m
Deterministic optimum	0.003	0.032	0.0019	7
Robust optimum	0.004	0.025	0.0028	35

Table 6: Statistical parameter

	Original Structure	**Deterministic Optimum**	**Robust Optimum**
Mean of η/%	78.83	80.73	86.60
Mean of B_{max}/μT	22.64	20.63	13.42
Transgression probability P/%	27.34	19.09	0

In order to verify the improvement effect of the energy transfer efficiency and shielding performance of the WPT system under the influence of offset uncertainty, according to the parameter settings in Table 2 and the optimized parameters in Table 5, the probability distribution curves of η and B_{max} are calculated using the agent model and compared with the pre-optimization PDF, as shown in Fig. 10 and Table 6.

Results demonstrate that the robustly optimized system achieves a mean efficiency of 86.60% with an associated magnetic field strength of 13.42 μT. In contrast, the deterministically optimized structure shows significantly degraded performance, with mean efficiency dropping to 80.73% and magnetic field strength increasing to 20.63 μT. In addition, analyzing from the perspective of the transgressing probability, the transgressing probability of the deterministically optimal structure reaches 19.09%, whereas the robustly optimized structure demonstrates an overshoot probability of 0. The transgression probability of magnetic leakage of the WPT system is reduced to 0, and there is no possibility of transgression, which ensures the safety of electromagnetic exposure of the users. Therefore, the robust-optimized WPT system's offset resistance is improved, and the RDO method assisted by the K-Trans surrogate model can effectively cut down the negative impact caused by the offset uncertainty of the WPT system, and improve the stability of the system's electromagnetic shielding, transmission efficiency and safety of the users.

V. EXPERIMENTAL RESULTS

In order to validate the RDO method proposed in this paper, a 300 W, 85 kHz system is constructed to verify the effectiveness of the proposed method, and the system is shown in Figs. 11 and 12. The system consists of a coil, converter circuit, shield and resistive load. In this paper, the coil spacing adjustment is realized using acrylic pads that do not have any effect on the electromagnetic field. In the experiment, the measurement device of magnetic field strength is based on the ELT-400 series probes used for safety assessment of human exposure to magnetic fields under the German

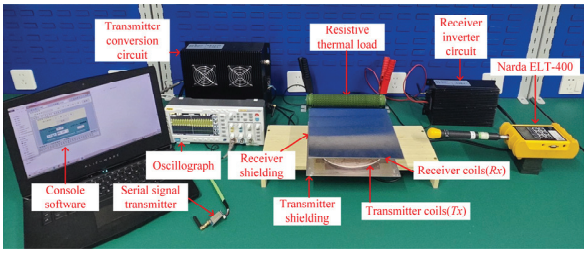

Fig. 11. Set up.

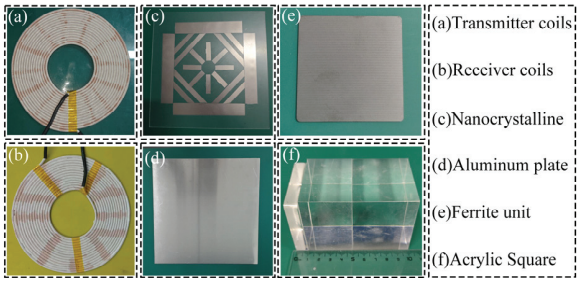

Fig. 12. Enlarged view.

company Narda, which meets the measurement standards of ICNIRP 2010.

From the simulation results in section IV, it can be seen that the shielding effect of deterministic optimal structure in the deterministic case is superior to that of the robust optimal value, which is verified in the following based on the experimental build. In the process of verifying the effect of robust optimal shielding structure, in this experiment, the step of the three uncertainty factors ΔZ, ΔX and ΔY are all set to 1 cm, the numerical planes of ΔZ with different coil spacing are used as a differentiation, and the data of $\Delta X - \Delta Y$ corresponding to the efficiency and the magnetic field strength under the case of ΔZ with different coil spacing are obtained to chart the four-dimensional response surface plots to verify the two kinds of structures under the influence of the uncertainty factors' shielding performance. From the distribution parameters of the uncertainty factors in Table 2, it can be seen that there are 363 possible combinations of the three uncertainty factors for each shielding structure in the experimental process at a step of 1 cm, and the response surface plots are realized at the resulting 363 points.

As shown in Figs. 13 and 14, the 3D response surface plots reveal significant differences between the robustly optimized structure and deterministic structure under asymmetric shielding conditions. The three coordinate axes represent positional offsets, with dual color scales indicating maximum magnetic flux density B_{max} and transfer efficiency η. Key findings include: at $\Delta Z = 4$ cm, the system achieves optimal performance balance, with the robust structure demonstrating 86.6% efficiency (4.95% improvement over deterministic design) and 13.4 μT B_{max} (5.17 μT reduction). This enhancement stems from adaptive coupling spacing adjustment in the robust framework, which simultaneously improves magnetic coupling efficiency through reduced coil separation and confines magnetic fields within operational zones. Under misalignment conditions, the robust design reduces B_{max} leakage by 34% while lowering exceedance probability from 12.3% to 0%, fully complying with ICNIRP 2010 27 μT safety limit. Statistical data in Table 7 confirm that, under various uncertainty factors, the robust optimization framework not only improves average efficiency by 4.95% but also ensures zero magnetic exceedance, providing an effective solution for handling positional offsets in practical deployments.

Experimental validation confirms that the robustly optimized structure significantly enhances both the offset resistance and shielding performance of the WPT system. Leveraging the K-Trans surrogate model, our methodology quantifies positional uncertainty impacts by constructing shielding performance surrogate models

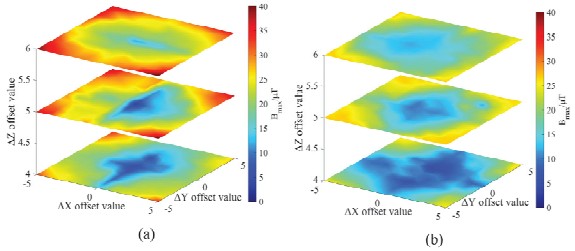

Fig. 13. Response surface plot B_{max} (a) deterministic optimum and (b) robust optimum.

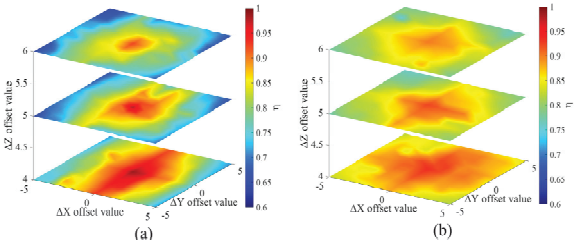

Fig. 14. Response surface plot η (a) deterministic optimum and (b) robust optimum.

Table 7: Statistical parameter

	Deterministic Optimum	**Robust Optimum**
Mean of η/%	79.84	84.79
Mean of B_{max}/μT	23.22	18.05
Transgression probability P/%	27.55	0

and deriving statistical parameters, while simultaneously enabling multi-objective robust optimization through MOEDO to improve shielding effectiveness and positional tolerance.

Comparative analysis reveals that, under positional uncertainty conditions, the K-Trans framework accurately captures shielding behavior patterns, and MOEDO achieves Pareto-optimal designs with 15.7% higher shielding efficiency and 42.3% greater positional tolerance compared to deterministic methods.

VI. CONCLUSION

The objective of this paper is to design highly offset-tolerant WPT shielding structures to counteract the negative effects of the offset uncertainty existing between the coupled mechanisms of the system and to improve the electromagnetic safety of the system. This paper proposes a robust optimization method based on the combination of K-Trans surrogate model and MOEDO. Its computational accuracy is basically the same as that of the MC method, and it noticeably saves the computational cost. From experimental results, K-Trans computational time cost is reduced by 90.97% compared with the MC method. The mean value of system efficiency with robust optimal structure is improved by 4.95% compared with the deterministic optimal structure, which effectively improves energy transfer efficiency. Mean of B_{max} is reduced by 5.17 μT, and the probability of system overrun is reduced to 0, which effectively protects the user's electromagnetic exposure safety. Therefore, the scheme proposed in this paper can provide an efficient and feasible solution for an optimized design of the shielding structure of WPT systems. Considering that the variables involved in practical applications are more complex, in future research we will look for more suitable methods for high-dimensional calculations to improve the safety and stability of WPT systems.

ACKNOWLEDGMENT

This work was supported in part by the Jilin Province and Changchun City Major Science and Technology Special Project 2024 Annual FAW Independent Innovation (Key Core Technology Research and Development) Major Science and Technology Special Project under Grant 20240301017ZD.

REFERENCES

[1] R. Jegadeesan, S. Nag, K. Agarwal, N. V. Thakor, and Y.-X. Guo, "Enabling wireless powering and telemetry for peripheral nerve implants," *IEEE J. Biomed. Health. Inform.*, vol. 19, no. 3, pp. 958–970, May 2015.

[2] G. D. Ntouni, A. S. Lioumpas, and K. S. Nikita, "Reliable and energy-efficient communications for wireless biomedical implant systems," *IEEE J. Biomed. Health. Inform.*, vol. 18, no. 6, pp. 1848–1856, Nov. 2014.

[3] S. Hong, Y. Kim, S. Lee, S. Jeong, B. Sim, H. Kim, J. Song, S. Ahn, and J. Kim, "A frequency-selective EMI reduction method for tightly coupled wireless power transfer systems using resonant frequency control of a shielding coil in smartphone application," *IEEE Trans. Electromagn. Compat.*, vol. 61, no. 6, pp. 2031–2039, Dec. 2019.

[4] L. Chaoqun, W. Xiaokang, W. Bin, and G. Yan, "Research on influence of the electric vehicle on life safety during the wireless charging process," in *2018 IEEE 2nd International Electrical and Energy Conference (CIEEC)*, Beijing, China, pp. 507–512, Nov. 2018.

[5] L. Fang, H. Zhou, W. Hu, X. Gao, H. Liu, and Q. Deng, "Design and analysis of flexible capacitive power transfer with stable output capability," *IEEE Transactions on Circuits and Systems. I: Regular Papers*, vol. 69, no. 11, pp. 4691–4701, Nov. 2022.

[6] D. Patil, M. K. McDonough, J. M. Miller, B. Fahimi, and P. T. Balsara, "Wireless power transfer for vehicular applications: Overview and challenges," *IEEE Trans. Transp. Electrif.*, vol. 4, no. 1, pp. 3–37, Mar. 2018.

[7] X. Shang, L. Xu, Q. Yu, L. Bo, G. Lv, Y. Chi, and T. Wang, "Uncertainty quantification and optimal design of EV-WPT system efficiency based on adaptive gaussian process regression," *Applied Computational Electromagnetics Society (ACES) Journal*, vol. 38, no. 12, pp. 929–940, Dec. 2023.

[8] T. Tan, T. Jiang, Y. Wu, Y. Zhu, and Y. Chi, "Safety assessment of gender-specific human electromagnetic exposure with aortic valve stents for EV-WPT," *Applied Computational Electromagnetics Society (ACES) Journal*, vol. 39, no. 08, pp. 742–753, Aug. 2024.

[9] International Commission on Non-Ionizing Radiation Protection, "Guidelines for limiting exposure to electromagnetic fields (1 Hz to 100kHz)," *Health Phys.*, vol. 118, no. 5, pp. 818–836, 2020.

[10] International Commission on Non-Ionizing Radiation Protection, "ICNIRP Guidelines for Limiting Exposure to Time-Varying Electric, Magnetic and Electromagnetic Fields (100 kHz to 300 GHz)," *Health Phys.*, vol. 128, no. 2, pp. 190–202, 2024.

[11] W. H. Bailey, R. Bodemann, J. Bushberg, C. K. Chou, R. Cleveland, A. Faraone, K. R. Foster, K. E. Gettman, K. Graf, T. Harrington, A. Hirata, R. R. Kavet, J. Keshvari, B. J. Klauenberg, A. Legros, D. P. Maxson, J. M. Osepchuk, J. P. Reilly, R. R. A. Tell, A. Thansandote, K. Yamazaki, M. C. Ziskin, and P. M. Zollman, "Synopsis of IEEE Std C95.1™-2019 IEEE Standard for Safety

Levels With Respect to Human Exposure to Electric, Magnetic, and Electromagnetic Fields, 0 Hz to 300 GHz," *IEEE Access*, vol. 7, pp. 171346–171356, 2019.

[12] C. Lu, X. Huang, X. Liu, Y. Zeng, R. Liu, C. Rong, and M. Liu, "Design and optimization of the low-frequency metasurface shield for wireless power transfer system," *IEEE Trans. Transp. Electrif.*, vol. 8, no. 1, pp. 723–733, Mar. 2022.

[13] Q. Zhu, Y. Zhang, Y. Guo, C. Liao, L. Wang, and L. Wang, "Null-coupled electromagnetic field canceling coil for wireless power transfer system," *IEEE Trans. Transp. Electrif.*, vol. 3, no. 2, pp. 464–473, June 2017.

[14] Q. Zhu, Y. Guo, L. Wang, C. Liao, and F. Li, "Improving the misalignment tolerance of wireless charging system by optimizing the compensate capacitor," *IEEE Trans. Ind. Electron.*, vol. 62, no. 8, pp. 4832–4836, Aug. 2015.

[15] R. Qin, J. Li, J. Sun, and D. Costinett, "Shielding design for high-frequency wireless power transfer system for EV charging with self-resonant coils," *IEEE Trans. Power Electron.*, vol. 38, no. 6, pp. 7900–7909, June 2023.

[16] N. Fu, J. Deng, Z. Wang, and D. Chen, "Dual-phase-shift control strategy with switch-controlled capacitor for overall efficiency optimization in wireless power transfer system," *IEEE Trans. Veh. Technol.*, vol. 72, no. 6, pp. 7304–7317, June 2023.

[17] Z. Li, C. Zhu, J. Jiang, K. Song, and G. Wei, "A 3kW wireless power transfer system for sightseeing car supercapacitor charge," *IEEE Trans. Power Electron.*, vol. 32, no. 5, pp. 3301–3316, May 2017.

[18] D. E. Gaona, C. Jiang, and T. Long, "Highly efficient 11.1-kW wireless power transfer utilizing nanocrystalline ribbon cores," *IEEE Trans. Power Electron.*, vol. 36, no. 9, pp. 9955–9969, Sep. 2021.

[19] P. Lagouanelle, F. Freschi, L. Pichon, and L. Giaccone, "Fast and reliable human exposure assessment around high power systems using surrogate modeling," *IEEE Access*, vol. 12, pp. 34835–34845, 2024.

[20] Y. Wang, F. Wang, Y. Tian, A. Sun, and B. Liu, "Surrogate-assisted multiobjective optimization of double-D coil for inductive power transfer system with LCC-LCC compensation network," *IEEE Trans. Ind. Electron.*, vol. 71, no. 9, pp. 10612–10624, Sep. 2024.

[21] X. Li, J. Li, L. Zuo, L. Zhu, and H. T. Shen, "Domain adaptive remaining useful life prediction with Transformer," *IEEE Trans. Instrum. Meas.*, vol. 71, pp. 1–13, 2022.

[22] B. Zhang, H. Yuan, J. Ge, L. Cheng, X. Li, and C. Xiao, "Weak appearance aware pipeline leak detection based on CNN-Transformer hybrid architecture," *IEEE Trans. Instrum. Meas.*, vol. 74, pp. 1–9, 2025.

[23] A. Feng, X. Zhang, and X. Song, "Unrestricted attention may not be all you need masked attention mechanism focuses better on relevant parts in aspect-based sentiment analysis," *IEEE Access*, vol. 10, pp. 8518–8528, 2022.

[24] Y. Dash, S. C. Sarangi, V. Gupta, N. Kumar, and A. Abraham, "A novel context-aware feature pyramid networks with Kolmogorov-Arnold modeling and XAI framework for robust lung cancer detection," *IEEE Access*, vol. 13, pp. 108992–109008, 2025.

[25] K. Kalita, J. V. N. Ramesh, L. Cepova, S. B. Pandya, P. Jangir, and L. Abualigah, "Multi-objective exponential distribution optimizer (MOEDO): A novel math-inspired multi-objective algorithm for global optimization and real-world engineering design problems," *Sci. Rep.*, vol. 14, no. 1, p. 1816, 2024.

T. H. Wang received the B.S. degree in electrical engineering and the Ph.D. degree in vehicle engineering from Jilin University, Changchun, Jilin, China, in 2010 and 2016, respectively. From 2016 to 2019, he was a Post-Doctoral Researcher at the Department of Science and Technology of Instrument, Jilin University, where he is currently an Associate Professor with the College of Instrumentation and Electrical Engineering. His research interests include the uncertainty quantification of wireless power transfer of EVs and human electromagnetic exposure safety.

K. F. Zhao received the B.S. degree in electrical engineering and automation from the College of Instrumentation and Electrical Engineering, Jilin University, Changchun, Jilin, China, in 2023, where he is currently pursuing the M.S. degree in electrical engineering. His research interests include human electromagnetic safety protection and electromagnetic compatibility of EVs.

H. W. Duan received the B.S. degree in electrical engineering and automation from the College of Electrical Engineering, Northeast Electric Power University, Jilin, China, in 2024. He's currently working on his M.S. degree at Jilin University, Jilin. Since 2024, he has worked on the operation and the application of micro-grid systems.

G. Lv received the master's degree in electronic circuit and system from College of Electronic Science & Engineering, Jilin University, Changchun, Jilin, China, in 2008. He joined the National Automotive Quality Supervision & Inspection Center (Changchun) after graduation. He is currently head of the EMC department. He is in charge of EMC performance in vehicle approval under the direction of the Ministry of Industry and Information Technology (MIIT) and Certification and Accreditation Administration of the P.R.C. He focuses on test methods improving and National Standards edit and amendment in EMC domain. He has joined teams responsible for EMC part of "Test and evaluation of autonomous electric vehicle" subject which is released by Ministry of Science and Technology (MOST) and "Research on real-time concurrent simulation test technology of multi-source sensor information of intelligent networked vehicle" which is released by Science and Technology Department of Jilin Province.

Q. Y. Yu received the B.S. and the M.S. degrees from the College of Communication Engineering, Jilin University, Changchun, Jilin, China, in 2016 and 2020, respectively, where he is pursuing the Ph.D. degree. His research interests include uncertainty quantification and electromagnetic compatibility of EVs.

S. S. Guan received the B.S. degree in precision instruments and machinery and the Ph.D. degree in measurement technology and instruments from Jilin University, Changchun, Jilin, China, in 2008 and 2012, respectively. In 2019, she was a Visiting Scholar at the Southern University of Science and Technology, Shenzhen. She is currently an Associate Professor with the College of Instrumentation and Electrical Engineering, Jilin University. Her research interests include forward modeling and inverse algorithms of EM fields, and the development of electromagnetic instruments.

Large Angle Electronically Controlled Beam Scanning Antenna Based on Liquid Crystal

Wei Hu[1], Di Jiang[1], Jiahao Zhao[1], Chenqi Zhang[1], Guhaolan Zhao[1], Jiacheng Zhao[1], Bo Yan[1], Chuanpei Xu[2], and Guofu Wang[3]

[1]Information and Communication Engineering
University of Electronic Science and Technology of China, Chengdu 611731, China
weihu_2021@163.com, dijiang@uestc.edu.cn, zjh17732991106@163.com, chenqizhang_00@163.com, zghl_work@163.com, lyang_26@163.com, boyan@uestc.edu.cn

[2]Guilin University of Electronic Technology
Guilin, Guangxi 541004, China
Xuchuanpei@163.com

[3]Guangxi University of Science and Technology
Liuzhou, Guangxi 545006, China
guofwang@126.com

Abstract – In this paper we propose a miniaturized large-angle beam scanning phased array antenna using liquid crystal. We innovatively combine the liquid crystal electrically tunable structure with the wide-beam antenna element structure and design an integrated multi-layer antenna structure which realizes large-angle beam scanning within the working bandwidth. The problems of low beam control accuracy and narrow scanning angle of traditional array antenna are effectively addressed. The overall dimensions of the prototype are $74\times60\times4$ mm. Based on the test results of the prototype the gain has reached 20.2 dBi at 27 GHz and the scanning angle was greater than $\pm60^\circ$.

Index Terms – Large-angle beam scanning, liquid crystal, miniaturization, phased array antenna.

I. INTRODUCTION

In recent years, antennas in wireless communication systems are required to meet the requirements of many high performances, such as high gain pattern, wide-beam scanning angle and wide bandwidth. A phased array antenna has the functions of beam scanning, beam control, and anti-interference. As a representative of high-performance antenna, phased array antenna have been widely studied, and play an important role in vehicle radar, satellite radar, 5G mobile terminal and other fields. As a key device of phased array, the phase shifter makes the beam superposition in a specific direction by changing the feed phase of the radiation element to achieve the function of beam forming. The traditional phase shifter unit usually adopts PIN diode-based phase shifters [1–6], varactor diode-based phase shifters [7, 8], digital phase shifters [9, 10], ferrite-based phase shifters [11] and other methods [12–15] to achieve phase shift, among which PIN diode and varactor-diode based phase shifters have high insertion loss and can only achieve step phase shift. Although a digital phase shifter has higher phase shift accuracy, the cost and volume increase exponentially with the increase of phase shift accuracy, which is not conducive to large-scale array and miniaturization. As a tunable material, ferrite can realize continuous phase shift, but its high insertion loss limits its application in high frequency. Therefore, how to design a continuously tunable phase shifter and the associated matching antenna system is vital to develop a new generation of phased array antennas.

Liquid crystal, as a new passive tunable material, exhibits obvious polarity under electric field, so it has the ability to continuously tune permittivity under bias voltage. The thermal expansion coefficient of liquid crystals is usually between 10^{-5}/K and 10^{-6}/K. This numerical range indicates that the size change of liquid crystal materials is relatively small when the temperature changes. This dimensional stability makes liquid crystals an ideal material for manufacturing high-precision optical instruments and high-precision antennas. Liquid crystal molecules have an ordered arrangement structure, which makes liquid crystals exhibit anisotropy in physical properties. Compared to some lumped phase-shifting devices, liquid crystal devices have no parasitic effects in higher frequency bands and have smaller losses. This feature enables liquid crystal antennas to

Submitted On: July 04, 2024
Accepted On: July 24, 2025

https://doi.org/10.13052/2025.ACES.J.401106

maintain high efficiency and less energy loss when transmitting signals.

This study demonstrates a liquid crystal based phased array antenna with significant innovations in both architecture and performance. We propose a novel integrated structure combining a wide-beam dipole radiator array, a high-isolation feed network, liquid crystal-based phase shifting, and a dedicated liquid crystal bias control circuit achieving unprecedented miniaturization while overcoming traditional scan limitations. Experimental validation confirms breakthrough beam-scanning capabilities: continuous 1D scanning over 120° with a peak gain of 20.2 dBi.

II. STRUCTURE OF DESIGNED ANTENNA

A. Liquid crystal phased shifter design

In this paper we use a slow wave transmission line as the phase-shifting structure, which is suspended upside down under the first layer substrate, and whose lower surface is in contact with the liquid crystal. The second layer substrate adopts a slot design to contain the liquid crystal, and the third layer substrate is used to print the metal ground and form a bias electrode with the transmission line. By changing the paranoid voltage applied to the metal ground, the dielectric constant of the liquid crystal is controlled, then the transmission coefficient of the electromagnetic wave on the transmission line can be changed, and thus the phase shift can be controlled.

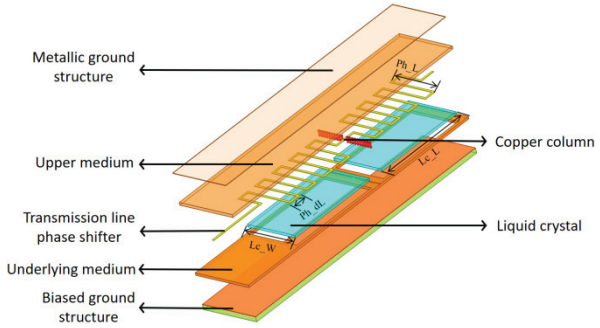

Fig. 1. Diagram of liquid crystal phase shifter.

To ensure that the primary working mode of electromagnetic waves passing through the phase shifter remains a quasi-TEM (Transverse Electromagnetic, where both electric and magnetic fields are transverse to the direction of wave propagation) wave and to maximize energy transfer to the output end, the liquid crystal tank is designed in two sections. A row of metal copper columns is placed in the middle, replacing the traditional metal electric wall, to optimize energy confinement within the transmission line. The diameter of the metal copper column is 0.2 mm and the spacing is 0.3 mm, which can effectively reduce return loss and transmission loss. The structure diagram of the designed phase shifter is shown in Fig. 1. The simulation results of the phase shifter base on liquid crystal material are shown in Fig. 2, from which we can see that the maximum phase shift is 410° by changing the dielectric constant of the liquid crystal and the insertion loss of the phase shifter is kept within 3 dB, in bandwidth of 26–28 GHz.

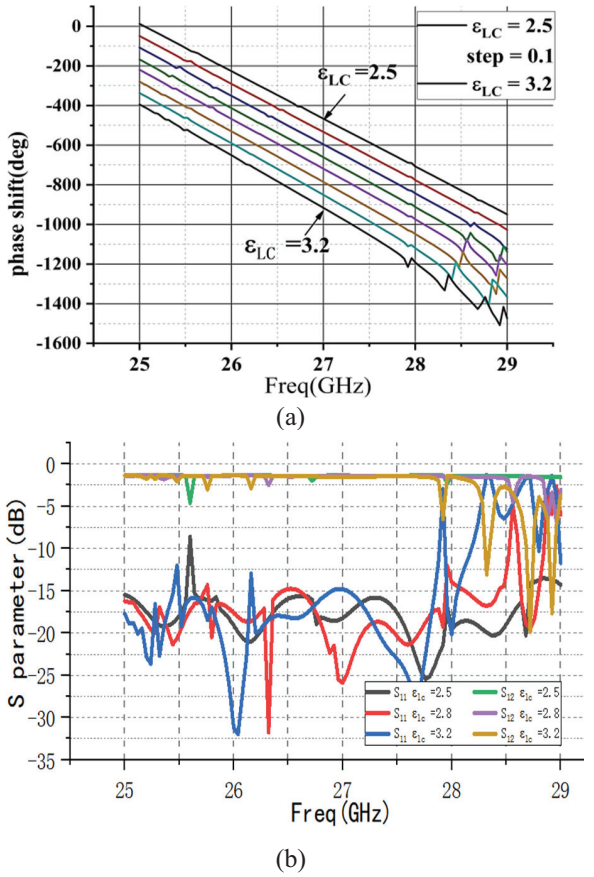

Fig. 2. Simulation results of the designed phase shifter: (a) relationship between phase and dielectric constant and (b) S parameter of the phase shifter.

B. Power division network design

To ensure the miniaturization of the power division phase-shifting network while further improving port isolation, we propose a novel network structure. In this design, the power dividers are distributed across different layers, effectively reducing coupling between the transmission lines.

As shown in Fig. 3 (a), a multistage combined Wilkinson power divider is used to realize the cascade of phase shifters after equal phase power divider. The structure of the power divider adopts a copper column to reduce electromagnetic interference and leakage

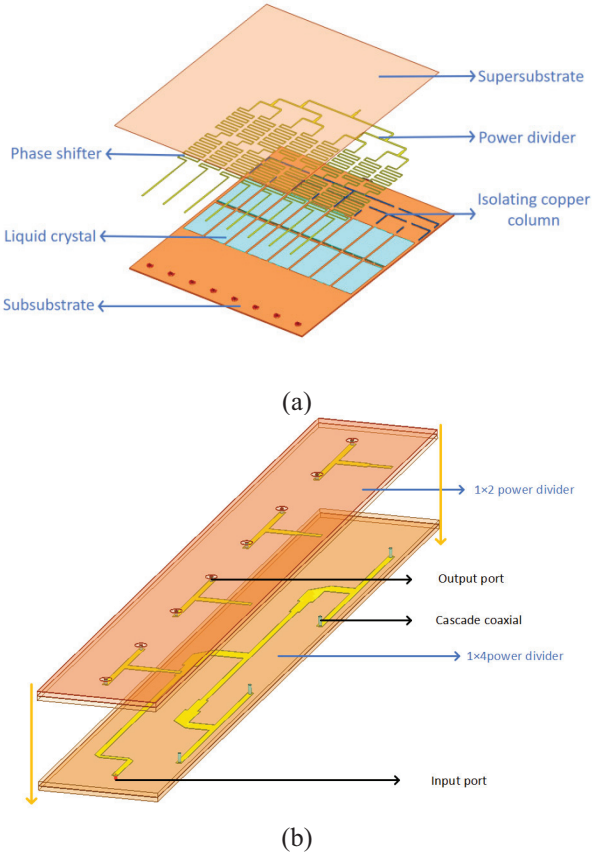

Fig. 3. Structure of designed power divide: (a) cascade of phase shifters and power divider and (b) structure of post-phase shifter power division network.

between adjacent lines and improve port isolation. The design of the post-phase shift power division network is shown in Fig. 3 (b). The multi-layer hierarchical power division structure is adopted to reduce the horizontal size to achieve miniaturization. The output end of the phase shifter is cascaded with the upper power divider through eight metallization holes to distribute the power of the post-phase shift signal.

C. Radiation patch design

In this work, we used a binary magnetoelectric dipole antenna to broaden the beam, as shown in Fig. 4. The traditional dipole antenna is divided into a driver patch and a parasitic patch, allowing for more flexible control of the current loop direction and enabling miniaturization of the patch. By increasing the diversity of the direction of the magnetic current, the structure can broaden the beam width by more abundant field distribution around the radiating element. The designed patch antenna demonstrates favorable performance, as shown in Fig. 5. It achieves excellent impedance matching at 27 GHz with a reflection coefficient of −18 dB and delivers a peak gain of approximately 5 dBi at the boresight direction, verifying its effective directional radiation characteristic.

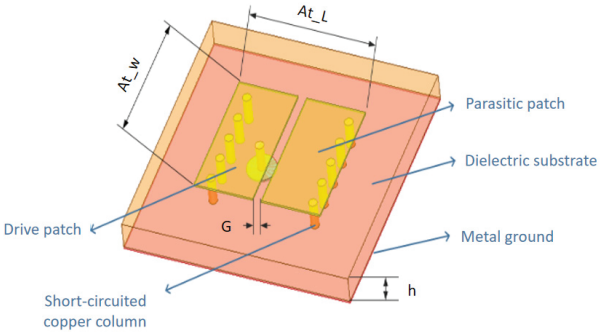

Fig. 4. Structure of designed radiation patch.

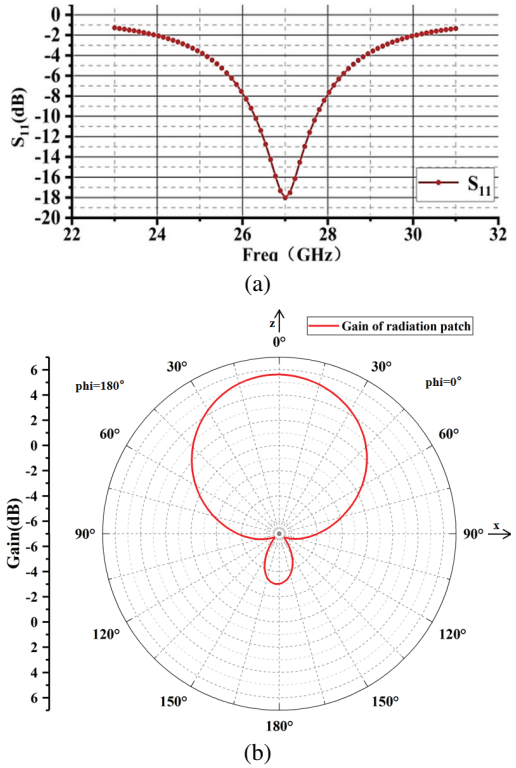

Fig. 5. Simulation result of designed antenna patch: (a) S parameter of antenna patch and (b) gain of antenna patch.

D. Array integration design

The phased array adopts an 8×8 uniform array model structure. A schematic diagram of the array structure is shown in Fig. 6. The array consists of antenna layer, power layer and phase shift power division network layer, and each layer is connected through metallized holes. In addition, in order to further reduce

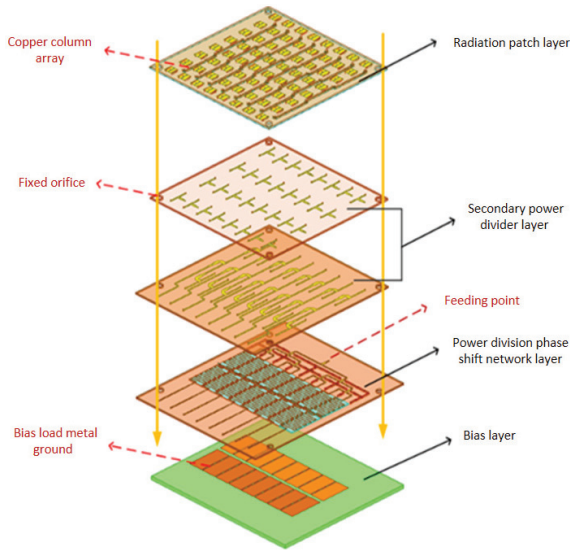

Fig. 6. Structure of array antenna multi-layer integration diagram.

the coupling between the antennas and improve the overall gain, the copper column structure is used as the electric wall between the units to inhibit electromagnetic leakage. By means of simulations, we found that optimal spacing between adjacent array elements is 5.55 mm, and optimal spacing of the decoupled copper columns is 0.3 mm.

Figure 7 shows that the maximum gain of the proposed array antenna is 21.8 dBi, the array realizes H-plane scanning by adjusting the dielectric constant of the liquid crystal to change the feed phase in the working band of each column antenna unit, and the maximum

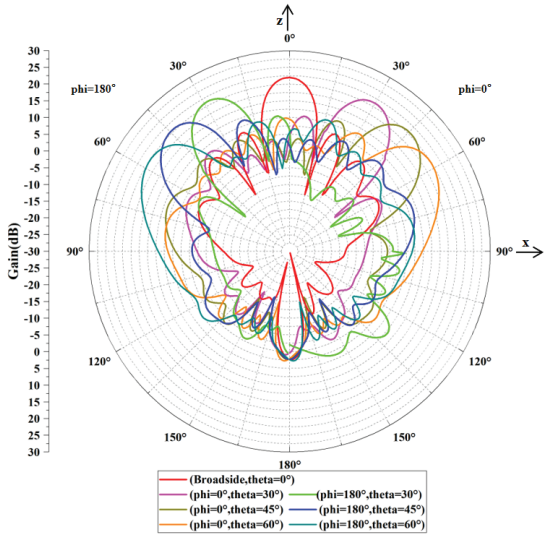

Fig. 7. Simulation results of radiation patterns under different dielectric constants at the operating frequency.

deflection angle can reach ±60°. Due to the structural design of phase shifter and power splitter, only the phase of each column is controlled, and the array can only realize one-dimensional beam scanning.

III. FABRICATION AND MEASUREMENT

Based on the previous design, the designed principle prototype and antenna test environment are shown in Fig. 8. The overall size of the prototype is 74×60×4

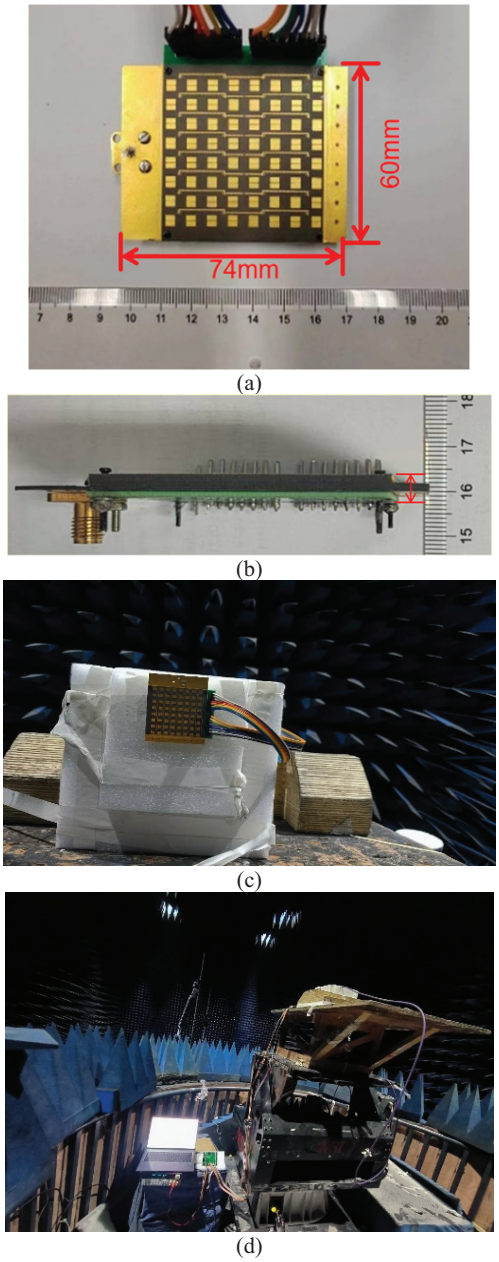

Fig. 8. Antenna array under measurement: (a) prototype of designed antenna, (b) profile structure of the prototype, (c) measurement in the anechoic chamber and (d) test environment and test equipment.

Table 1: Key parameters of the designed array antenna (mm)

Lc_W	Lc_L	Ph_L	Ph_dL	At_L	At_W	G	h
10.6	5.2	5.6	1.2	3.1	2.8	0.21	0.508

Table 2: Comparison with other phased array antenna

Ref.	Tuning Material	Element Number	Peak Gain (dBi)	Range	Size of Antenna (mm^3)	Operating Frequency (GHZ)	Bandwidth (%)
[1]	PIN	1×4	9.3	±58	35×65×1.524	2.85	26
[11]	LM	1×4	8.3	±38°	57.2×14×8	10	12
[2]	PIN	24×2	13.8	±60°	250×50×1.881	14.8	6.7
[8]	Varactor-diode	4×4	8.1	±25°	70×70×1.524	12	10
[9]	CMOS	1×4	17.6	±32°	–	16.5	16.4
[12]	LC	1×4	6.7	±23°	35×50×2.5	35	5.1
This Work	LC	8×8	20.2	±60°	74×60×4	27	7.4

mm, and a stepped laminated design is adopted to meet the requirements of wiring and perforation process. The array is independently tuned by eight columns of liquid crystal phase shifters. The phase shifters are filled with VMLC-2101 liquid crystal with a thickness of 0.254 mm. The relevant parameters are $\varepsilon_{r\perp} = 2.28$, $\varepsilon_{r\parallel} = 2.28$, $tan\delta_{r\perp} = 0.009$ and $tan\delta_{r\parallel} = 0.009$ at normal temperature.

The key dimensional parameters of the designed array antenna, corresponding to the labels in the structural diagrams, are summarized in Table 1. Different bias voltage groups are applied to the antenna, and the radiation signal of the standard antenna at the far field end is received and processed by using the antenna to be tested. Results of the far-field pattern parameters are obtained and saved, and the test results are shown in Fig. 9. The maximum gain of the antenna to be tested is 20.2 dBi. Attenuation is 1.23 dB at 30°, 2.64 dB at −30°, 4.48 dB at 60° and 4.63 dB at −60°. A comparison of phased arrays fabricated by different methods is shown in Table 2.

Compared with the simulations, the test results of the prototype are asymmetrical and the gain of the beams are degraded to a certain extent. There are four main reasons to explain the discrepancy between the simulations and the tests. First, the antenna array is designed with a non-strictly symmetric structure, and the scanning beam is not strictly symmetrical due to the influence of the boundary conditions of the antenna unit during the scanning of E-plane beam. The second reason is that the liquid crystal molecular direction is affected by the time of applying bias voltage and the initial state, so it is difficult to achieve quantitative unification, and there are bubbles in the perfusion process leading to errors in the change of dielectric constant. The third reason is that the liquid crystal layer is too thin, resulting in uneven liquid crystal contact. By thickening the liquid crystal layer and re-matching the impedance, this effect can be reduced. The fourth reason is that, due to the high-frequency band and small size, even slight deviations in the processed metal via holes and PCB lamination can cause impedance variations, leading to losses.

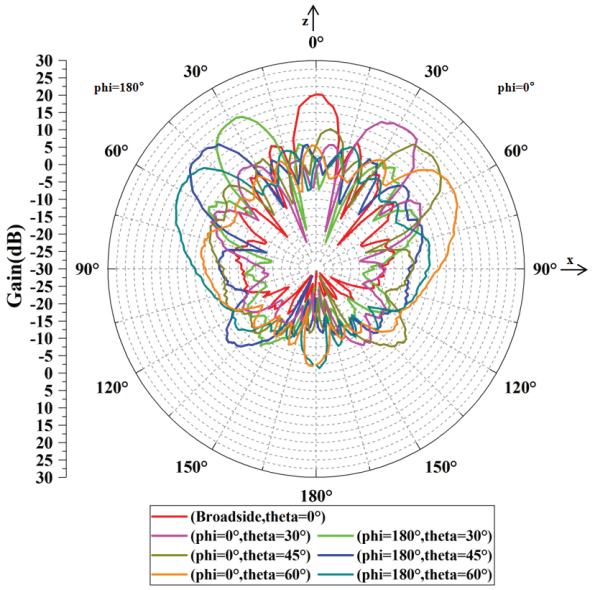

Fig. 9. Test results of radiation patterns under different dielectric constants at the operating frequency.

IV. CONCLUSION

In this paper, we present a design method for a large-angle beam scanning antenna based on liquid crystal. The antenna achieves single-frequency beam scanning. An innovative design structure of liquid crystal antenna is proposed to enable wide-angle beam control. The test results show that the antenna can achieve ±60° beam scanning at 27 GHz and gain is higher than

20 dBi, which verifies that the design of the antenna meets the requirements for large-angle beam scanning and supports the theory of liquid crystal reconfiguration.

ACKNOWLEDGMENT

This work was supported by the Sichuan Science and Technology Program (2023ZDZX0015); Science and Technology Projects of Chengdu (2023-JB00-00019-GX); Key Research and Development Program of Guangxi (AB25069115).

REFERENCES

[1] H. Xing, K. Zhang, M. Wang, C. Fan, H. Zheng, and E. Li, "Lower sidelobe phased array based on pattern reconfigurable elements," *International Journal of RF and Microwave Computer-Aided Engineering*, vol. 32, no. 7, p. e23171, 2022.

[2] X. Li, H. Q. Yang, R. W. Shao, F. Zhai, G. B. Liu, Z. X. Wang, H. F. Gao, G. Fan, J. W. Wu, Q. Cheng, and T.-J. Cui, "Low cost and high performance 5-bit programmable phased array antenna at Ku-band," *PIER*, vol. 175, pp. 29–43, 2022.

[3] S. Xu, K. Wu, Q. Zhou, S. Liao, and Q. Xue, "Low-profile conical beam array antenna based on concentric annular planar inverted-F antenna elements," *IEEE Antennas and Wireless Propagation Letters*, vol. 22, no. 7, pp. 1562–1566, July 2023.

[4] B. Xi, Y. Xiao, S. Tan, F. Yang, and Z. Chen, "2-Bit wideband electronically controlled reconfigurable phased array with wide-angle beam-scanning capacity," *IEEE Transactions on Antennas and Propagation*, vol. 71, no. 5, pp. 4128–4137, May 2023.

[5] H. Yu, P. Li, J. Su, Z. Li, S. Xu, and F. Yang, "Reconfigurable bidirectional beam-steering aperture with transmitarray, reflectarray, and transmit-reflect-array modes switching," *IEEE Transactions on Antennas and Propagation*, vol. 71, no. 1, pp. 581–595, Jan. 2023.

[6] X. Cao, C. Deng, Y. Yin, Y. Hao, and K. Sarabandi, "1-Bit reconfigurable transmit- and reflect-array antenna using patch-ground-patch structure," *IEEE Antennas and Wireless Propagation Letters*, vol. 23, no. 1, pp. 434–438, Jan. 2024.

[7] I. Syrytsin, S. Zhang, G. F. Pedersen, and A. S. Morris, "Compact quad-mode planar phased array with wideband for 5G mobile terminals," *IEEE Transactions on Antennas and Propagation*, vol. 66, no. 9, pp. 4648–4657, Sep. 2018.

[8] M. Nikfalazar, M. Sazegar, A. Mehmood, A. Wiens, A. Friederich, H. Maune, J. R. Binder, and R. Jakoby. "Two-dimensional beam-steering phased-array antenna with compact tunable phase shifter based on BST thick films," *IEEE Antennas and Wireless Propagation Letters*, vol. 16, pp. 585–588, 2017.

[9] Q. Zhang, C. Zhao, X. Zhang, Y. Wu, Y. Yu, and H. Liu, "A cost-effective Ku-band phased array in package integrating multi-independent CMOS transceivers with on-chip antennas," *IEEE Microwave and Wireless Technology Letters*, vol. 33, no. 10, pp. 1486–1489, Oct. 2023.

[10] H. Jeon and K. W. Kobayashi, "A high linearity +44.5-dBm IP3*C*-Band 6-Bit digital phase shifter using SOI technology for phased array applications," *IEEE Microwave and Wireless Components Letters*, vol. 29, no. 11, pp. 733–736, Nov. 2019.

[11] S. Alkaraki, Q.-W. Lin, J. R. Kelly, Z. Wang, and H. Wong, "Phased array antenna system enabled by liquid metal phase shifters," *IEEE Access*, vol. 11, pp. 96987–97000, 2023.

[12] X. Y. Li, D. Jiang, J. Liu, and M. S. Tong, "A Ka-band multilayer beaming-scanning antenna using liquid crystals," *IEEE Antennas and Wireless Propagation Letters*, vol. 21, no. 1, pp. 44–48, Jan. 2022.

[13] S. Ma, S.-Q. Zhang, L.-Q. Ma, F.-Y. Meng, D. Erni, L. Zhu, J.-H. Fu, and Q. Wu, "Compact planar array antenna with electrically beam steering from backfire to endfire based on liquid crystal," *IET Microwaves, Antennas & Propagation*, vol. 12, no. 7, pp. 1140–1146, 2018.

[14] O. H. Karabey, A. Gaebler, S. Strunck, and R. Jakoby, "A 2-D electronically steered phased-array antenna with 2×2 elements in LC display technology," *IEEE Transactions on Microwave Theory and Techniques*, vol. 60, no. 5, pp. 1297–1306, May 2012.

[15] O. H. Karabey, A. Mehmood, M. Ayluctarhan, H. Braun, M. Letz, and R. Jakoby, "Liquid crystal based phased array antenna with improved beam scanning capability," *Electronics Letters*, vol. 50, no. 6, pp. 426–428, 2014.

Wei Hu is a doctoral candidate of electronic information in Information and Communication Engineering, University of Electronic Science and Technology of China. He has a master's degree in communication and information system from Sichuan University. His main research direction is intelligent sensing and information system, microwave reconfigurable devices and systems, and broadband reconfigurable array antenna.

Di Jiang is Professor of Information and Communication Engineering, University of Electronic Science and Technology of China. He is mainly engaged in broadband reconfigurable microwave devices, array antennas, and liquid crystal array antennas.

Jiahao Zhao is a graduate student majoring in Electronic Information at the University of Electronic Science and Technology of China, with his main research directions focusing on RCS reduction metasurfaces and array antennas.

Chenqi Zhang is a graduate student of Information and Communication Engineering, from the University of Electronic Science and Technology of China. His main research direction is phased array antenna and holographic antenna.

Guhaolan Zhao is a graduate student majoring in Electronic Information at the University of Electronic Science and Technology of China. His research interests include reconfigurable antennas and antenna arrays.

Jiacheng Zhao is a graduate student majoring in Information and Communication Engineering at the University of Electronic Science and Technology of China. His research focuses on metasurfaces for RCS reduction.

Bo Yan is a professor of Information and Communication Engineering at the University of Electronic Science and Technology of China. Her current research interests lie in embedded system, FPGA/ASIC design, and AI for the Internet of Things (AIoT).

Chuanpei Xu received her Ph.D. degree from Xidian University, China, in 2006. She is currently a professor of Instrument Science and Technology at Guilin University of Electronic Science and Technology in Guangxi, China. Her current research focuses on integrated circuit testing, automatic test and control systems, microfluidics, and biosensors.

Guofu Wang was born in Pingdingshan, China, in 1977. He received the M.S. and Ph.D. degrees in signal and information processing from the Chinese Academy of Sciences in 2005 and 2007, respectively. Since 2017, he has been a Professor with the School of Electrical and Information Engineering, Guangxi University of Technology. His main research interests include adaptive signal processing and image processing. He has a rich research experience in the development of key technologies of photoelectric countermeasure turntables.

A Miniaturized Dual-Band Circularly Polarized Antenna With Broadband and Flexible Frequency Ratio

Yunlong Mao[1], Deshun Li[1], Yifan Shen[1], Atef Z. Elsherbeni[2], and Si Li[1]

[1]Ocean College
Jiangsu University of Science and Technology, Jiangsu 212003, China
maoyunlong0511@just.edu.cn, just_lds@163.com,
shenyifan@stu.just.edu.cn, lisi0511@just.edu.cn

[2]Electrical Engineering Department
Colorado School of Mines, Golden 80401, USA
aelsherb@mines.edu

Abstract – A dual-band circularly polarized antenna with AR (Axial Ratio) bandwidth enhanced using parasitic strips and triangle notches is proposed in this paper. The proposed antenna comes with a size of $53 \times 53 \times 3.813$ mm ($0.64\lambda_g \times 0.64\lambda_g \times 0.046\lambda_g$ at 2.45 GHz), which is composed of two layers of substrate and three layers of metallic patterns. With the introduction of parasitic strips on the top metallic layer and etched triangles on the ground plane, this antenna exhibits dual-band circularly polarized character. A flexible frequency ratio from 1.57 to 2.01 could be obtained by changing the size of the triangle notches. Simulations and measurements verified that the proposed antenna shows relative S11<-10 dB bandwidth of 36.6% (2.23–3.25 GHz) and 51.3% (3.58–6.05 GHz), relative AR<3 dB bandwidth of 17.6% (2.32–2.77 GHz) and 11.1% (4.65–5.30 GHz), peak gains of 4.45 dBic and 6.24 dBic, respectively. This antenna is a good candidate for the 2.45 GHz communication band and the 5G sub-6 NR band applications.

Index Terms – Circular polarization, dual-band, microstrip antenna, parasitic patch, ultra-wideband.

I. INTRODUCTION

The rapid development of 5G networks has brought many opportunities, driving the advent of new applications in areas such as the Internet of Things (IoT) [1]. Given the proliferation of diverse communication standards, contemporary wireless devices require multiband antenna operation to ensure functional compatibility. Consequently, antennas must support multiple frequency bands while maintaining a low-profile, planar form factor to facilitate seamless integration into compact and geometrically constrained platforms.

There are various approaches proposed in the realm of dual-band circularly polarized antenna design. One such approach integrates two radiating structures on a substrate, each with distinct operating frequencies. This configuration can be utilized for array antenna [2–4], stack of patches [5–8], or a combination of electric and magnetic dipoles [9, 10]. The second approach uses the integration of dual-band antennas with polarization-converting surfaces, such as the polarization rotation AMC (Artificial Magnetic Conductor) [11] and the dual-linear-to-circular polarization converters [12]. These designs in general necessitate the use of additional substrates to facilitate specific polarization transitions or rotating structures, which also result in high-profile and structural complexity. To deal with these limitations, researchers are focusing on the study of the incorporation of slots into the radiating patch [13, 14]. This method renders the antenna structure uncomplicated, while maintaining the antenna's dimensions, and enables the antenna's operational frequency band to be flexibly adjustable. However, a common issue is that the circularly polarized bandwidth is relatively narrow. A thorough analysis of circular polarization reveals that the primary factor contributing to the constricted circularly polarized bandwidth is the substantial Q value [14, 15] introduced by the narrow slots. Several approaches were employed to obtain reduced Q value, such as widening the width of slots [14, 16, 17] and employing parasitic patches [15, 16, 18, 19]. However, from the aspect of equivalent circuits, either of these methods could widen the AR (Axial Ratio) bandwidth at one frequency but may not be applicable for two or more bands. Therefore, it is still a challenge to obtain wide AR bandwidth at multiple bands.

In this paper, we propose a low-profile miniaturized dual-band circularly polarized antenna with wideband AR in both operational bands. At the lower frequency band, the AR bandwidth is widened using parasitic strips, while at the higher frequency band, the AR

Submitted On: August 12, 2025
Accepted On: November 03, 2025

https://doi.org/10.13052/2025.ACES.J.401107

bandwidth is widened by triangle notches etched on the ground plane. As a consequence, both AR bands are individually adjustable. Moreover, the proposed antenna achieved FFR (Flexible Frequency Ratio) from 1.57 to 2.01 by changing the size of the notched triangles. Simulations and measurements were operated, and comparisons to some recent researchers identified the advancement of the proposed antenna.

II. ANTENNA DESIGN AND PARAMETRIC STUDIES

A. Antenna element configuration

The geometry of the designed dual-band circularly polarized antenna is shown in Fig. 1. It is composed of two layers of substrates with plane size of 53×53 mm^2. The first substrate height is 3 mm and its relative permittivity is $\varepsilon r = 2.2$. The radiation patch is printed on the top side of the substrate, and the ground plane is on the other side. The second substrate height is 0.813 mm with $\varepsilon r = 4.4$. An L-shaped feedline is printed on its bottom side. Detailed geometrical parameters are listed in Table 1.

Table 1: Parameters of the proposed antenna (unit: mm)

D	*L*	*W*	*l1*	*l2*	*l3*	*l4*
53	10	2	14	7	8	28
l5	*w1*	*w2*	*w3*	*w4*	*w5*	*lb*
15	4.5	5.5	1.5	6	7.5	32
ls	*h1*	*h2*	*g1*	*g2*	*a*	*b*
28	3	0.813	0.3	0.4	12	4

B. Design procedure

To generate circularly polarized waves, it is essential to produce two orthogonal currents with 90 degrees phase difference. Therefore, we first designed an octagonal patch as displayed in Fig. 2 (a), and the ground plane is as displayed in Fig. 2 (d). This patch is fed by an L-shaped microstrip. Such a structure exhibits the potential of generating circularly polarized waves, but the bandwidth is limited.

The frequency resonance condition can be expressed as [20]

$$f_0 = \frac{1}{2\pi\sqrt{LC}}. \tag{1}$$

Therefore, resonance frequency modulation can be achieved by introducing additional capacitive or inductive components into the circuit system. The inductance value is predominantly governed by the thickness of the substrate (h) in planar circuit implementations. Concurrently, the equivalent capacitance (C_{eq}) exhibits dual dependency on both the geometric configuration of patch elements and the inter-element gap (g). Therefore, in this paper, the addition of parasitic strips near the center patches results in the formation of a capacitance at the gap between the center patch and the parasitic strips, due to the accumulation of moving electrons. Consequently, edge capacitors C_1, C_2, and C_3 were introduced at the gap to facilitate the desired electrical effects. Additionally, the center patches and ground plane inherently exhibit

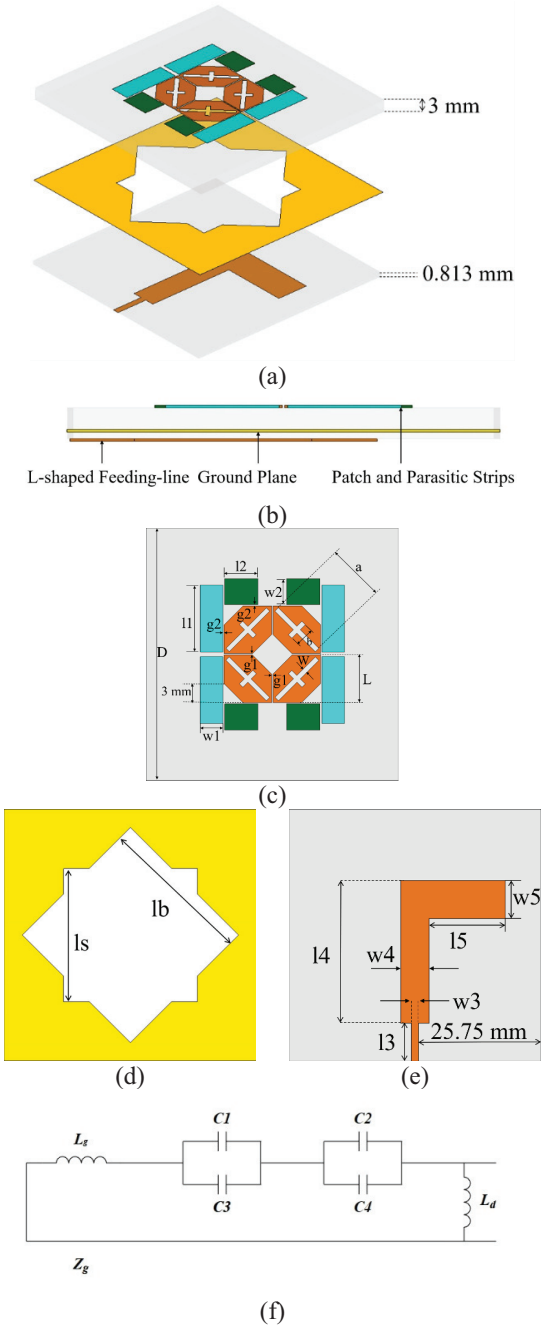

Fig. 1. Antenna structure. (a) 3D view, (b) side view, (c) top view, (d) ground plane, (e) bottom view, (f) equivalent circuit.

inductive characteristics. Therefore, the resonant frequency can be expressed as [21–25]

$$f_0 = \frac{1}{2\pi\sqrt{(L_g + L_d)(C_1 + C_2 + C_3 + C_4)}} = \frac{1}{2\pi\sqrt{(L_g + L_d)C_{total}}}, \quad (2)$$

in equation (2), C, L_d, and L_g can be approximated as follows:

$$C_1 = C_3 = \frac{L\varepsilon_0\sqrt{(\varepsilon_r + 1)}}{\sqrt{2}\pi}\cosh^{-1}\left(\frac{L + W_1 + 2g_2}{2g_2}\right), \quad (3)$$

$$C_2 = C_4 = \frac{L\varepsilon_0(\varepsilon_r + 1)}{\pi}\cosh^{-1}\left(\frac{L + W_2 + 2g_2}{2g_2}\right), \quad (4)$$

$$L_d = \mu h, \quad (5)$$

$$Lg = \frac{2Z_0}{\omega}\tan\left(\frac{\omega\sqrt{\mu_0\varepsilon_0(\varepsilon_r + 1)}(L - 2W)}{2\sqrt{2}}\right). \quad (6)$$

Thus, it can be observed that, with the center patches dimensions and gap g_2 being fixed, the dimensions of the parasitic strips constitute the critical factor affecting the total capacitance. Therefore, adjusting the dimensions of two distinct parasitic strip sets enables modulation of the total capacitance (C_{total}), thereby influencing the antenna's resonant frequency.

In this study, we compared the case with and without parasitic strips, Ant. 1 and Ant. 2. It is shown that the introduction of parasitic strips improved the impedance matching at higher frequencies while successfully achieving a wideband circular polarization at frequencies around 2.5 GHz. The introduction of parasitic strips modifies the current distribution, resulting in y-direction and x-direction currents exhibiting equal amplitude with a 90° phase difference in the low-frequency band, thus achieving circular polarization at lower frequencies. However, the circular polarization at around 4.6 GHz is almost vanished.

To introduce circular polarization bandwidth in the high-frequency band, observation of surface current vectors on the ground plane at 5 GHz revealed a current mismatch condition at the etched edges. Consequently, a set of triangular notches were etched around the original square slot, with the final configuration shown in Fig. 1 (d). Comparing Ant. 2 and the proposed one, it is observed that the introduction of the triangle notches enhanced circularly polarization at higher frequencies while maintaining a similar operating band as Ant. 2. Circular polarization is also observed from 4.4∼5.22 GHz. Such an effect is a result of the strategy that extended the current path as illustrated in Fig. 3, making it close to the half wavelength at 5 GHz.

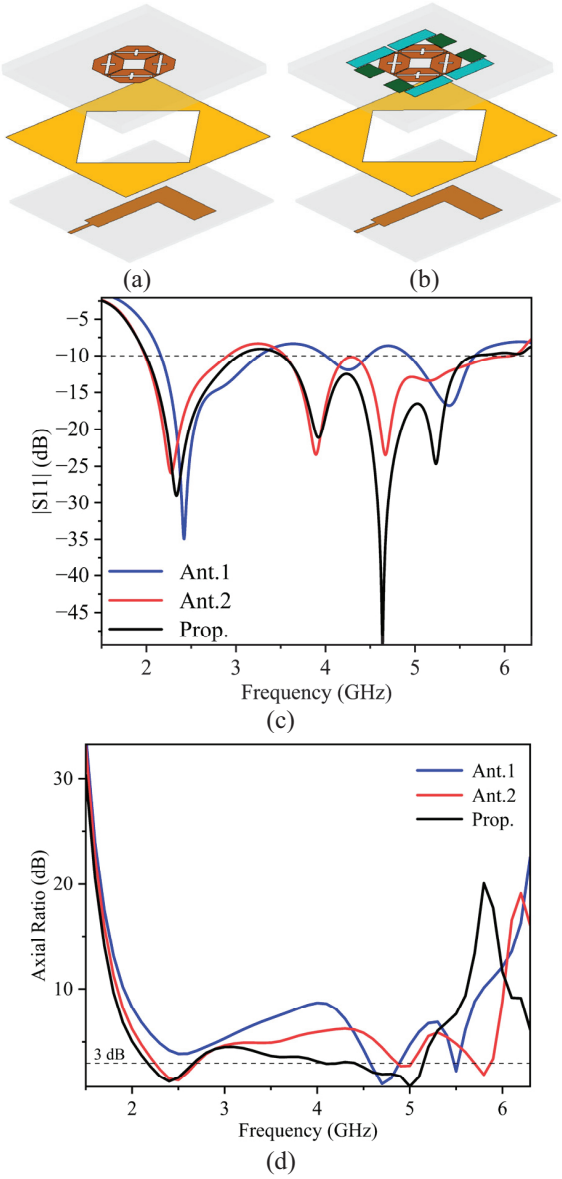

Fig. 2. (a) Structure of Ant. 1, (b) structure of Ant. 2, (c) simulated S parameters S11, (d) simulated axial ratio AR of Ant. 1, Ant. 2, and proposed antenna.

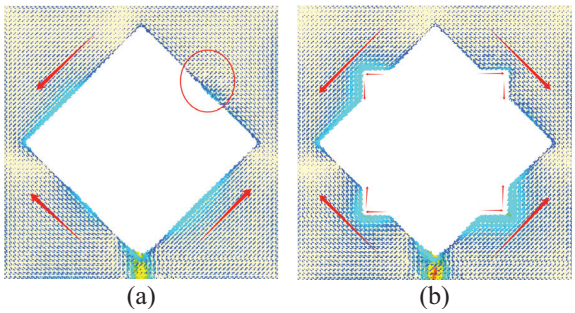

Fig. 3. Current path at 5 GHz. (a) Ant. 2 and (b) proposed antenna.

C. Parametric analysis

To further validate the effects of parasitic strip integration and slot etching on antenna performance, we analyzed their parameters separately using CST Studio Suite. The impacts of parasitic strips and etched notches on antenna S11 and AR are demonstrated in Figs. 4 and 5. As observed in Fig. 4, the two distinct parasitic strip sets with differentiated dimensions induce frequency band-specific modifications, enabling independent regulation of impedance matching across distinct frequency bands.

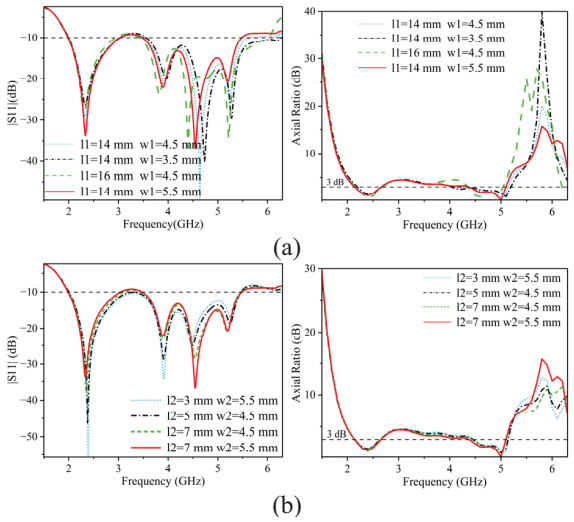

Fig. 4. S11 and AR versus frequency for (a) l1 and w1 and (b) l2 and w2.

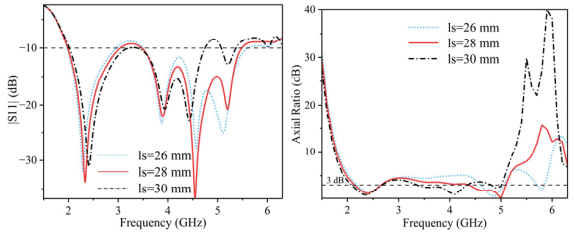

Fig. 5. S11 and AR versus frequency for different values of ls.

As shown in Fig. 5, significant modifications in S11 and AR are observed. With the increase of ls, the operational bandwidth at lower frequencies exhibits minor expansion, while the upper cutoff frequency at higher frequencies demonstrates a pronounced downward shift. Figure 5 (b) reveals that the first AR frequency range remains nearly unchanged, whereas the second AR frequency range shifts substantially from 4.65–5.20 GHz to 3.34–4.37 GHz, with its corresponding minimum AR value shifting from 5 GHz to 4.13 GHz. This phenomenon occurs because ls directly governs the resonant frequency. As ls increases, the frequency ratio decreases from 2.01 to 1.57, elongating the current propagation path and thereby exciting resonance at lower frequencies.

The effects that the parasitic strips and the notches have on S11 and AR are plotted in Figs. 4 and 5. In Fig. 4, the increase of the parasitic strips size barely affects S11 and AR at lower frequencies but would cause a little shift at higher frequency. That is because the impedance at the operating frequencies is changing smoothly, hence slight changes of the parasitic strips would cause little difference on the antenna input impedance.

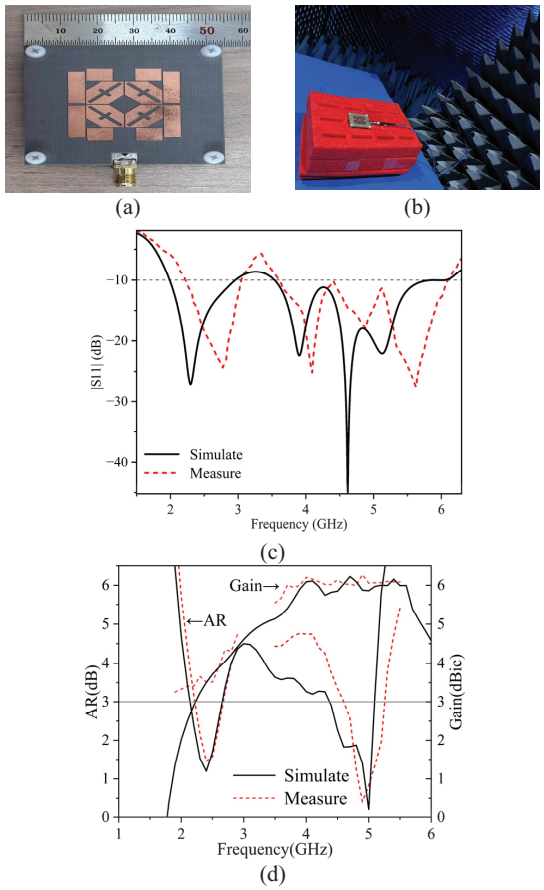

Fig. 6. (a), (b) Photo of antenna prototype. Simulation and measurement results of (c) S11 and (d) AR and gain.

In Fig. 5, significant changes are observed for both S11 and AR. In Fig. 5, with the increase of ls, the working frequency band at lower frequencies is only slightly extended, while at higher frequencies, the upper cut-off frequency is greatly shifted to a lower frequency. As reflected in Fig. 5 (b), the first AR frequency range is barely changed, while the second AR frequency range exhibits significant shift, from 4.65∼5.20 GHz

Table 2: Comparison with other dual-band circularly polarized antennas

Ref.	f_1/f_2 (GHz)	FBW_L/FBW_H	$ARBW_L/ARBW_H$	$Gain_L/Gain_H$ (dBic)	Antenna Size (λ_g^3 at f_1)
[13]	2.35/4.15	18.2%/17.8%	72.1%/63.5%	7.87/5.71	0.94*0.82*0.22
[14]	2.49/3.44	35.48%/25%	7.1%/5.06%	3.36/3.16	1.47*1.47*0.01
[26]	3.48/5.03	30.48%/18.51%	8.06%/6.38%	6.9/7.3	1.33*1.33*0.34
[27]	2.91/5.41	18.56%/10.45%	37.03%/33.9%	4.79/4.27	1.79*1.79*0.02
[28]	5.77/9.3	4.5%/2.7%	23.07%/28%	8.4/6.35	1.28*1.28*0.07
This Work	**2.74/4.64**	**36.6%/51.3%**	**53.19%/21.56%**	**4.45/6.24**	**0.64*0.64*0.04**

λ_g: actual wavelength of the center frequency of the low-frequency range,ARBW: relative bandwidth of circular polarization within the passband [13].

to 3.34∼4.37 GHz, of which the corresponding minimum AR value shifted from 5 GHz to 4.13 GHz. As a consequence, the frequency ratio is changed from 2.01 to 1.57. That is because ls affects the resonant frequency. With the increasement of ls, the current flow path would be extended, hence excited resonances at lower frequencies.

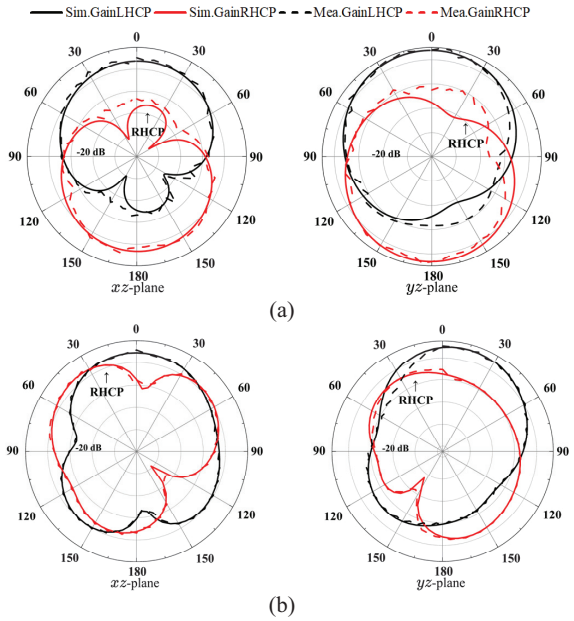

Fig. 7. Simulated and measured normalized radiation patterns of the proposed antenna at (a) 2.45 GHz on *xz*-plane and *yz*-plane and (b) 5.0 GHz on *xz*-plane and *yz*-plane.

III. ANTENNA MEASUREMENT

The proposed antenna was fabricated as shown in Fig. 6 (a) and measured using Keysight N5227A network analyzer and Satimo system. Figures 6 (b)–(c) shows that the measured and simulated results are well matched. Due to fabrication and measuring errors, a slight frequency shift was observed, but still within the required frequency range. The proposed antenna achieves a measured S11<-10 dB bandwidth of 36.6% (2.23–3.25 GHz) and 51.3% (3.58–6.05 GHz), AR<3 dB bandwidth of 17.6% (2.32–2.77 GHz) and 11.1% (4.65–5.20 GHz), and peak gains of 4.45 dBic and 6.24 dBic, respectively. Figures 7 (a)–(b) show the simulated and measured normalized radiation patterns in the *xz*- and *yz*-planes of the two frequency bands·

Comparisons between the proposed antenna and recent reported ones are listed in Table 2. As observed, the proposed antenna has achieved widest relative bandwidth for both impedance frequency bands and AR bandwidth, while obtaining high gain and small size. Therefore, it is a better candidate for wireless applications.

IV. CONCLUSION

This paper proposes a low-profile dual-band circularly polarized antenna for use in the 2.45 GHz communication band and the 5G sub-6 NR band (3.5–5.7 GHz). The proposed antenna employs a stacked and microstrip line-fed structure to produce ultra-wide operating bandwidths as well as circularly polarized radiation responses in the low- and high-frequency bands, respectively. The introduction of a star-slot structure at the ground plane not only affects the coupling efficiency but also affects the operating bandwidth and circularly polarized bandwidth. Test results show that the antenna has wide operating bandwidth and circularly polarized bandwidth. Comparing with existing methods, the antenna does not require the use of two antenna radiators or additional polarization conversion or rotating substrate, which provides a new approach for the design of dual-band antennas. These features make the proposed antenna attractive in duplex communication systems.

REFERENCES

[1] G. A. Akpakwu, B. J. Silva, G. P. Hancke, and A. M. Abu-Mahfouz, "A survey on 5G networks for the Internet of Things: Communication technologies and challenges," *IEEE Access*, vol. 6, pp. 3619–3647, 2017.

[2] C. D. Bui, N. Nguyen-Trong, and T. K. Nguyen, "A planar dual-band and dual-sense circularly polarized microstrip patch leaky-wave antenna," *IEEE Antennas and Wireless Propagation Letters*, vol. 19, no. 12, pp. 2162–2166, Dec. 2020.

[3] N. Nguyen-Trong, S. J. Chen, and C. Fumeaux, "High-gain dual-band dual-sense circularly polarized spiral series-fed patch antenna," *IEEE Open Journal of Antennas and Propagation*, vol. 3, pp. 343–352, 2022.

[4] J.-N. Wang, Z.-J. Guo, and Z.-C. Hao, "A millimeter-wave planar dual-band array antenna having individually LHCP and RHCP radiation characteristics," *IEEE Open Journal of Antennas and Propagation*, vol. 3, pp. 768–773, 2022.

[5] N. Yan, K. Ma, H. Zhang, and P. Jia, "An SISL triple-band multimode stacked-patch antenna with L-strips for multiband applications," *IEEE Transactions on Antennas and Propagation*, vol. 67, no. 2, pp. 1284–1288, Feb. 2019.

[6] Y. Liu, Z. Yue, Y. Jia, Y. Xu, and Q. Xue, "Dual-band dual-circularly polarized antenna array with printed ridge gap waveguide," *IEEE Transactions on Antennas and Propagation*, vol. 69, no. 8, pp. 5118–5123, Aug. 2021.

[7] N. Claus, "High-performance air-filled multiband antenna for seamless integration into smart surfaces," *IEEE Antennas and Wireless Propagation Letters*, vol. 20, pp. 2260–2264, 2021.

[8] K. Xue, "A dual-polarized filtering base-station antenna with compact size for 5G applications," *IEEE Antennas and Wireless Propagation Letters*, vol. 19, pp. 1316–1320, 2020.

[9] C. D. Bui, N. Nguyen-Trong, and T. K. Nguyen, "A planar dual-band and dual-sense circularly polarized microstrip patch leaky-wave antenna," *IEEE Antennas and Wireless Propagation Letters*, vol. 19, no. 12, pp. 2162–2166, Dec. 2020.

[10] P. Liu, F. Jia, Y. Zhang, G. Su, Q. Wang, and X. Y. Zhang, "Dual-polarized dipole antenna with dual-band spatial filtering response for aperture-shared triband base station array application," *IEEE Antennas and Wireless Propagation Letters*, vol. 22, no. 12, pp. 3057–3061, Dec. 2023.

[11] J. Zhu, Y. Yang, S. Li, S. Liao, and Q. Xue, "Dual-band dual circularly polarized antenna array using FSS-integrated polarization rotation AMC ground for vehicle satellite communications," *IEEE Transactions on Vehicular Technology*, vol. 68, no. 11, pp. 10742–10751, Nov. 2019.

[12] M. A. Sofi, K. Saurav, and S. K. Koul, "Four-port orthogonal circularly polarized dual-band MIMO antenna with polarization and spatial diversity using a dual-band linear-to-circular polarization converter," *IEEE Transactions on Antennas and Propagation*, vol. 70, no. 9, pp. 8554–8559, Sep. 2022.

[13] N. An and Y. Zhang, "Dual-band dual-sense circularly polarized antenna utilizing a radiating slot antenna as feeding structure," *IEEE Antennas and Wireless Propagation Letters*, vol. 23, no. 4, pp. 1321–1325, Apr. 2024.

[14] Q.-S. Wu, Z.-K. Lin, Z.-X. Du, and X. Zhang, "A dual-band dual-sense circularly polarized slot antenna with cascaded nonradiative resonator," *IEEE Antennas and Wireless Propagation Letters*, vol. 23, no. 10, pp. 3123–3127, Oct. 2024.

[15] Y. Mao, M. Zhu, H. Liu, S. Li, and S. Zhang, "A novel metasurface antenna with enhanced CP bandwidth through decreasing Q factor," *Microw. Opt. Technol. Lett.*, vol. 66, p. e34159, 2024.

[16] N. An and Y. Zhang, "Dual-band dual-sense circularly polarized antenna utilizing a radiating slot antenna as feeding structure," *IEEE Antennas and Wireless Propagation Letters*, vol. 23, no. 4, pp. 1321–1325, Apr. 2024.

[17] E. Demircioglu, M. H. Sazlı, S. T. İmeci, and O. Sengul, "Soft computing techniques on multi-resonant antenna synthesis and analysis," *Microwave and Optical Technology Letters*, vol. 55, no. 11, pp. 2643–2648, Nov. 2013.

[18] B. Tutuncu, H. Torpi, and S. T. Imeci, "Directivity improvement of microstrip antenna by inverse refraction metamaterial," *Journal of Engineering Research*, vol. 7, no. 4, pp. 151–164, Dec. 2019.

[19] M. Y. Imeci, B. Tütüncü, and S. T. Imeci, "A 3-dB 90° microstrip hybrid directional coupler at 2.27 GHz," *AEU-International Journal of Electronics and Communications*, vol. 155, Mar. 2023.

[20] B. Zheng, N. Li, X. Li, X. Rao, and Y. Shan, "Miniaturized wideband CP antenna using hybrid embedded metasurface structure," *IEEE Access*, vol. 10, pp. 120056–120062, 2022.

[21] D. Sievenpiper, Z. Lijun Zhang, R. F. J. Broas, N. G. Alexopolous, and E. Yablonovitch, "High-impedance electromagnetic surfaces with a forbidden frequency band," *IEEE Transactions on Microwave Theory and Techniques*, vol. 47, pp. 2059–2074, 1999.

[22] D. Chen, W. Yang, Q. Xue, and W. Che, "Miniaturized wideband planar antenna using interembedded metasurface structure," *IEEE Transactions on Antennas and Propagation*, vol. 69, no. 5, pp. 3021–3026, 2021.

[23] Z. Xia, X. Xiong, W. Xia, X. Cao, J. Hu, and R. Cheng, "Miniaturized wideband single-layer CP metasurface antenna using CPW-fed," *Microw. Opt. Technol. Lett.*, vol. 67, 2025.

[24] R. Mittra, T. Marinovic, O. Ozgun, S. Liu, and R. K. Arya, "Novel strategies for efficient computational electromagnetic (CEM) simulation of microstrip circuits, antennas, arrays, and metamaterials. Part-II: Characteristic basis function method, perfectly matched layer, GPU acceleration," *Applied Computational Electromagnetics*

Society (ACES) Journal, vol. 40, no. 6, pp. 471–498, June 2025.

[25] Y. Fan, L. Li, R. K. Arya, X. Ma, S. Kong, and J. Dong, "Outdoor Wi-Fi dual-band dual-polarized base station antenna design," *Applied Computational Electromagnetics Society (ACES) Journal*, vol. 39, no. 12, pp. 1042–1050, Dec. 2024.

[26] C.-W. Tong, H. Tang, W. Qin, W.-W. Yang, X.-F. Zhang, and J.-X. Chen, "Differentially inserted-fed compact dual-band circularly polarized dielectric resonator antenna," *IEEE Antennas and Wireless Propagation Letters*, vol. 18, no. 12, pp. 2498–2502, Dec. 2019.

[27] Y. Xu, L. Zhu, and N.-W. Liu, "Design approach for a dual-band circularly polarized slot antenna with flexible frequency ratio and similar in-band gain," *IEEE Antennas and Wireless Propagation Letters*, vol. 21, no. 5, pp. 1037–1041, May 2022.

[28] S. Ji, Y. Dong, S. Wen, and Y. Fan, "C/X dual-band circularly polarized shared-aperture antenna," *IEEE Antennas and Wireless Propagation Letters*, vol. 20, no. 12, pp. 2334–2338, Dec. 2021.

Yunlong Mao was born in Taizhou, Jiangsu, China, in 1989. He received the B.S. degree in electrical information engineering from the Jiangsu University of Science and Technology, Zhenjiang, in 2011, and the Ph.D. degree in information and communication engineering from Harbin Engineering University, Harbin, in 2018. He is currently an Assistant Professor with the School of Oceanology, Jiangsu University of Science and Technology. His research interests include antennas and finite difference time domain method.

Deshun Li was born in Yinchuan, Ningxia, China, in 2001. He received the B.S. degree in Ocean College from the Jiangsu University of Science and Technology. Zhenjiang, in 2023. He is currently a graduate student at Ocean College, Jiangsu University of Science and Technology. His research focuses on the microstrip antenna.

Yifan Shen was born in Wuxi, Jiangsu Province, China, in 2000. She received her B.S. degree in electronic information science and technology from Ocean College, Jiangsu University of Science and Technology in 2019. She is currently a graduate student at Ocean College, Jiangsu University of Science and Technology. Her research focuses on the cross-application of microwave technology, especially microwave hyperthermia treatment, including antenna design and optimization, phased array systems, and adaptive beamforming algorithms.

Atef Z. Elsherbeni is a renowned expert in electromagnetism, currently a professor at the Colorado School of Mines, and an IEEE Fellow and ACES Fellow. He received his Ph.D. in electrical engineering from the University of Manitoba in 1987 and subsequently taught at the University of Mississippi, where he held several academic and administrative positions. Elsherbeni's research has focused on computational electromagnetics, particularly in the application of finite-difference time-domain (FDTD) and finite-element methods (FEM). He has published a large number of academic papers and has given keynote speeches at several international conferences to share his research results and experience.

Si Li was born in Harbin, Heilongjiang, China, in 1987. She received the B.S. degree in electrical information engineering from the Jiangsu University of Science and Technology, Zhenjiang, in 2011, and the Ph.D. degree in information and communication engineering from Harbin Engineering University, Harbin, in 2018. She is now an Assistant Professor with the School of Oceanology, Jiangsu University of Science and Technology. Her research interests include metamaterials and antenna designs.

An Analytical Method for Shielding Effectiveness of Complex Metallic Cavities Based on the BLT Equation

Ai-Guo Gao, Da-Zhao Yu, Yi-Jiang Du, and He-Xiang Huang

School of Basic Sciences for Aviation
Naval Aviation University, Yantai, Shandong 264001, China
gaoaiguo2024@163.com, ytyudazhao@qq.com, 478342934@qq.com, 1052267738@qq.com

Abstract – A hybrid analytical method integrating the equivalent circuit method, electromagnetic topology theory, and the generalized BLT (Baum-Liu-Tesche) equation is proposed. This method systematically incorporates plane-wave incidence-angle effects and lossy conducting material properties and is further extended to heterogeneous configurations such as stepped cavities and series-parallel hybrid cascaded three-layer cavities, thus enabling rapid yet accurate assessment of both the shielding effectiveness (SE) and resonant behavior in complex metallic cavities. First, a model based on equivalent circuit theory is established. Next, a corresponding signal flow graph is established using electromagnetic topology theory, after which the generalized BLT equation is derived to compute the SE. Comparisons with CST full-wave simulation results demonstrate that the proposed method achieves a significant improvement in computational efficiency while maintaining high accuracy. It effectively accommodates arbitrarily eccentric apertures, aperture arrays, and arbitrary observation points, and can rapidly and accurately predict the SE and higher-order resonant frequencies, even at elevated frequencies. This work provides a simple and efficient analytical method for analyzing the SE of various heterogeneous and complex metallic cavities.

Index Terms – Electromagnetic topology (EMT) theory, equivalent circuit method, general Baum-Liu-Tesche (BLT) equation, shielding effectiveness (SE).

I. INTRODUCTION

As aviation equipment advances rapidly, the number and variety of airborne electronic devices are increasing at an accelerating pace. These electronic devices generate significant unintended electromagnetic emissions during operation, giving rise to a series of self-interference and mutual interference problems. Furthermore, against the backdrop of the evolving modern warfare, various directed energy electromagnetic pulse weapons are being developed at an unprecedented rate. The reliable operation of electronic devices in complex electromagnetic environments has become a critical factor determining the outcome of modern warfare. Electromagnetic shielding is a key means of achieving electromagnetic protection. Its core principle involves using shielding structures to reflect and absorb electromagnetic energy, thereby effectively blocking electromagnetic radiation coupling pathways. Shielding effectiveness (SE) is typically evaluated by measuring the reduction in electromagnetic field strength at an observation point with and without the shielding structure. However, in practical applications, due to constraints imposed by manufacturing processes, signal transmission requirements, ventilation and heat dissipation requirements, shielded cavities inevitably contain certain apertures and gaps, such as cable feedthrough apertures, ventilation openings, and display windows. The existence of these apertures and gaps significantly degrades the shielding performance, creating pathways for radiation coupling that allow external electromagnetic fields to penetrate the cavity, thereby interfering with or even damaging the cavity's internal components. Therefore, investigating the electromagnetic shielding performance of metallic cavities is vital for guaranteeing the reliable functioning of airborne electronic systems.

Currently, research methods for addressing metallic cavity shielding issues are broadly classified into numerical, analytical, and experimental approaches. Numerical methods include the finite-difference time-domain method [1], transmission line matrix method [2], and method of moments [3]. While these methods can achieve high-precision computational results through accurate modeling of cavity structures, they demand significant computational resources and time costs. Analytical methods primarily include the small aperture coupling theory [4], the equivalent circuit method [5, 6], and the Baum-Liu-Tesche (BLT) equation method [7]. These methods offer distinct advantages such as high computational efficiency and a streamlined modeling process, enabling rapid analysis and evaluation of the SE and resonant characteristics of metallic cavities.

Submitted On: August 18, 2025
Accepted On: November 21, 2025

https://doi.org/10.13052/2025.ACES.J.401108

In recent years, significant advancements have been made in extending Robinson's classical equivalent circuit model and the BLT equation method. Researchers have further refined the circuit model, thereby extending the prediction method to higher-order modes over a broader frequency range [8]. However, this approach remains limited to single-cavity structures and does not adequately clarify its applicability to complex multi-stage cascaded cavities. Further extensions have been applied to cavities featuring aperture arrays and two cascaded double-layer cavities [9, 10]. Although some of these studies have considered the influence of incident wave angles and the adaptability to double-layer structures, they still fail to resolve the challenges for irregular multi-stage cascaded cavities. An extended hybrid analytical model has been put forward that considers the effects of central, eccentric apertures, higher-order modes, and aperture arrays in multi-cavity structures [11, 12]. However, reference [11] only considers the configuration of aperture arrays. Reference [12] only analyzes resonant characteristics in the low-frequency range (0∼1 GHz) and did not extend to higher-order resonant behavior at higher frequencies. Furthermore, studies on irregular cavities also focus on low-frequency (0∼1 GHz) resonances and do not examine the effects of eccentric apertures and arbitrary observation points [13, 14]. Additionally, studies on complex cavity structures with internal sub-cavities do not consider aperture array effects or high-frequency higher-order resonant responses [15]. In summary, existing research still has the following main limitations: (a) Most methods do not systematically consider the impact of plane-wave incidence-angles on SE; (b) There is a prevalent assumption that cavities are ideal conductors, neglecting the practical effects of lossy conducting materials; (c) The majority of studies focus on simple single-cavity and regular multi-cavity structures, lacking targeted analyses for irregular and complex multi-stage cascaded cavities; (d) Some works only address fundamental mode resonance and SE in low-frequency ranges, lacking in-depth exploration of higher-order resonant characteristics at high frequencies.

This paper presents a hybrid analytical method that integrates the equivalent circuit method, electromagnetic topology theory, and the generalized BLT equation. This method systematically incorporates two key factors, namely plane-wave incidence-angle effects and lossy conducting material properties, and is further extended to stepped cavities and series-parallel hybrid cascaded three-layer cavities. The method enables rapid and accurate evaluation of the SE and high-frequency higher-order resonant characteristics of lossy, complex metallic cavities with eccentric apertures, aperture arrays, and arbitrarily positioned observation points. First, a refined equivalent circuit model of apertured cavities is constructed based on equivalent circuit theory. Subsequently, using electromagnetic topology theory, a corresponding signal flow graph is established to characterize the propagation and coupling mechanisms of electromagnetic fields, which culminates in the derivation of the generalized BLT equations. Finally, the equivalent circuit method is reintroduced to calculate the SE.

II. THEORETICAL DERIVATION OF THE ANALYTICAL METHOD

This section presents the theoretical foundation of the hybrid analytical method for evaluating the SE of shielded cavities, which is further extended to stepped cavities and series-parallel hybrid cascaded three-layer cavities.

A. Modeling of shielded cavities

The geometric model of the rectangular metallic cavity is illustrated in Fig. 1. The cavity has dimensions of $a\times b\times d$. The aperture, with dimensions of $l\times w$, is centered at (x_0, y_0). The coordinates of an arbitrary point P are (x_p, y_p, z_p).

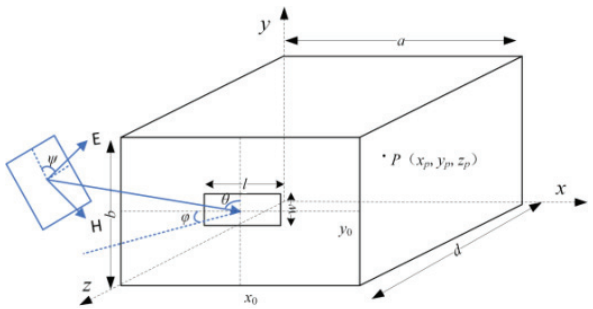

Fig. 1. Apertured shielded cavity under plane-wave excitation.

The incident electric field $\boldsymbol{E}$ can be decomposed into the $\boldsymbol{x}$, $\boldsymbol{y}$, and $\boldsymbol{z}$ components [16]. The analytical expressions for these components are given by:

$$\begin{aligned}\boldsymbol{E} &= \hat{\boldsymbol{x}}(\cos\varphi\sin\psi - \sin\varphi\cos\theta\cos\psi)E_0 \\ &\quad + \hat{\boldsymbol{y}}(\sin\theta\cos\psi)E_0 \\ &\quad - \hat{\boldsymbol{z}}(\cos\varphi\cos\theta\cos\psi + \sin\varphi\sin\psi)E_0 \\ &= \hat{\boldsymbol{x}}F_{px}E_0 + \hat{\boldsymbol{y}}F_{py}E_0 + \hat{\boldsymbol{z}}F_{pz}E_0. \end{aligned} \quad (1)$$

The amplitude of the electric field E is denoted by E_0, and the constant terms of E are defined by the polarization factors F_{px}, F_{py}, and F_{pz}.

The propagation vector β is given by:

$$\begin{aligned}\boldsymbol{\beta} &= -\hat{\boldsymbol{x}}(\sin\varphi\sin\theta)\beta_0 - \hat{\boldsymbol{y}}(\cos\theta)\beta_0 \\ &\quad - \hat{\boldsymbol{z}}(\cos\varphi\sin\theta)\beta_0 \\ &= \hat{\boldsymbol{x}}F_{ix}\beta_0 + \hat{\boldsymbol{y}}F_{iy}\beta_0 + \hat{\boldsymbol{z}}F_{iz}\beta_0. \end{aligned} \tag{2}$$

Here, the constant terms in each direction are defined by the incident factors F_{ix}, F_{iy}, and F_{iz}.

The equivalent circuit for an apertured shielded cavity is shown in Fig. 2.

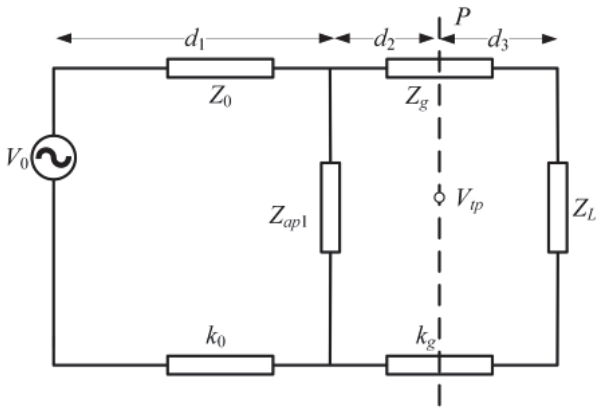

Fig. 2. Equivalent circuit for apertured cavity under plane-wave excitation.

The voltage V_0 represents the incident plane-wave's equivalent voltage source, Z_0 denotes free space's characteristic impedance, while Z_g denotes the characteristic impedance, and k_g denotes the propagation constant. The voltage at point P is denoted by V_{tp}.

Assuming that the cavity is made of an ideal conductor, the equivalent impedance of the aperture is expressed as:

$$Z_{ap} = \frac{1}{2}\cdot\frac{l}{a}jC_m Z_{0s}\tan\left(\frac{k_0 l}{2}\right), \tag{3}$$

$$C_m = \sin\frac{m\pi x_0}{a}\cos\frac{n\pi y_0}{b}, \tag{4}$$

$$Z_{0s} = 120\pi^2\left(\ln\left(2\frac{1+\sqrt[4]{1-(w_e/b)^2}}{1-\sqrt[4]{1-(w_e/b)^2}}\right)\right)^{-1}, \tag{5}$$

$$k_0 = \frac{2\pi}{\lambda}, \tag{6}$$

$$w_e = w - \frac{5t}{4\pi}\left(1+\ln\frac{4\pi w}{t}\right). \tag{7}$$

Here, C_m is the aperture position factor.

When the cavity is made of lossy conducting materials, the equivalent impedance is modified to:

$$Z_{ap} = \frac{1}{2}\cdot\frac{l}{a}C_m Z_{0s}\frac{Z_L + jZ_{0s}\tan\frac{k_0 l}{2}}{Z_{0s} + jZ_L\tan\frac{k_0 l}{2}}, \tag{8}$$

$$Z_L = (1+j)\sqrt{\frac{\omega\mu}{2\sigma}}. \tag{9}$$

Here, Z_L denotes the characteristic impedance of the cavity made of lossy conducting material.

For an array of n apertures, the total equivalent impedance is defined as the sum of the equivalent impedances of each individual aperture.

$$Z_{ap} = \sum_{i=1}^{n} Z_{api}. \tag{10}$$

B. Establishment and solution of the generalized BLT equation

The shielded cavity signal flow diagram is presented in Fig. 3.

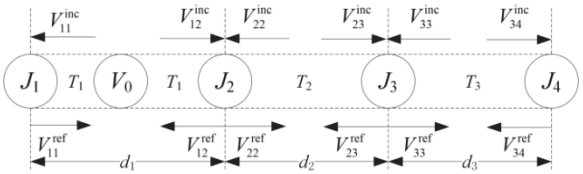

Fig. 3. Shielded cavity signal flow diagram.

Here the nodes J_1, J_2, J_3, and J_4 correspond to the external observation point, the aperture, the internal observation point, and the cavity bottom, respectively. The paths T_1, T_2, and T_3 represent distinct energy transmission channels, V^{inc} and V^{ref} denote the incident voltage and the reflected voltage, respectively.

The generalized BLT equation for determining the target voltage is expressed as:

$$V = (U+\rho)(\Gamma-\rho)^{-1}S. \tag{11}$$

In the scattering matrix, the reflection coefficient ρ_1 is zero, while ρ_2, ρ_3, and ρ_4 are expressed as:

$$\rho_2 = \begin{bmatrix} \dfrac{Y_0 - Y_g - Y_{ap}}{Y_0 + Y_g + Y_{ap}} & \dfrac{2Y_g}{Y_0 + Y_g + Y_{ap}} \\ \dfrac{2Y_0}{Y_0 + Y_g + Y_{ap}} & \dfrac{Y_g - Y_0 - Y_{ap}}{Y_0 + Y_g + Y_{ap}} \end{bmatrix},$$

$$\rho_3 = \begin{bmatrix} 0 & 1 \\ 1 & 0 \end{bmatrix}, \quad \rho_4 = \left(\frac{Z_L - Z_g}{Z_L + Z_g}\right). \tag{12}$$

Here, Y_0 is the free space admittance, Y_g is the cavity admittance, and Y_{ap} is the aperture admittance.

Assuming the cavity is made of an ideal conducting material, the characteristic impedances for TE modes and TM modes in a rectangular waveguide, denoted as Z_g^{TE} and Z_g^{TM}, and the k_g within the cavity are defined as follows:

$$\begin{aligned} Z_{\mathrm{g}}^{\mathrm{TE}} &= Z_0/\sqrt{1-(m\lambda/2a)^2-(n\lambda/2b)^2} \\ Z_{\mathrm{g}}^{\mathrm{TM}} &= Z_0\sqrt{1-(m\lambda/2a)^2-(n\lambda/2b)^2}, \end{aligned} \tag{13}$$

$$k_g = k_0\sqrt{1-(m\lambda/2a)^2-(n\lambda/2b)^2}. \tag{14}$$

For a cavity made of lossy conducting materials, the characteristic impedance and propagation constant of the cavity are expressed as:

$$\begin{aligned} Z_g^{\mathrm{TE}} &= Z_0 k_0/k_g \\ Z_g^{\mathrm{TM}} &= Z_0 k_g/k_0, \end{aligned} \tag{15}$$

$$k_{\mathrm{g}} = -j\gamma, \tag{16}$$

$$\begin{aligned} \gamma^2 = &-k_z^2-(1-j)\delta \\ &\times\left[\frac{\varepsilon_{0m}}{a}\left(k_{c0}^2+k_z^2\frac{k_x^2}{k_{c0}^2}\right)+\frac{\varepsilon_{0n}}{b}\left(k_{c0}^2+k_z^2\frac{k_y^2}{k_{c0}^2}\right)\right], \end{aligned} \tag{17}$$

$$k_z = \sqrt{k_0^2-k_{c0}^2}, \tag{18}$$

$$k_{c0} = \sqrt{k_x^2+k_y^2}, \tag{19}$$

$$k_x = \frac{m\pi}{a}, \quad k_y = \frac{n\pi}{b}, \quad \delta = \frac{1}{\sqrt{\pi f\sigma\mu_0}}. \tag{20}$$

Here, k_z is the phase constant, k_{c0} is the cutoff wave number, ε_{0m} and ε_{0n} are the Norimura coefficients, and δ is the skin depth.

The propagation coefficients Γ_1, Γ_2, and Γ_3 in the propagation matrix are given by:

$$\begin{aligned} \Gamma_1 = \begin{bmatrix} 0 & \mathrm{e}^{jk_0d_1} \\ \mathrm{e}^{jk_0d_1} & 0 \end{bmatrix}, \quad \Gamma_2 = \begin{bmatrix} 0 & \mathrm{e}^{jk_gd_2} \\ \mathrm{e}^{jk_gd_2} & 0 \end{bmatrix}, \\ \Gamma_3 = \begin{bmatrix} 0 & \mathrm{e}^{jk_gd_3} \\ \mathrm{e}^{jk_gd_3} & 0 \end{bmatrix}. \end{aligned} \tag{21}$$

The excitation source S is expressed as:

$$S = \begin{bmatrix} 0.5V_0\mathrm{e}^{jk_0d_{11}} & -0.5V_0\mathrm{e}^{jk_0d_{12}} & 0 & 0 & 0 & 0 \end{bmatrix}^{\mathrm{T}}. \tag{22}$$

Here, the sum of d_{11} and d_{12} is equal to d_1.

According to equation (11), voltage $V_{tp} = V_{33}$. The specific expression for the TE mode voltage response component is given by:

$$\begin{aligned} E_{px}^{\mathrm{TE}} &= -F_{px}F_{iz}\frac{an}{bm}V_{tp}C_{px} \\ E_{py}^{\mathrm{TE}} &= F_{py}F_{iz}V_{tp}C_{py} \\ E_{pz}^{\mathrm{TE}} &= 0. \end{aligned} \tag{23}$$

Here $m \neq 0$, and the position coefficients C_{px} and C_{py} of the observation point are expressed as follows:

$$\begin{aligned} C_{px} &= \cos\frac{m\pi x_p}{a}\sin\frac{n\pi y_p}{b} \\ C_{py} &= \sin\frac{m\pi x_p}{a}\cos\frac{n\pi y_p}{b}. \end{aligned} \tag{24}$$

The specific expression for the TM mode is written as:

$$\begin{aligned} E_{px}^{\mathrm{TM}} &= F_{px}F_{iz}\frac{bm}{an}V_{tp}C_{px} \\ E_{py}^{\mathrm{TM}} &= F_{py}F_{iz}V_{tp}C_{py} \\ E_{pz}^{\mathrm{TM}} &= -F_{pz}F_{iz}\frac{bk_{c0}^2}{n\pi k_g}V_{tp1}C_{pz}. \end{aligned} \tag{25}$$

Here $m \neq 0, n \neq 0, V_{tp1}$ is the maximum voltage response of the observation point in TM mode. The position coefficient C_{pz} of the observation point is given by:

$$C_{pz} = \sin\left(\frac{m\pi x_p}{a}\right)\sin\left(\frac{n\pi y_p}{b}\right). \tag{26}$$

As shown in equations (27) and (28). The total voltage is obtained by:

$$\begin{aligned} E_{px} &= \sum_{m,n}\left(E_{px}^{\mathrm{TE}}+E_{px}^{\mathrm{TM}}\right) \\ E_{py} &= \sum_{m,n}\left(E_{py}^{\mathrm{TE}}+E_{py}^{\mathrm{TM}}\right) \\ E_{pz} &= \sum_{m,n}E_{pz}^{\mathrm{TM}}. \end{aligned} \tag{27}$$

$$E_{\mathrm{total}} = \sqrt{E_{px}^2+E_{py}^2+E_{pz}^2}. \tag{28}$$

Without the shielded cavity, the voltage at the observation point is expressed as:

$$E_{p0} = \frac{1}{2}V_0\mathrm{e}^{-jk_0(d_{12}+t+d_2)}. \tag{29}$$

Therefore, the SE can be calculated using equation (30).

$$SE = -20\lg\left|\frac{E_{\mathrm{total}}}{E_{p0}}\right|. \tag{30}$$

C. Extension of analytical methods

This section extends the aforementioned methods to calculate the SE of stepped cavities and series-parallel hybrid cascaded three-layer cavities.

1. Stepped cavity

The geometric model of the stepped shielded cavity is shown in Fig. 4, where the heights of cavity 1 and cavity 2 are denoted by b_1 and b_2. The equivalent circuit model and signal flow diagram corresponding to this configuration are shown in Figs. 5 and 6.

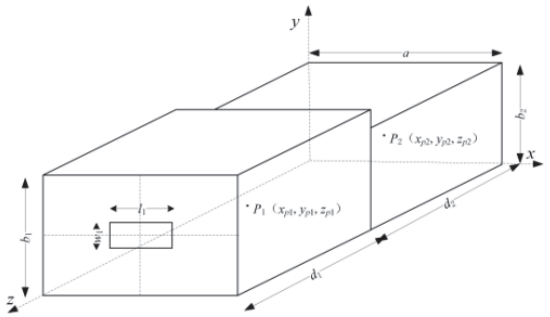

Fig. 4. Geometric modelling for stepped cavity.

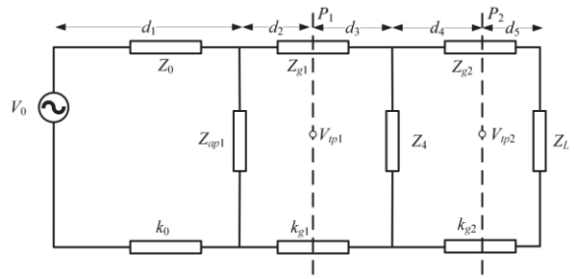

Fig. 5. Equivalent circuit for stepped cavity.

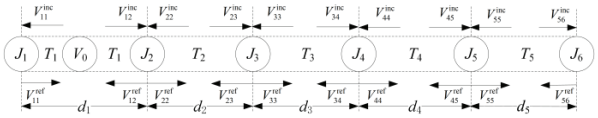

Fig. 6. Signal flow diagram for stepped cavity.

Here, the node J_4 represents the stepped structure. The corresponding scattering matrix ρ_4 is given by:

$$\rho_4 = \begin{bmatrix} \dfrac{Y_{g1}-Y_{g2}-Y_4}{Y_{g1}+Y_{g2}+Y_4} & \dfrac{2Y_{g2}}{Y_{g1}+Y_{g2}+Y_4} \\ \dfrac{2Y_{g1}}{Y_{g1}+Y_{g2}+Y_4} & \dfrac{Y_{g2}-Y_{g1}-Y_4}{Y_{g1}+Y_{g2}+Y_4} \end{bmatrix}. \tag{31}$$

Here $Y_{g1} = 1/Z_{g1}$ and $Y_{g2} = 1/Z_{g2}$ are the admittances of electromagnetic waves propagating in the cavity 1 and cavity 2, respectively, and $Y_4 = 1/Z_4$ is the admittance of the stepped structure, which is expressed as:

$$Z_4 = \frac{-j\lambda_g Z_{g1}}{4b_1}\left[\ln\frac{1-\alpha^2}{4\alpha}\left(\frac{1+\alpha}{1-\alpha}\right)^{\frac{1}{2}\left(\frac{\alpha+1}{\alpha}\right)} + \frac{2}{A}\right]^{-1}, \tag{32}$$

$$\alpha = b_2/b_1, \tag{33}$$

$$A = \left(\frac{1+\alpha}{1-\alpha}\right)^{2\alpha}\frac{1+\sqrt{1-\left(2b_1/\lambda_g\right)^2}}{1-\sqrt{1-\left(2b_1/\lambda_g\right)^2}}\cdot\frac{1+3\alpha^2}{1-\alpha^2}, \tag{34}$$

$$\lambda_g = \lambda/\sqrt{1-(\lambda/2a)^2-(\lambda/2b_2)^2}. \tag{35}$$

The voltage at P_1 and P_2 can be calculated as $V_{tp1} = V_{33}$ and $V_{tp2} = (b_1/b_2)\cdot V_{55}$. Similarly, the SE of the stepped cavity can be determined using this proposed hybrid analytical algorithm.

2. Series-parallel hybrid cascaded three-layer cavity

The geometric model of the series-parallel hybrid cascaded three-layer cavity is shown in Fig. 7. Cavity 1 has a height of b, while cavity 2 and cavity 3 are arranged in a parallel configuration, with heights of b_1 and b_2. The corresponding equivalent circuit model and signal flow diagram are shown in Figs. 8 and 9.

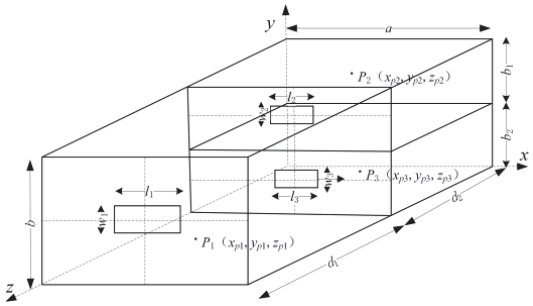

Fig. 7. Geometric modeling for series-parallel hybrid cascaded three-layer cavity.

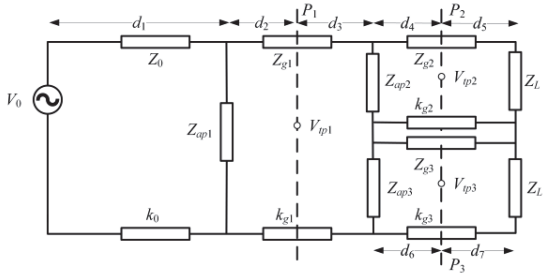

Fig. 8. Equivalent circuit for series-parallel hybrid cascaded three-layer cavity.

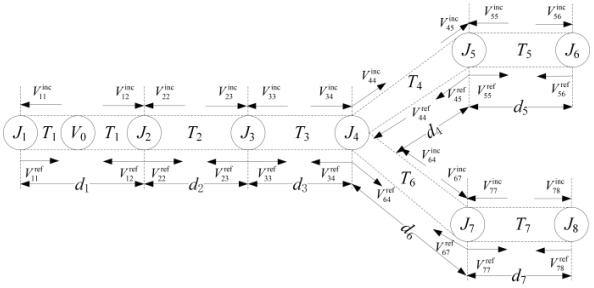

Fig. 9. Signal flow diagram for series-parallel hybrid cascaded three-layer cavity.

In the signal flow diagram, node J_4 represents the two apertures of cavity 2 and cavity 3 and is modeled as a three-port network. Node J_5 corresponds to the observation point P_2 in cavity 2, while node J_6 represents the bottom of cavity 2. Similarly, node J_7 corresponds to the observation point P_3 in cavity 3, and node J_8 represents the bottom of cavity 3. The calculation method for the scattering matrices associated with each node remains unchanged. The scattering matrix ρ_4 corresponding to node J_4 is given by:

$$\rho_4 = \begin{bmatrix} S_{11}^4 & S_{12}^4 & S_{13}^4 \\ S_{21}^4 & S_{22}^4 & S_{23}^4 \\ S_{31}^4 & S_{32}^4 & S_{33}^4 \end{bmatrix}, \tag{36}$$

$$\begin{aligned} S_{11}^4 = (&Y_{g1}Y_{g3} + Y_{g1}Y_{ap3} + Y_{g1}Y_{ap2} + Y_{g1}Y_{g2} \\ &- Y_{g3}Y_{g2} - Y_{ap3}Y_{g2} - Y_{ap2}Y_{g3} - Y_{ap2}Y_{ap3})/Y_{t4}, \end{aligned} \tag{37}$$

$$S_{12}^4 = 2(Y_{g1}Y_{g3} + Y_{g1}Y_{ap3})/Y_{t4}, \tag{38}$$

$$S_{13}^4 = 2(Y_{g1}Y_{g2} + Y_{g1}Y_{ap2})/Y_{t4}, \tag{39}$$

$$S_{21}^4 = 2(Y_{g1}Y_{g2} + Y_{g2}Y_{g3} + Y_{g2}Y_{ap3})/Y_{t4}, \tag{40}$$

$$\begin{aligned} S_{22}^4 = (&Y_{g1}Y_{g2} + Y_{g2}Y_{g3} + Y_{g2}Y_{ap3} - Y_{g1}Y_{ap2} \\ &- Y_{g3}Y_{ap} - Y_{ap2}Y_{ap3} - Y_{g1}Y_{ap3} - Y_{g1}Y_{g3})/Y_{t4}, \end{aligned} \tag{41}$$

$$S_{23}^4 = S_{32}^4 = 0, \tag{42}$$

$$S_{31}^4 = 2(Y_{g1}Y_{g3} + Y_{g2}Y_{g3} + Y_{g3}Y_{ap2})/Y_{t4}, \tag{43}$$

$$\begin{aligned} S_{33}^4 = (&Y_{g1}Y_{g3} + Y_{g2}Y_{g3} + Y_{g3}Y_{ap2} - Y_{g1}Y_{ap3} \\ &- Y_{g2}Y_{ap3} - Y_{g1}Y_{ap3} - Y_{g1}Y_{g2} - Y_{ap2}Y_{ap3})/Y_{t4}, \end{aligned} \tag{44}$$

$$\begin{aligned} Y_{t4} = &Y_{g1}Y_{g3} + Y_{g1}Y_{ap3} + Y_{g1}Y_{ap2} + Y_{g1}Y_{g2} \\ &+ Y_{g2}Y_{g3} + Y_{g2}Y_{ap3} + Y_{g3}Y_{ap2} + Y_{ap2}Y_{ap3}. \end{aligned} \tag{45}$$

Here Y_{g1}, Y_{g2}, and Y_{g3} represent the admittances of electromagnetic waves propagating in cavity 1, cavity 2, and cavity 3, while Y_{ap2} and Y_{ap3} denote the admittances of the apertures in cavity 2 and cavity 3.

The propagation coefficients, denoted by Γ_1, Γ_2, and Γ_3, are the same as those previously described, while the expressions for Γ_4 and Γ_5 are:

$$\Gamma_4 = \begin{bmatrix} 0 & 0 & e^{jk_{g2}d_4} & 0 & 0 & 0 \\ 0 & 0 & 0 & 0 & 0 & e^{jk_{g2}d_5} \\ e^{jk_{g2}d_4} & 0 & 0 & 0 & 0 & 0 \\ 0 & 0 & 0 & 0 & e^{jk_{g3}d_6} & 0 \\ 0 & 0 & 0 & e^{jk_{g3}d_6} & 0 & 0 \\ 0 & e^{jk_{g2}d_5} & 0 & 0 & 0 & 0 \end{bmatrix},$$

$$\Gamma_5 = \begin{bmatrix} 0 & \mathrm{e}^{jk_{g3}d_7} \\ \mathrm{e}^{jk_{g3}d_7} & 0 \end{bmatrix}. \tag{46}$$

Here k_{g2} and k_{g3} denote the propagation constants in cavity 2 and cavity 3.

The voltage at P_1 is $V_{tp1} = V_{33}$, the voltage at P_2 is $V_{tp2} = (b/b_1) \cdot V_{55}$, and the voltage at P_3 is $V_{tp3} = (b/b_2) \cdot V_{77}$. Similarly, the SE of the series-parallel hybrid cascaded shielded cavity can be calculated using this proposed hybrid analytical algorithm.

III. NUMERICAL VERIFICATION

To validate the hybrid analytical method proposed in this study, several cavity models were designed to perform numerical verification of the SE. Comparisons and analyses between the results of the proposed method and those from CST simulations were carried out to confirm the reliability of this method.

The cavity models were fabricated from a lossy conducting material with a magnetic permeability of 1.26×10^{-6} H/m and an electrical conductivity of 3.56×10^{7} S/m. The thickness of the walls was set as $t = 1$ mm. The incident plane-wave angles were specified as $\psi = 0^\circ$, $\varphi = 0^\circ$, and $\theta = 90^\circ$, whereby the wave is incident perpendicularly to the aperture plane along the $-z$ direction. The frequency range investigated spans from 0.1 to 3 GHz. The cavity dimensions, aperture dimensions, aperture positions, and observation point positions used in the models are summarized in Table 1.

Figure 10 presents the results for Case 1, the observation point lies at the top-left corner. The results demonstrate that the method enables accurate prediction of SE at eccentric locations, with excellent agreement between the analytical approach and CST simulations.

Figure 11 presents the results for Case 2, the aperture configuration consists of a 3×3 eccentric square aperture array. Due to the increased complexity of the aperture geometry, more modes must be considered compared to a single aperture, which results in additional resonance peaks. The analytical results from

Table 1: Parameter settings for calculation cases

Case No.	Cavity Dimensions (mm)	Aperture Dimensions (mm)	Aperture Positions (mm)	Observation Point Positions (mm)
1	$320 \times 160 \times 260$	40×20	$(160, 80)$	(55,140,85)
2	$320 \times 160 \times 260$	3×3 array, Each aperture:20 $\times$20, Spacing:4	$(60, 65)$	(225,140,255)
3	Cavity 1: $300 \times 130 \times 130$ Cavity 2: $300 \times 120 \times 240$	40×20	$(200, 60)$	(45,90,155)
4	Cavity 1: $300 \times 130 \times 130$ Cavity 2: $300 \times 120 \times 240$	2×2 array, Each aperture:20 $\times$20, Spacing: 4	$(212, 72)$	(150,60,120)
5	Cavity 1: $300 \times 120 \times 160$	40×20	$(150, 60)$	$P_1(150, 60, 165)$
	Cavity 2: $300 \times 60 \times 100$	40×20	$(150, 90)$	$P_2(150, 90, 65)$
	Cavity 3 : $300 \times 60 \times 100$	40×20	$(150, 30)$	$P_3(150, 30, 65)$

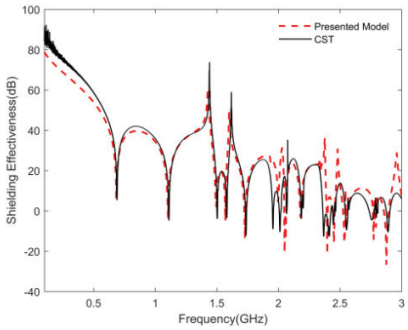

Fig. 10. SE results of Case 1.

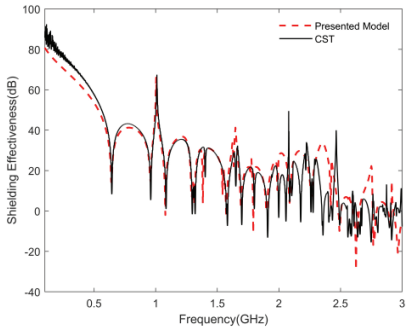

Fig. 12. SE results of Case 3.

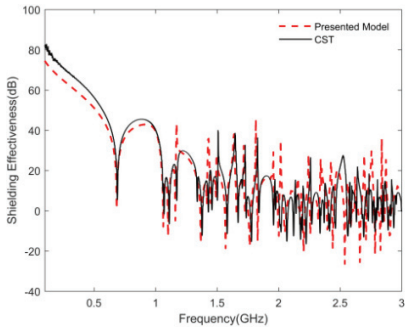

Fig. 11. SE results of Case 2.

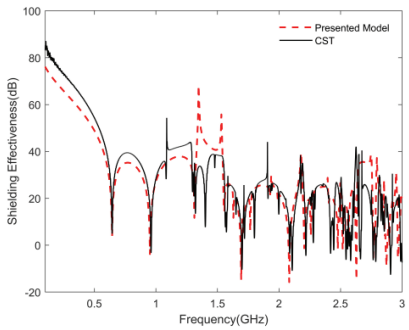

Fig. 13. SE results of Case 4.

the proposed method exhibit a high degree of agreement with CST simulation results in both amplitude and resonant frequencies. These results demonstrate that the proposed method can accurately address both central aperture and eccentric aperture array configurations, enabling reliable calculation of SE and identification of resonant points for eccentric observation points.

Figure 12 presents the results for Case 3 of the stepped cavity. In this case, the eccentric aperture is situated at the bottom-right corner. The results derived from the method proposed herein display strong consistency with CST simulation results in both amplitude and resonant frequencies, which effectively validates the accuracy of the method when extended to stepped cavities with eccentric apertures.

Figure 13 presents the results for Case 4 of the stepped cavity, The aperture configuration consists of a 2×2 eccentric square aperture array, with the observation point situated along the central axis of Cavity 2. These results demonstrate that this method can accurately predict the SE for stepped cavities with eccentric aperture arrays, which further confirms its applicability to complex aperture configurations.

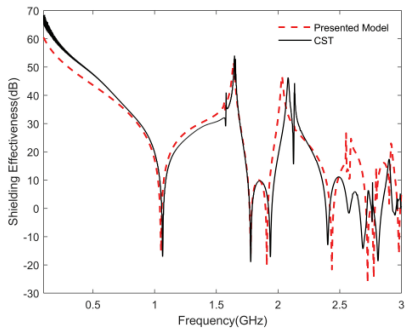

Fig. 14. SE results of Case 5 point P_1.

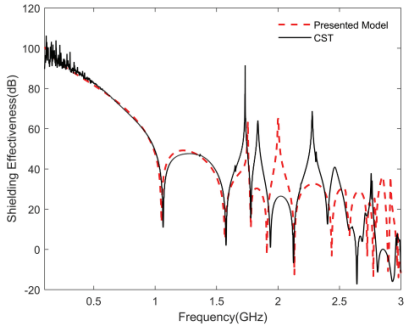

Fig. 15. SE results of Case 5 point P_2.

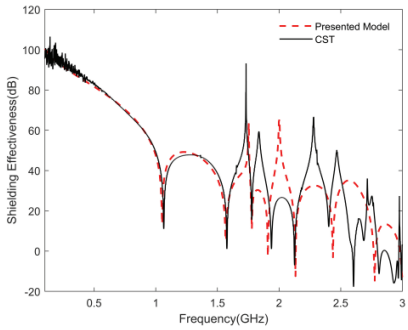

Fig. 16. SE results of Case 5 point P_3.

Figures 14, 15, and 16 present the results for Case 5 of the series-parallel hybrid cascaded three-layer cavity, findings from the proposed method exhibit strong agreement with CST simulation results in both amplitude and resonant frequencies, indicating that the method is suitable for calculating the SE of complex cavity structures. However, as the frequency increases, the discrepancy between the calculated and simulated results becomes more pronounced, though the overall trend remains consistent. Additionally, since cavity 2 and cavity 3 are arranged in parallel, their SE and resonant frequencies are identical if their aperture sizes and observation point positions are the same. Furthermore, the inner cavity exhibits resonances corresponding to those of the outer cavity. This is attributed to the higher energy levels in the outer cavity at its resonant frequencies, which, when coupled to the inner cavity, cause a reduction in the SE in the inner cavity at those frequencies.

All numeric calculations were carried out on one computer, fitted with Intel Core i3-10110U CPU @2.10 GHz and 8 GB of RAM. The proposed hybrid analytical method took no more than 20 seconds per calculation, whereas the corresponding CST simulations took more than 20 minutes. This substantial reduction in computation time highlights the distinct advantage of the proposed method in terms of computational efficiency.

IV. CONCLUSION

This paper presents a hybrid analytical method that integrates the equivalent circuit method, electromagnetic topology theory, and generalized BLT equations, while systematically accounting for plane-wave incidence-angle effects and lossy conducting material properties. The approach enables rapid evaluation of both the SE and the resonant behavior of lossy metallic cavities. Compared with the results from CST simulations, the method exhibits excellent performance in both accuracy and computational efficiency. By introducing aperture and observation point position factors, the method is applicable to arbitrarily eccentric apertures, aperture arrays, and arbitrarily positioned observation points. Even at elevated frequencies, the method can quickly and accurately predict the SE and higher-order resonant frequencies. Furthermore, the proposed hybrid analytical method has been successfully extended to various complex cavity structures, including stepped cavities and series-parallel hybrid cascaded three-layer cavities, thus demonstrating its broad applicability for SE analysis in complex cavity configurations. This work provides a simple and efficient approach for SE calculations in complex shielding structures, and numerical validation via CST simulations has confirmed its efficacy. Future work will focus on experimental validation to further corroborate these numerical findings.

ACKNOWLEDGMENT

This work was supported by the National Natural Science Foundation of China (Grant 51375490).

REFERENCES

[1] P. Radhakrishnan, L. Koraqi, T. Claeys, J. Catrysse, and D. Pissoort, "FDTD simulation and experimental comparative study of a Gasket's shielding effectiveness characterization: Dipole Vs. log-periodic antenna," *IEEE Trans. Electromagn. Compat.*, vol. 67, no. 2, pp. 598–608, Apr. 2025.

[2] Y. A. Medjaouri, K. Benzaoui, A. Ales, B. Rekioua, R. Tahmi, D. Peumans, J. Gyselinck, and Y. Rolain,

"Equivalent modeling of multilayered conductive composite materials for EMI shielding applications," *IEEE Trans. Dielectr. Electr. Insul.*, vol. 32, no. 4, pp. 1923–1929, Aug. 2025.

[3] M. Kalantari and S. H. H. Sadeghi, "An efficient method for computing the shielding effectiveness of arbitrary-shape multilayered composite enclosures," *IEEE Trans. Electromagn. Compat.*, vol. 66, no. 2, pp. 444–452, Apr. 2024.

[4] Z. Sun, W. Dong, D. Qin, L. Zheng, P. Qiu, C. Ding, X. Yang, and C. Jiao, "Approximate simulation of low frequency magnetic shielding of a rectangular shielding box with all walls perforated periodical holes," *Prog. Electromagn. Res. Lett.*, vol. 109, pp. 31–39, Feb. 2023.

[5] M. P. Robinson, J. D. Turner, D. W. P. Thomas, J. F. Dawson, M. D. Ganley, A. C. Marvin, S. J. Porter, T. M. Benson, and C. Christopoulos, "Shielding effectiveness of a rectangular enclosure with a rectangular aperture," *Electron. Lett.*, vol. 32, no. 17, pp. 1559–1560, Aug. 1996.

[6] A. Rabat, P. Bonnet, K. E. K. Drissi, and S. Girard, "Analytical models for electromagnetic coupling of an open metallic shield containing a loaded wire," *IEEE Trans. Electromagn. Compat.*, vol. 59, no. 5, pp. 1634–1637, Oct. 2017.

[7] S. Shen, Y. Wang, and P. Xing, "The prediction of shielding effectiveness of the rectangular enclosure with complex apertures based on the BLT equation," *IEICE Electron. Express*, vol. 22, no. 10, pp. 20250159-20250159, May 2025.

[8] M. C. Yin and P. A. Du, "An improved circuit model for the prediction of the shielding effectiveness and resonances of an enclosure with apertures," *IEEE Trans. Electromagn. Compat.,* vol. 58, no. 2, pp. 448–456, Apr. 2016.

[9] B. L. Nie, P. A. Du, and P. Xiao, "An improved circuital method for the prediction of shielding effectiveness of an enclosure with apertures excited by a plane wave," *IEEE Trans. Electromagn. Compat.*, vol. 60, no. 5, pp. 1376–1383, Oct. 2018.

[10] Y. Gong, Y. Li, and L. Jiang, "Efficient analytical method for the shielding effectiveness of an apertured enclosure based on the BLT equation," *IET Sci. Meas. Technol.*, vol. 14, no. 8, pp. 897–904, Sep. 2020.

[11] W. Shen, S. Wang, W. Li, H. Jin, and H. Zhang, "An extended hybrid analytical model for the shielding effectiveness prediction of a multi-cavity structure with numerous apertures," *Prog. Electromagn. Res. M.*, vol. 96, pp. 181–190, Sep. 2020.

[12] H. Jin, H. Zhang, Y. Ma, K. Chen, and X. Sun, "An analytical hybrid model for the shielding effectiveness evaluation of a dual-cavity structure with an aperture array," *Prog. Electromagn. Res. Lett.*, vol. 91, pp. 109–116, May 2020.

[13] J. Ren, Y. Pan, Z. Zhou, and T. Zhang, "Research on testing method for shielding effectiveness of irregular cavity based on field distribution characteristics," *Electronics*, vol. 12, no. 4, p. 1035, Feb. 2023.

[14] K. Chen, H. Jin, H. Zhang, X. Zhang, and Z. Liu, "A hybrid analytical model for estimating the shielding effectiveness of an irregular cavity structure with aperture arrays," in *22nd International Symposium on High Voltage Engineering* (*ISH 2021*) *Hybrid Conference*, Xi'an, China, pp. 949–954, 2021.

[15] J. C. Zhou and X. T. Wang, "An efficient method for predicting the shielding effectiveness of an apertured enclosure with an interior enclosure based on electromagnetic topology," *Applied Computational Electromagnetics Society (ACES) Journal*, vol. 37, no. 10, pp. 1014–1020, Oct. 2022.

[16] J. Shim, D. G. Kam, J. H. Kwon, and J. Kim, "Circuital modeling and measurement of shielding effectiveness against oblique incident plane wave on apertures in multiple sides of rectangular enclosure," *IEEE Trans Electromagn. Compat.*, vol. 52, no. 3, pp. 566–577, Aug. 2010.

Ai-Guo Gao was born in Lianyungang, Jiangsu Province, China, in 1984. He received his B.S. degree in communication engineering from Ocean University of China, Qingdao, in 2007, and the M.S. degree in Communication and Information Systems from Naval University of Engineering, Wuhan, in 2009. He is currently working toward the Ph.D. degree in Aerospace Science and Technology with Naval Aviation University, Yantai, China. His research interests include electromagnetic shielding and electromagnetic compatibility technology.

Da-Zhao Yu was born in Yuncheng, Shandong Province, China, in 1976. He received his Ph.D. degree from Naval Aviation University, Yantai, in 2008. He is currently a Professor with the School of Basic Sciences for Aviation, Naval Aviation University. His research interests include flight safety, electromagnetic compatibility measurement, and corrosion protection and control.

Yi-Jiang Du was born in Jincheng, Shanxi Province, China, in 1989. He received his M.S. degree from Beihang University, Beijing, in 2018. He is currently a Lecturer with the School of Basic Sciences for Aviation, Naval Aviation University. His research interests include flight mechanics and flight control.

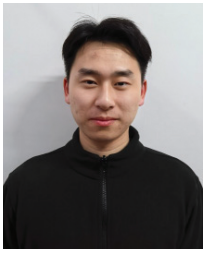

He-Xiang Huang was born in Wuhan, Hubei Province, China, in 2001. He is currently working toward the M.S. degree in Aerospace Science and Technology with Naval Aviation University, Yantai. His research interests include electromagnetic compatibility modeling and testing techniques.

Testing and Remote Communication of S-Parameters for Biomedical Applications Using Miniature VNA Hardware

Kenneth Y. Hora, Lisa Elmiladi, Atef Z. Elsherbeni, and Peter H. Aaen

Department of Electrical Engineering, Colorado School of Mines, Golden, CO 80401, USA
khora@mines.edu, lelmiladi@mines.edu, aelsherb@mines.edu, paaen@mines.edu

Abstract **–** Remote sensing of lactate is important in both healthcare settings and monitoring athlete's performance. Many approaches for noninvasive remote sensing of lactate use on-body resonator circuits that measure changes in S-parameters to determine lactate concentration. However, due to their large size, most commercial vector network analyzers (VNAs) are impractical for taking on-body measurements of moving participants. This paper presents an approach that uses smaller, hobbyist, VNAs to create practical on-body measurement systems.

Index Terms **–** Bluetooth, lactate, MATLAB, NanoVNA, noninvasive sensing, python, VNA, wireless communication.

I. INTRODUCTION

Lactate monitoring within the human body can provide doctors, athletic trainers, and other health professionals with important information about their patients. This might include monitoring patients who have been in low oxygen situations or monitoring the exhaustion of athletes. Currently, many techniques for measuring lactate concentration require invasive procedures, such as pricking a finger to draw blood. There has been considerable development in noninvasive methods to measure lactate concentration, which often measure sweat, saliva, or tears; however, these methods often require characterization of these samples from external testing devices [1].

Recently, there has been additional development in RF and microwave-based devices examining whether the dielectric properties of lactate can be used with noninvasive, on-body sensors to detect lactate concentration [2–5]. Often, these devices use resonators or similar circuitry and detect shifts in reflection and transmission coefficients over various frequencies to determine the concentration of lactate. While some approaches use transmission responses for characterization [2], these microwave circuits are often connected to vector network analyzers (VNAs) [3–5].

Current VNAs are often very large with respect to on-body sensors that require the measurement of S-parameters. Although some handheld VNAs do exist, such as the Keysight FieldFox [6], they are often still impractical for on-body measurements. However, within the past 4 years, hobbyist VNAs, such as the NanoVNA [7] and NanoVNA v2 by NanoRFE [8] have become widely available and provide relatively small footprints (though at the cost of measurement accuracy) that can be attached to a person for remote lactate sensing.

This paper explores the NanoVNA-H and NanoVNA v2 hardware as potential measurement devices for noninvasive lactate sensors.

II. NANOVNA HARDWARE

A. NanoVNA-H

The NanoVNA-H is a compact device that boasts a variety of hardware capabilities and interfaces designed to cater to a broad spectrum of RF measurement needs. It includes two ports, labeled Port 1 and Port 2, and is capable of measuring S_{11} and S_{21}. The NanoVNA-H is equipped with a simple user interface, consisting of a touchscreen display that can be detached to render the device more compact, enhancing portability for field use or in testing environments where physical cables are impractical or hazardous. Additional specifications of the NanoVNA-H may be found in Table 1 [7, 9].

Table 1: NanoVNA-H characteristics

Frequency Range	50 kHz to 900 MHz
Frequency Resolution	100 Hz
Noise Floor	-40 dB
Max Sweep Points	1024
Interface	micro-USB, hardware UART

Moreover, NanoVNA-H hardware is designed to interface seamlessly with numerous software and platforms. One of the key interfaces is the UART (Universal Asynchronous Receiver/Transmitter), a hardware communication protocol that facilitates serial communication between devices [10]. This interface allows

Submitted On: September 18, 2025
Accepted On: October 14, 2025

https://doi.org/10.13052/2025.ACES.J.401109

the NanoVNA-H to communicate over Bluetooth with modules like the HC-05, enabling wireless connectivity. The Bluetooth module connects to the VNA via jumper wires attached to the VCC, Tx and Rx pins, and GND. The Tx and Rx pins enable bidirectional communication, allowing commands to be sent and data to be received over UART. This wireless capability not only extends the device's usability in different settings but also facilitates real-time data transfer to laptops or smartphones, eliminating the limitations imposed by cables.

B. NanoVNA v2

The NanoVNA v2 is an improved hobbyist VNA created by NanoRFE, but it is not based on the original NanoVNA-H design or derivatives [8]. Instead, it was designed to be more performant than previous hardware and was not designed to be compatible with the NanoVNA-H.

The NanoVNA v2 is a two-port network analyzer, capable of measuring S_{11} and S_{21}. The authors used a NanoVNA v2 (see Table 2) [11].

Table 2: NanoVNA v2 characteristics

Frequency Range	50 kHz to 3 GHz
Frequency Resolution	10 kHz
Noise Floor	−40 dB
Max Sweep Points	1024-65536 (firmware & PC dependent)
Interface	micro-USB

The NanoVNA v2 will interface with a host computer via USB and connects as a virtual serial port. Binary commands can be issued to the device to set sweep parameters or read data from the device [11].

III. WIRELESS COMMUNICATION INTERFACE WITH NANOVNA-H

The NanoVNA-H, while a compact and capable device for RF measurements, typically requires a direct USB connection for data interfacing, which limits its applicability for dynamic and remote sensing applications. This section presents the integration of an HC-05 wireless communication module, to enable remote operation and data acquisition from the NanoVNA-H.

The HC-05 module was selected for its ubiquity, ease of use, and sufficient data rate to transmit S-parameters effectively. Interfacing the module required firmware modifications to the NanoVNA-H, which were implemented following the support provided by DaveLapp [12]. The firmware release leverages the UART1 port for wireless data transmission when USB is not active.

A. Bluetooth module configuration

The HC-05 Bluetooth module was initially configured with AT commands to set the device name and baud rate, ensuring seamless communication with the NanoVNA-H. These configurations were critical for establishing a reliable link and compatibility with various operating systems and host devices.

B. Hardware configuration

The interfacing between the NanoVNA-H and the Bluetooth module involved connecting the Tx and Rx pins to the corresponding UART pads on the NanoVNA's printed circuit board (PCB). This hardware setup facilitated a virtual serial port over Bluetooth, allowing for the wireless transmission of measurement data. The UART connections are shown in Fig. 1. The device under test (DUT) was attached to Port 1 of the VNA so that it can be measured. This is shown in Figs. 1 and 2.

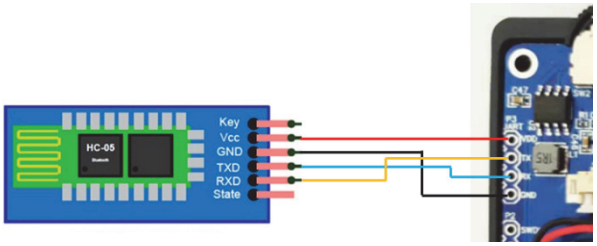

Fig. 1. UART interface pin connections between HC-05 Bluetooth module and NanoVNA-H.

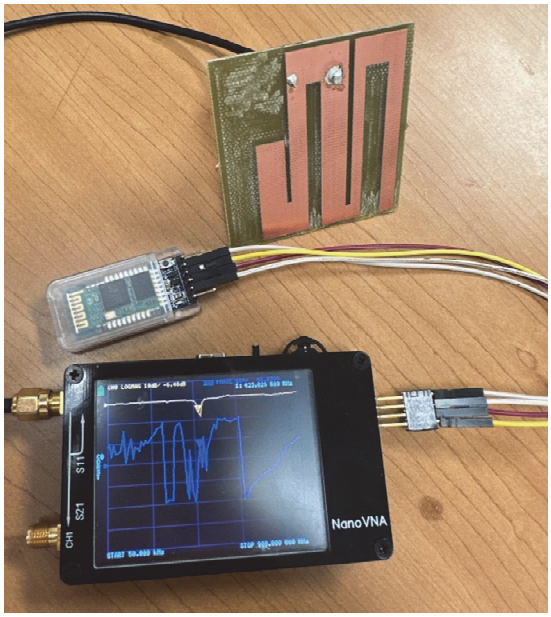

Fig. 2. NanoVNA attached to HC-05 Bluetooth module via UART connections and a sensor antenna.

C. Software configuration

To capture and visualize the data wirelessly transmitted by the NanoVNA-H, a MATLAB script was developed and is listed in [13]. This script interfaces with the Bluetooth module to receive data, applies necessary calibrations, and plots the S-parameters for real-time analysis. The use of MATLAB provided robust data manipulation and visualization capabilities, essential for interpreting the RF characteristics related to lactate concentration.

A Python library was also developed to interface the NanoVNA-H to a host computer, allowing devices without MATLAB to perform the same functions [13]. It allows users to control the NanoVNA, acquire S-parameters data, and process this data for RF analysis.

D. Measurement saving and transfer

The wireless communication setup was tested in various scenarios to ensure stability and accuracy. The tests would involve remote monitoring of lactate concentrations using resonator circuits attached to the human body. Figure 3 represents an example resonator used to take microfluidic lactate samples. The wireless NanoVNA-H proved to be a valuable tool for dynamic testing environments where conventional VNAs are unsuitable due to size and the necessity of a physical connection.

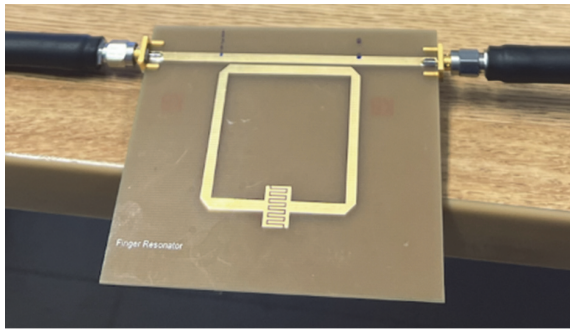

Fig. 3. Finger resonator setup used for microfluidic measurements that mimic lactate concentrations.

In this experiment, the NanoVNA-H was connected via Bluetooth to a computer running the NanoVNA Saver application, which is available as an open-source application on GitHub [14]. This setup allowed for convenient and wireless data acquisition from the NanoVNA-H, streamlining the measurement process and enhancing mobility. The control panel for the application is shown in Fig. 4. The measurement results downloaded from NanoVNA Saver are shown in Fig. 5. The Smith chart, log magnitude, and other relevant plots were generated in NanoVNA Saver, enabling detailed examination of the DUT characteristics.

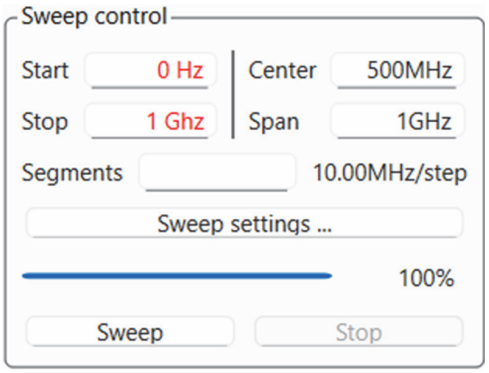

Fig. 4. NanoVNA Saver sweep control interface.

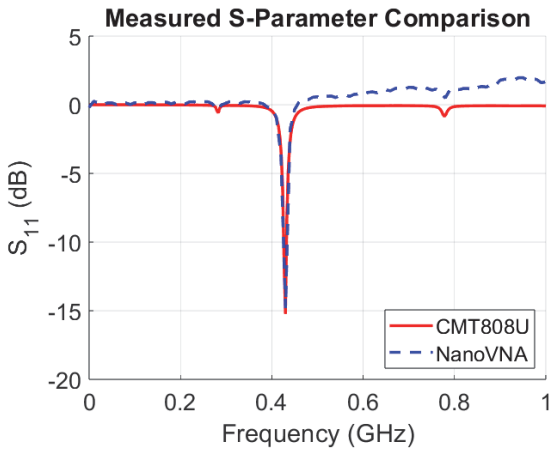

Fig. 5. Comparison of measured S-parameters from CMT808U laboratory VNA (calibrated) and NanoVNA (uncalibrated) for the sensor antenna shown in Fig. 2.

Shown in Fig. 5 are S-parameter measurements for an on-body glucose-sensing antenna developed by Ostrem, Kringlen, and Evanovich in free space [15]. For comparison, the same antenna is measured on a CMT-808U laboratory VNA, calibrated on Port 1 using an S2611 Calibration Kit. The antenna measurements were initially taken in free space in the range 0-1 GHz, providing baseline S-parameter data for comparison.

For this antenna, the NanoVNA-H measured the resonance of the antenna around 430 MHz to an accuracy <1 MHz. The magnitude of the reflection coefficient is within 1 dB at the same measured frequency. It should be noted that measurements taken on the NanoVNA express a reflection coefficient >0 dB even though the device measured is passive. This is because the NanoVNA cannot transmit calibrated measurements over UART. In applications where calibration is necessary, measurements of a calibration kit may be taken by a user prior to use and have calibration applied through software after measurements are complete.

IV. WIRELESS COMMUNICATION INTERFACE WITH NANOVNA V2

Due to the hardware differences from the NanoVNA-H, the NanoVNA v2 does not provide a hardware UART port that can be used to interface the NanoVNA directly to a computer via a USB-to-serial bridge. Instead, the module can only connect via USB, which establishes a virtual USB Communication Device Class (CDC) serial port between the NanoVNA and its host computer.

A. Hardware configuration

Hardware setup for the NanoVNA v2 is relatively simple. The DUT is connected to Port 1 (and Port 2, if applicable) via a coaxial cable as shown in Figs. 6 and 7. The NanoVNA is then connected via USB to a host computer. In this paper, the NanoVNA was connected to a host laptop running Windows 10. A smaller, portable device such as a Raspberry Pi may be used in lieu of the laptop to allow all hardware to be attached to a person, and standard communication protocols such as WiFi or Bluetooth may be used to transfer data wirelessly.

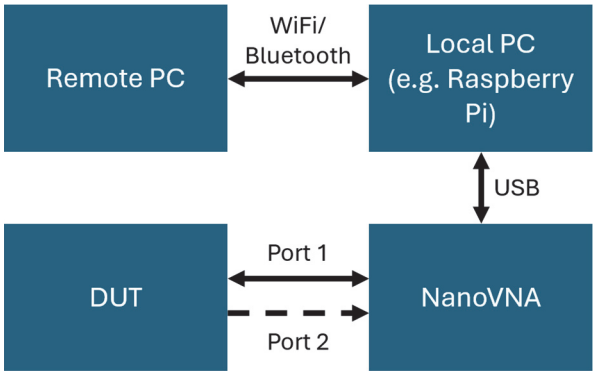

Fig. 6. Connection diagram of NanoVNA v2 for remote measurement.

B. Software configuration

Using the USB data interface specification from the NanoRFE NanoVNA v2 Manual and example firmware provided on the NanoVNA v2 GitHub repository [16], a Python library was developed to simplify interfacing of the NanoVNA v2 with a host computer [13]. This Python library uses the pySerial library for serial interfacing so that the source code is compatible with Windows, Linux, or MacOS.

Due to firmware limitations, some sweep settings of the NanoVNA v2 may yield bad measurement results. For example, it was found that the number of sweep points must be a power of 2 if more than 256 samples are being requested from the NanoVNA. Otherwise, some repeated data will be sent from the NanoVNA v2.

Fig. 7. Test configuration of the sensor antenna using NanoVNA v2 and a host computer.

C. Measurement saving and transfer

Using the software developed to interface with the NanoVNA v2, a sweep of S_{11} of the attached antenna was measured and plotted as shown in Fig. 7. The developed software is also able to export the measured parameters to a touchstone file, which may then be imported into software such as MATLAB for further analysis. Files can be retrieved from the host computer to other remote computers using protocols like SCP or SFTP. The same experiment using the sensor antenna developed by Collin Kringlen was used to examine the measurement accuracy of the NanoVNA v2 when connected remotely.

When examining the major resonance of the antenna at 2.1 GHz, the NanoVNA has a measurement accuracy of within 10 MHz. It does not, however, measure the magnitude of the S-parameters well, displaying over 5 dB of difference when compared to the NanoVNA v2. This is an expected tradeoff given the price of the NanoVNA v2 compared to a professional VNA, though application where only a shift in resonant frequency is examined could greatly benefit from the size reduction in measurement hardware. This setup also suffers from the same calibration issues where it may report a reflection coefficient >0 dB for a passive device, though software libraries such as scikit-rf may be used to measure a calibration kit and apply the calibration to the measured data [17].

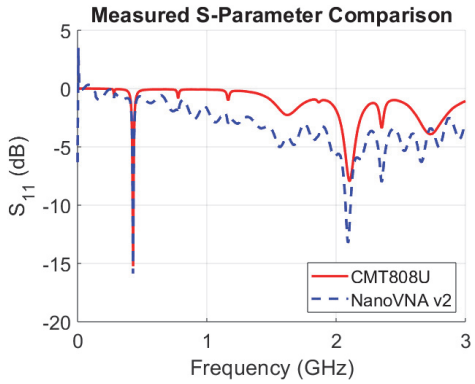

Fig. 8. S_{11} plot of measured antenna on NanoVNA v2 (uncalibrated) against Copper Mountain CMT808U (calibrated).

V. DISCUSSION

This paper proposes a simple system for making noninvasive on-body measurements of S-parameters with small-footprint, low-cost VNA technology. However, there are potential areas where the software developed can be further improved.

First, it should be noted that direct readings from the NanoVNA v2 do not reflect any calibration applied to the device, so calibration needs to be applied in the software on the host computer. This is evident in Fig. 8 where $S_{11} > 0$ dB at some points. Calibration can be done using a library such as scikit-rf [17] or by custom implementation, though it has yet to be implemented in the currently developed Python codebase.

The developed software may also be imported as a class into other Python modules, which can allow users to develop real-time streaming of S-parameters or data analysis. If good models are created that relate a shift in S_{11} or S_{21} to lactate concentrations, this would enable real-time on-body lactate monitoring.

VI. CONCLUSIONS

The integration of microwave sensor technology with wireless data interfaces in the NanoVNA-H and NanoVNA v2 paves the way for a new era in biomedical sensing. This research not only contributes to the field of biomedical engineering but also sets a precedent for future innovations in portable measurement technologies.

Through the use of a NanoVNA, this study has demonstrated the feasibility of remote lactate sensing, which has significant implications for healthcare and athletic performance monitoring. The successful interfacing of the NanoVNA-H with Bluetooth communication modules and the development of accompanying software in MATLAB and Python highlights the potential for creating a user-friendly, cost-effective, and portable solution for real-time lactate monitoring. Although an additional single-board computer or similar device is needed to enable similar functionality on the NanoVNA v2, the ability to wirelessly interface with it provides additional opportunities that the NanoVNA does not provide, especially enabling measurement of S-parameters in the 900 MHz to 3 GHz range.

REFERENCES

[1] F. Alam, S. RoyChoudhury, A. H. Jalal, Y. Umasankar, S. Forouzanfar, N. Akter, S. Bhansali, and N. Pala, "Lactate biosensing: The emerging point-of-care and personal health monitoring," *Biosensors and Bioelectronics*, vol. 117, pp. 818–829, Oct. 2018.

[2] M. Baghelani, Z. Abbasi, M. Daneshmand, and P. E. Light, "Non-invasive lactate monitoring system using wearable chipless microwave sensors with enhanced sensitivity and zero power consumption," *IEEE Transactions on Biomedical Engineering*, vol. 69, no. 10, pp. 3175–3182, Oct. 2022.

[3] A. Mason, O. Korostynska, J. Louis, L. E. Cordova-Lopez, B. Abdullah, J. Greene, R. Connell, and J. Hopkins, "Noninvasive in-situ measurement of blood lactate using microwave sensors," *IEEE Transactions on Biomedical Engineering*, vol. 65, no. 3, pp. 698–705, Mar. 2018.

[4] T. Reinecke, J.-G. Walter, T. Kobelt, A. Ahrens, T. Scheper, and S. Zimmermann, "Design and evaluation of split-ring resonators for aptamer-based biosensors," *Journal of Sensors and Sensor Systems*, vol. 7, no. 1, pp. 101–111, Feb. 2018.

[5] A. Mason, O. Korostynska, M. Ortoneda-Pedrola, A. Shaw, and A. Al-Shamma'a, "A resonant co-planar sensor at microwave frequencies for biomedical applications," *Sensors and Actuators A: Physical*, vol. 202, pp. 170–175, Nov. 2013.

[6] Keysight, *FieldFox Handheld RF and Microwave Analyzers* [Online]. Available: https://www.keysight.com/us/en/products/network-analyzers/fieldfox-handheld-rf-microwave-analyzers.html.

[7] About NanoVNA, *NanoVNA |Very tiny handheld Vector Network Analyzer*. [Online]. Available: https://nanovna.com.

[8] About NanoVNA, *NanoVNA v2 Official Site* [Online]. Available: https://nanorfe.com/nanovna-v2.html.

[9] L. Rothman, *NanoVNA Console Commands* [Online]. Available: https://4ham.ru/wp-content/uploads/2020/05/NanoVNA_Console_Commands_Dec-9-19-1.pdf.

[10] NanoVNA Hardware [Online]. Available: https://oristopo.github.io/nVhelp/html/hardware.htm.

[11] User Manual - NanoVNA V2, *NanoVNA V2 Official Site* [Online]. Available: https://nanorfe.com/nanovna-v2-user-manual.html#specifications.

[12] Firmware with UART support for nanoVNA-H [Online]. Available: https://github.com/DaveLapp/NanoVNA-H/releases/tag/shell-on-UART-HugenJan2020.

[13] K. Y. Hora, L. K. Elmiladi, A. Z. Elsherbeni, and P. H. Aaen, *Nano VNA Remote Communication of S-Parameters* [Online]. Available: https://aces-society.org/software/freeware/NanoVNA_Code_Appendix_LisaElmiladi.zip.

[14] NanoVNA-Saver/nanovna-saver [Online]. Available: https://github.com/NanoVNA-Saver/nanovna-saver/releases.

[15] S. Ostrem, C. Kringlen, C. Evanovich, A. Elsherbeni, and P. Aaen, "Towards the design of a non-invasive glucose monitoring sensor," in *2024 International Applied Computational Electromagnetics Society (ACES) Symposium*, pp. 1–2, May 2024.

[16] nanovna-v2/NanoVNA2-firmware [Online]. Available: https://github.com/nanovna-v2/NanoVNA2-firmware.

[17] A. Arsenovic, J. Hillairet, J. Anderson, H. Forstén, V. Rieß, M. Eller, N. Sauber, R. Weikle, W. Barnhart, and F. Forstmayr, "scikit-rf: An Open-Source Python Package for Microwave Network Creation, Analysis, and Calibration [Speaker's Corner]," *IEEE Microwave Magazine*, vol. 23, no. 1, pp. 98–105, Jan. 2022.

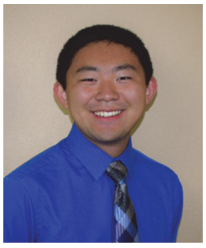

Kenneth Y. Hora received his B.S. in Electrical Engineering in 2025 with minors in Computer Engineering and Public Affairs at the Colorado School of Mines in Golden, CO, USA. He is continuing his education at Mines, pursuing an M.S. in Electrical Engineering. His research interests include microprocessor VLSI design, embedded systems, antennas, and electromagnetic simulation.

Lisa Elmiladi received her B.S. and M.S. in Electrical Engineering in 2024 and 2025, respectively, from the Colorado School of Mines in Golden, CO, USA, completing both degrees with distinction. Her research interests include VLSI circuit design, biomedical devices, antennas, computer architecture, and electromagnetics. With a keen interest in the practical and theoretical aspects of her field, Elmiladi is intent on furthering her education with a Ph.D. in Electrical Engineering.

Atef Z. Elsherbeni received his Ph.D. in Electrical Engineering from Manitoba University, Winnipeg, Manitoba, Canada, in 1987. He started his engineering career as a part-time Software and System Design Engineer from March 1980 to December 1982 at the Automated Data System Center, Cairo, Egypt. From January to August 1987, he was a Post-Doctoral Fellow at Manitoba University. Elsherbeni joined the faculty at the University of Mississippi in August 1987 as an Assistant Professor of Electrical Engineering and progressed to the full professor and the Associate Dean of the College of Engineering for Research and Graduate Programs. He joined the Electrical Engineering and Computer Science (EECS) Department at Colorado School of Mines in August 2013. Elsherbeni is an IEEE Life Fellow and ACES Fellow. He is the Editor-in-Chief for *Applied Computational Electromagnetics Society (ACES) Journal*, and a past Associate Editor to *Radio Science*. He was Chair of the Engineering and Physics Division of the Mississippi Academy of Science, Chair of the Educational Activity Committee for IEEE Region 3 Section, and past President of ACES Society. He recently received the 2023 IEEE APS Harington-Mittra Award for his contribution to computational electromagnetics with hardware acceleration and the ACES 2025 Computational Electromagnetics Award.

Peter H. Aaen received the B.A.Sc. degree in engineering science and the M.A.Sc. degree in electrical engineering from the University of Toronto, Toronto, ON, Canada, in 1995 and 1997, respectively, and the Ph.D. degree in electrical engineering from Arizona State University, Tempe, AZ, USA, in 2005. He was the Manager of the RF Division, RF Modeling and Measurement Technology Team, Freescale Semiconductor, Inc., Tempe, AZ, USA, a company which he joined in 1997, then the Semiconductor Product Sector, Motorola Inc. In 2013, he joined the Faculty of Engineering and Physical Sciences, University of Surrey, Guildford, UK, where he was a Reader of microwave semiconductor device modeling. He was also the Director of the Nonlinear Microwave Measurement and Modeling

Laboratory, a joint University of Surrey/National Physical Laboratory, and the Director of National Physical Laboratory – South of England, Guildford UK. In 2019, he joined the Colorado School of Mines as a Professor and Head of the Electrical Engineering Department. He co-authored *Modeling and Characterization of RF and Microwave Power FETs* (Cambridge University Press, 2007). Aaen is a member of the Microwave Theory and Techniques and Electron Device Societies, served as an Executive Committee Member and Vice-President of the Automatic RF Techniques Group, and was the Chair of the IEEE Technical Committee (MTT-1) on Computer-Aided Design.

High-Frequency Performance Analysis and Verification of Twinax Cable Structures

Wei-Hsiu Tsai[1], Ding-Bing Lin[1], Cheng-Hsun Ho[1], and Tzu-Fang Tseng[2]

[1]Department of Electronic and Computer Engineering
National Taiwan University of Science and Technology, Taipei 10607, Taiwan
D10802006@mail.ntust.edu.tw, dblin@mail.ntust.edu.tw, M11002248@gapps.ntust.edu.tw

[2]Department of CTO Office
BizLink International Corporation, New Taipei 23533, Taiwan
tzufang_tseng@optiworks.com

Abstract – The most commonly used cables in device-to-device communication, such as USB, HDMI, DP, or PCI-e cables, as well as the MCIO cables currently used in artificial intelligence (AI) servers, has a differential Twinax configuration. The use of differential transmission aims to mitigate the impact of external interference. The Twinax structure consisted of a twin-core cable with an outer copper foil shielding. Achieving perfect symmetry in the Twinax cable is a challenge. This work investigated whether the asymmetrical structure and material impacted the production yield rate. The focus was on the mixed-mode analysis of the asymmetric Twinax cable. By utilizing mixed-mode S-parameters, we aimed to determine whether the cable designs met industry standards and complied with data rate requirements. Due to intense market competition and short development cycles, 3D full-wave simulations were time-consuming because of the high mesh count. Moreover, modeling was challenging because the center of each segment of an actual cable underwent slight variations. To expedite the design process, a method was developed to extract Twinax cable RLGC (Resistance, Inductance, Conductance, Capacitance) parameters, calculate mixed-mode S-parameters, and perform analysis and evaluations. Our approach not only enables efficient signal quality assessment across cables of varying lengths by simply connecting each small segment to account for continuous manufacturing variations but also significantly reduces product development time to under one hour. Furthermore, this work investigated the impact of common manufacturing imperfections, ensuring robust and reliable designs for real-world applications.

Index Terms – Mixed-mode scattering parameters, RLGC parameters, transmission line analysis, Twinax cable, vector network analyzers.

I. INTRODUCTION

Whether it is 5G/6G, artificial intelligence (AI), high-performance cloud computing (HPC) systems, or quantum computing, future technologies all involve handling vast amounts of data and information. The demand for data rates continuously increases, and interface components for transmitting and receiving data face numerous challenges in maintaining signal integrity during high-speed transmissions. The Peripheral Component Interconnect Express (PCIe) interface standard is the most common in high-performance computing systems and data centers [1]. Since PCI-SIG introduced PCIe 1.0 in 2003, it has evolved continually, with the PCIe 6.0 standard released in 2021, boosting transmission capability from 2.5 GT/s to 64 GT/s. Increasing the frequency enables support for higher data rates. For high-speed digital signals, differential transmission with Twinax cables is commonly used because it effectively eliminates external noise.

The production process involves two methods: separate extrusion [2] as shown in Fig. 1 (a) and co-extrusion [3] as shown in Fig. 1 (b). The separate extrusion structure is inhomogeneous due to air gaps between the shielding and the dielectric insulator, resulting in an inhomogeneous dielectric in copper Twinax cables. The time domain time skew in Twinax cables is typically used as an indicator for testing the signal integrity (SI) performance of the cables [4]. However, time skew cannot accurately reflect the performance of the product in actual applications, as delay decreases at higher frequencies [5].

Moreover, compared to co-extruded cables, separately extruded cables typically have lower manufacturing costs but are believed to have greater skew-induced differential insertion loss resonance [6]. Time skew causes differential insertion loss to resonate at a frequency equal to 1/(2-time skew) [7], thereby

Submitted On: July 14, 2025
Accepted On: September 30, 2025

https://doi.org/10.13052/2025.ACES.J.401110

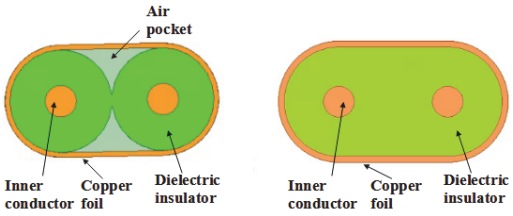

(a) (b)

Fig. 1. Cross-section of Twinax cables. (a) Separately extruded cable. (b) Co-extruded cable.

minimizing unnecessary resonance in differential insertion loss at operating frequencies under lower time skew. Contrary to common belief, in separately extruded cables, dielectric non-uniformity helps reduce skew caused by structural asymmetry at high frequencies and eliminates the resonance due to differential insertion loss skew.

Studies indicate that dielectric non-uniformity could cause modulation behavior in scattering parameters (S-parameters) [8]. This phenomenon is like microstrip lines [9], where the phase velocity of odd and even modes varied due to dielectric non-uniformity [10]. Dielectric non-uniformity also causes relatively minor changes in capacitance [11], leading to modulation between propagation constants and significantly altering S-parameters [12]. Since the changes in the capacitance matrix are relatively minor, this variation was generally referred to as capacitance disturbance.

Non-uniformity and asymmetry are considered disturbances to the RLGC parameters, preventing accurate signal level interpretation and increasing bit error rates (BER) [13]. Furthermore, the characteristic modes of asymmetric coupled transmission lines are not limited to odd or even modes, necessitating transformations for the required mixed-mode S-parameter analysis.

In practice, analyzing the impact of dielectric non-uniformity and asymmetry on the signal integrity performance of Twinax cables, analytical equations for calculating S-parameters based on RLGC parameters can be derived. Calculating S-parameters from the RLGC parameters of multi-conductor transmission lines typically requires computing the hyperbolic function of matrices [14]. The hyperbolic matrix function can be calculated through infinite series summation, which increases the complexity of perturbation analysis [15]. Therefore, perturbation analysis based on solving eigenvalues and eigenvectors was proposed [16]. S-parameters can be calculated based on elements of the RLGC parameters without needing to compute matrix hyperbolic functions or any other infinite series. This assumes the cables are ideal transmission lines, with no variation along the transmission direction.

Our method employs an Ansys 2D extractor to extract S-parameters and derive R, L, G, and C parameters. We performed measurements on PCIe Twinax cables comparing the measurement results with the mathematical calculations. The results validated the accuracy of the mathematical calculation method, which could be applied to cable design. Additionally, because the concept was applicable to microstrip lines, the calculation method could be extended to printed circuit board assembly (PCBA) design.

There is already substantial research on symmetric transmission lines, but studies on asymmetric transmission lines only saw theoretical analysis starting in the 1990s [17, 18]. Research in this area is categorized under multiconductor transmission lines, primarily focusing on those based on conductive substrates. By measuring the S-parameters and applying curve fitting, the RLGC parameters of the transmission lines are obtained. It is important to note that this analysis needed to ignore the effects of other higher-order modes; otherwise, the extracted RLGC parameters will have significant errors.

This work is an extension of [19], providing a more comprehensive description of the structure, materials, and methods for actual cable measurements. In section II, we present a method to calculate the R, L, G, C, and asymmetric S-parameters of coupled transmission lines. Section III simulates and calculates the S-parameters for four different Twinax cable scenarios when non-ideal conditions are considered, discussing whether the mixed-mode S-parameters meet industry standards. In section IV, we compare the measured S-parameters of Twinax cables produced with the calculated results to confirm their consistency. In section V, we conclude the paper.

II. CALCULATING R, L, G, C, AND S-PARAMETERS FOR TWINAX CABLE

A. Transmission line theory analysis for Twinax cable

The coupled two-dimensional transmission line model assumes that the two wires are symmetrical, as shown in Fig. 2. This structure ignores the influence of higher-order modes and assumes that the voltage propagation direction is along the x-axis. The magnetic field generated by the current in the first wire divides the interior of the wire into infinitely many concentric circles with negligible thickness. Each circle experiences different magnetic flux, resulting in varying eddy current strengths, with the strongest eddy currents near the center. Consequently, the current tends to concentrate on the surface of the wire. The proximity effect is caused by the eddy currents induced within the second wire, which resist changes in magnetic flux generated by the current in the first wire. Because the magnetic field strength is

inversely proportional to the distance from the first wire, the magnetic field is stronger in areas of the second wire closer to the first wire, leading to larger opposing eddy currents. Conversely, areas of the second wire closer to the surrounding ground experience weaker magnetic fields, resulting in smaller opposing eddy currents.

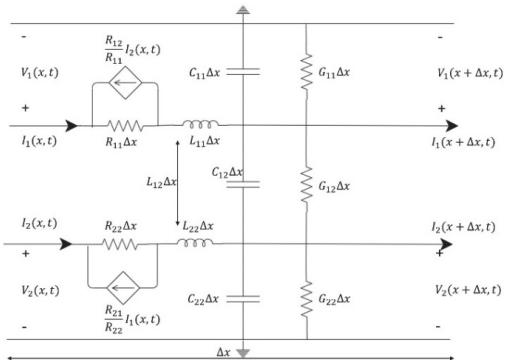

Fig. 2. Equivalent circuit of two-dimensional transmission line.

The two-dimensional transmission line can be expressed as:

$$-\frac{dv_1}{d_x} = Z_{11}i_1 + Z_{12}i_2, \tag{1}$$

$$-\frac{dv_2}{d_x} = Z_{22}i_2 + Z_{12}i_1, \tag{2}$$

$$-\frac{di_1}{d_x} = Y_{11}v_1 + Y_{12}v_2, \tag{3}$$

$$-\frac{di_2}{d_x} = Y_{22}v_2 + Y_{12}v_1. \tag{4}$$

Where:

$$\begin{aligned} Z_{11} &= R_{11} + j\omega L_{11}, \\ Z_{12} &= R_{12} + j\omega L_{12}, \\ Z_{21} &= R_{21} + j\omega L_{21}, \\ Z_{22} &= R_{22} + j\omega L_{22}, \\ Y_{11} &= G_{11} + G_{12} + j\omega(C_{11} + C_{12}), \\ Y_{12} &= G_{12} + j\omega C_{12}, \\ Y_{21} &= G_{21} + j\omega C_{21}, \\ Y_{22} &= G_{22} + G_{12} + j\omega(C_{22} + C_{12}). \end{aligned}$$

Z_{11} is the series impedance of the first wire, Z_{22} is the series impedance of the second wire, Z_{12} (or Z_{21}) is the mutual impedance between them, Y_{11} is the shunt admittance of the first wire, Y_{22} is the shunt admittance of the second wire, Y_{12} (or Y_{21}) is the mutual admittance between them, L_{11} is the self-inductance of the first wire, L_{21} is the mutual inductance of the second wire, C_{11} is the self-capacitance of the first wire, C_{12} is the mutual capacitance between the two wires, R_{21} is the AC resistance of the first wire, R_{12} is the mutual resistance within the second wire, G_{11} is the self-conductance of the first wire, G_{12} is the mutual conductance between the two wires.

By substituting (3) into (1) and (2), and (4) into (1) and (2), the voltage propagation equations are derived. Observing equations (5) and (6) as a system of coupled differential equations, it is challenging to solve for the voltage propagation behavior of v_1 and v_2 in this scenario. Therefore, the application of eigenvalue decomposition is necessary. The procedure involves representing (5) and (6) as matrix equations, as shown in (7). Decomposing the 2x2 matrix in (7) into eigenvalues λ_1 and λ_2 with corresponding eigenvectors e_1 and e_2, considering the infinite solutions for eigenvectors, set x_1 and x_3 as 1. Proceed with the calculations:

$$\frac{d^2v_1}{dx^2} = a_1v_1 + b_1v_2, \tag{5}$$

$$\frac{d^2v_2}{dx^2} = a_2v_2 + b_2v_1, \tag{6}$$

$$\frac{d^2}{dx^2}\begin{bmatrix} v_1 \\ v_2 \end{bmatrix} = \begin{bmatrix} a_1 & b_1 \\ b_2 & a_2 \end{bmatrix}\begin{bmatrix} v_1 \\ v_2 \end{bmatrix}, \tag{7}$$

$$\begin{bmatrix} a_1 & b_1 \\ b_2 & a_2 \end{bmatrix}\begin{bmatrix} x_1 \\ x_2 \end{bmatrix} = \lambda_1\begin{bmatrix} x_1 \\ x_2 \end{bmatrix}, \tag{8}$$

$$\begin{bmatrix} a_1 & b_1 \\ b_2 & a_2 \end{bmatrix}\begin{bmatrix} x_3 \\ x_4 \end{bmatrix} = \lambda_2\begin{bmatrix} x_3 \\ x_4 \end{bmatrix}. \tag{9}$$

Taking (10) into (7) yields (A). Next, by differentiating as a linear operator, the differential operator can be factored out, resulting in (A). Let $\begin{bmatrix}\overrightarrow{e_1} & \overrightarrow{e_2}\end{bmatrix}^T\begin{bmatrix} v_1 \\ v_2 \end{bmatrix}$ be a new variable representing $\begin{bmatrix} v_c \\ v_\pi \end{bmatrix}$, leading to a decoupled system of simultaneous differential equations. Finally, after solving for v_c and v_π, substituting back into $\begin{bmatrix} v_c \\ v_\pi \end{bmatrix}\begin{bmatrix}\overrightarrow{e_1} & \overrightarrow{e_2}\end{bmatrix}^T\begin{bmatrix} v_1 \\ v_2 \end{bmatrix}$ yields the propagation equations for v_1 and v_2 in (17) and (A). As for the current propagation behavior of i_1 and i_2, substituting v_1 and v_2 back into (3) and (4) provides the expressions for i_1 and i_2 in (A) and (A). C and π represent characteristic orthogonal basis modes for asymmetric transmission lines, analogous to even and odd modes for symmetric transmission lines, differing only in symbol representation. Here, x_2 and x_4 denote the ratio of v_1 and v_2 under C and π mode scenarios:

$$\begin{bmatrix} a_1 & b_1 \\ b_2 & a_2 \end{bmatrix} = \begin{bmatrix}\overrightarrow{e_1} & \overrightarrow{e_2}\end{bmatrix}\begin{bmatrix} \lambda_1 & 0 \\ 0 & \lambda_2 \end{bmatrix}\begin{bmatrix}\overrightarrow{e_1} & \overrightarrow{e_2}\end{bmatrix}^{-1}, \tag{10}$$

$$\frac{d^2}{dx^2}\begin{bmatrix}v_1\\v_2\end{bmatrix}=\begin{bmatrix}\overrightarrow{e_1} & \overrightarrow{e_2}\end{bmatrix}\begin{bmatrix}\lambda_1 & 0\\0 & \lambda_2\end{bmatrix}\begin{bmatrix}\overrightarrow{e_1} & \overrightarrow{e_2}\end{bmatrix}^{-1}\begin{bmatrix}v_1\\v_2\end{bmatrix}, \tag{11}$$

$$\begin{bmatrix}\overrightarrow{e_1} & \overrightarrow{e_2}\end{bmatrix}^{-1}\frac{d^2}{dx^2}\begin{bmatrix}v_1\\v_2\end{bmatrix}=\begin{bmatrix}\lambda_1 & 0\\0 & \lambda_2\end{bmatrix}\begin{bmatrix}\overrightarrow{e_1} & \overrightarrow{e_2}\end{bmatrix}^{-1}\begin{bmatrix}v_1\\v_2\end{bmatrix}, \tag{12}$$

$$\frac{d^2}{dx^2}\begin{bmatrix}\overrightarrow{e_1} & \overrightarrow{e_2}\end{bmatrix}^{-1}\begin{bmatrix}v_1\\v_2\end{bmatrix}=\begin{bmatrix}\lambda_1 & 0\\0 & \lambda_2\end{bmatrix}\begin{bmatrix}\overrightarrow{e_1} & \overrightarrow{e_2}\end{bmatrix}^{-1}\begin{bmatrix}v_1\\v_2\end{bmatrix}, \tag{13}$$

$$\frac{d^2}{dx^2}\begin{bmatrix}v_c\\v_\pi\end{bmatrix}=\begin{bmatrix}\lambda_1 & 0\\0 & \lambda_2\end{bmatrix}\begin{bmatrix}v_c\\v_\pi\end{bmatrix}, \tag{14}$$

$$\frac{d^2v_c}{dx^2}=\lambda_1 v_c, \tag{15}$$

$$\frac{d^2v_\pi}{dx^2}=\lambda_2 v_\pi, \tag{16}$$

$$v_1=A_1e^{-\sqrt{\lambda_1}x}+A_2e^{-\sqrt{\lambda_1}x}+A_3e^{-\sqrt{\lambda_2}x}+A_4e^{-\sqrt{\lambda_2}x}, \tag{17}$$

$$v_2=A_1x_2e^{-\sqrt{\lambda_1}x}+A_2x_2e^{-\sqrt{\lambda_1}x}+A_3x_4e^{-\sqrt{\lambda_2}x}+A_4x_4e^{-\sqrt{\lambda_2}x}, \tag{18}$$

$$i_1=A_1Y_{c1}e^{-\sqrt{\lambda_1}x}+A_2xY_{c1}e^{-\sqrt{\lambda_1}x}+A_3xY_{\pi1}e^{-\sqrt{\lambda_2}x}+A_4Y_{\pi1}e^{-\sqrt{\lambda_2}x}, \tag{19}$$

$$i_2=A_1x_2Y_{c2}e^{-\sqrt{\lambda_1}x}+A_2x_2Y_{c2}e^{-\sqrt{\lambda_1}x}+A_3x_4Y_{\pi2}e^{-\sqrt{\lambda_2}x}+A_4x_4Y_{\pi2}e^{-\sqrt{\lambda_2}x}. \tag{20}$$

Here $\sqrt{\lambda_1}$ and $\sqrt{\lambda_2}$ represent the propagation constants for the c and π modes, respectively, and $Y_{c2}, Y_{c1}, Y_{\pi2}$, and $Y_{\pi1}$ denote the characteristic admittances for the second and first wires of the C and π modes, respectively.

For C mode:

$$\frac{i_2}{i_1}=\frac{1}{R_\pi},\quad \frac{v_2}{v_1}=R_c,$$

$$-\frac{dv_1}{d_x}=Z_{11}i_1+Z_{12}\frac{1}{R_\pi}i_1,\quad -\frac{di_1}{d_x}=Y_{11}v_1+Y_{12}R_cv_1,$$

$$Z_{c1}=\sqrt{\frac{R_{11}-\frac{R_{12}}{R_\pi}+j\omega(L_{11}-\frac{L_{12}}{R_\pi})}{G_{11}+G_{12}-R_CG_{12}+j\omega(C_{11}+C_{12}-R_CC_{12})}}, \tag{21}$$

$$Z_{c2}=\sqrt{\frac{R_{22}-R_\pi R_{12}+j\omega(L_{22}-R_\pi L_{12})}{G_{22}+G_{12}-\frac{G_{12}}{R_C}+j\omega(C_{22}+C_{12}-\frac{C_{12}}{R_C})}}. \tag{22}$$

For π mode:

$$\frac{i_2}{i_1}=\frac{1}{R_c},\quad \frac{v_2}{v_1}=R_\pi,$$

$$-\frac{dv_1}{d_x}=Z_{11}i_1+Z_{12}\frac{1}{R_c}i_1,\quad -\frac{di_1}{d_x}=Y_{11}v_1+Y_{12}R_\pi v_1,$$

$$Z_{\pi1}=\sqrt{\frac{R_{11}-\frac{R_{12}}{R_C}+j\omega(L_{11}-\frac{L_{12}}{R_C})}{G_{11}+G_{12}-R_\pi G_{12}+j\omega(C_{11}+C_{12}-R_\pi C_{12})}}, \tag{23}$$

$$Z_{\pi2}=\sqrt{\frac{R_{22}-R_CR_{12}+j\omega(L_{22}-R_CL_{12})}{G_{22}+G_{12}-\frac{G_{12}}{R_\pi}+j\omega(C_{22}+C_{12}-\frac{C_{12}}{R_\pi})}}. \tag{24}$$

The RLGC parameters of the asymmetric line can be calculated from the C mode (21) and (22) and π mode (23) and (24) equations, yielding expressions (25)–(45):

$$\gamma_c=\sqrt{\left(R_{11}-\frac{R_{12}}{R_\pi}+j\omega\left(L_{11}-\frac{L_{12}}{R_\pi}\right)\right)*(G_{11}+G_{12}-R_CG_{12}+j\omega(C_{11}+C_{12}-R_CC_{12}))}, \tag{25}$$

$$\gamma_\pi=\sqrt{\left(R_{11}-\frac{R_{12}}{R_C}+j\omega\left(L_{11}-\frac{L_{12}}{R_C}\right)\right)\times(G_{11}+G_{12}-R_\pi G_{12}+j\omega(C_{11}+C_{12}-R_\pi C_{12}))}, \tag{26}$$

$$Z_{c1}*\gamma_C=R_{11}-\frac{R_{12}}{R_\pi}+j\omega\left(L_{11}-\frac{L_{12}}{R_\pi}\right), \tag{27}$$

$$Z_{\pi1}*\gamma_\pi=R_{11}-\frac{R_{12}}{R_C}+j\omega\left(L_{11}-\frac{L_{12}}{R_C}\right), \tag{28}$$

$$Z_{c2}*\gamma_C=R_{22}-R_\pi R_{12}+j\omega\left(L_{22}-R_\pi L_{12}\right), \tag{29}$$

$$Z_{\pi2}*\gamma_\pi=R_{22}-R_CR_{12}+j\omega\left(L_{22}-R_CL_{12}\right), \tag{30}$$

$$\gamma_C/Z_{c1}=G_{11}+G_{12}-R_CG_m+j\omega(C_{11}+C_{12}-R_CC_{12}), \tag{31}$$

$$\gamma_\pi/Z_{\pi1}=G_{11}+G_{12}-R_\pi G_{12}+j\omega(C_{11}+C_{12}-R_\pi C_{12}), \tag{32}$$

$$\gamma_C/Z_{c2}=G_{22}+G_{12}-\frac{G_{12}}{R_C}+j\omega\left(C_{22}+C_{12}-\frac{C_{12}}{R_C}\right), \tag{33}$$

$$\gamma_\pi/Z_{\pi2}=G_{22}+G_{12}-\frac{G_{12}}{R_\pi}+j\omega\left(C_{22}+C_{12}-\frac{C_{12}}{R_\pi}\right). \tag{34}$$

The simultaneous equations (27) to (34) can be used to derive the values of (35) to (45):

$$R_{11} = Re\left(\frac{(R_\pi Z_{c1}\gamma_c - R_c Z_{\pi 1}\gamma_\pi)}{R_c - R_\pi}\right), \quad (35)$$

$$R_{12} = Re\left(\frac{(Z_{c1}\gamma_c - Z_{\pi 1}\gamma_\pi)}{\frac{-1}{R_\pi} + R_c}\right), \quad (36)$$

$$R_{22} = Re\left(\frac{(R_c Z_{c2}\gamma_c - R_\pi Z_{\pi 2}\gamma_\pi)}{R_c - R_\pi}\right), \quad (37)$$

$$L_{11} = Im\left(\frac{(R_\pi Z_{c1}\gamma_c - R_c Z_{\pi 1}\gamma_\pi)}{(R_c - R_\pi)\omega}\right), \quad (38)$$

$$L_{12} = Im\left(\frac{(Z_{c1}\gamma_c - Z_{\pi 1}\gamma_\pi)}{\left(\frac{-1}{R_\pi} + R_c\right)\omega}\right), \quad (39)$$

$$L_{22} = Im\left(\frac{(R_c Z_{c2}\gamma_c - R_\pi Z_{\pi 2}\gamma_\pi)}{(R_c - R_\pi)\omega}\right), \quad (40)$$

$$C_{11} = Im\left(\frac{\left(\frac{\gamma_c}{Z_{c1}}(1-R_\pi) - \frac{\gamma_\pi}{Z_{\pi 1}}(1-R_c)\right)}{(R_c - R_\pi)\omega}\right), \quad (41)$$

$$C_{12} = Im\left(\frac{\left(\frac{\gamma_c}{Z_{c1}} - \frac{\gamma_\pi}{Z_{\pi 1}}\right)}{(R_c - R_\pi)\omega}\right), \quad (42)$$

$$C_{22} = Im\left(\frac{\left(\frac{\gamma_c}{Z_{c2}}\left(1-\frac{1}{R_\pi}\right) - \frac{\gamma_\pi}{Z_{\pi 2}}\left(1-\frac{1}{R_c}\right)\right)}{\left(\frac{1}{R_c} + \frac{-1}{R_\pi}\right)\omega}\right), \quad (43)$$

$$G_{11} = Re\left(\frac{\left(\frac{\gamma_c}{Z_{c1}}(1-R_\pi) - \frac{\gamma_\pi}{Z_{\pi 1}}(1-R_c)\right)}{(R_c - R_\pi)}\right), \quad (44)$$

$$G_{12} = Re\left(\frac{\left(\frac{\gamma_c}{Z_{c1}} - \frac{\gamma_\pi}{Z_{\pi 1}}\right)}{(R_c - R_\pi)}\right), \quad (45)$$

$$C_{22} = Re\left(\frac{\left(\frac{\gamma_c}{Z_{c2}}\left(1-\frac{1}{R_\pi}\right) - \frac{\gamma_\pi}{Z_{\pi 2}}\left(1-\frac{1}{R_c}\right)\right)}{\left(\frac{1}{R_c} + \frac{-1}{R_\pi}\right)}\right). \quad (46)$$

B. Extraction of S-parameters for asymmetric cables

Figure 3 depicts the model of an asymmetric transmission line. Coefficients for the C and π modes, as well as the transmission system's ABCD matrix, are given by (46), where S_{K11}, S_{K12}, S_{22}, and S_{21} are 2x2 matrices. $V_{p1} = \begin{bmatrix} v_a & v_b \end{bmatrix}^T$, $V_{p2} = \begin{bmatrix} v_c & v_d \end{bmatrix}^T$, $I_{p1} = \begin{bmatrix} I_a & I_b \end{bmatrix}^T$, $I_{p2} = \begin{bmatrix} I_c & I_d \end{bmatrix}^T$, $\overline{\overline{A}}, \overline{\overline{B}}, \overline{\overline{C}}$, and $\overline{\overline{D}}$ each represent 2x2 matrices.

Finally, the S-parameters for the asymmetric transmission line are obtained from the ABCD matrix. The

Fig. 3. Model of an asymmetric cable.

4-port network is simplified to a 2-port network through vector representation, with the matrices A, B, C, and D represented as:

$$\begin{bmatrix} v_{p1} \\ I_{p1} \end{bmatrix} = \begin{bmatrix} \overline{\overline{\mathrm{A}}} & \overline{\overline{\mathrm{B}}} \\ \overline{\overline{\mathrm{C}}} & \overline{\overline{\mathrm{D}}} \end{bmatrix} \begin{bmatrix} v_{p2} \\ -I_{p2} \end{bmatrix}, \quad (47)$$

$$[\overline{\overline{\mathrm{A}}}] = \frac{1}{R_\pi - R_c}\left\{ \begin{bmatrix} 1 & 1 \\ R_c & R_\pi \end{bmatrix} \begin{bmatrix} \cosh(\gamma_c l) & 0 \\ 0 & \cosh(\gamma_\pi l) \end{bmatrix} \times \begin{bmatrix} R_\pi & -1 \\ -R_c & 1 \end{bmatrix} \right\}, \quad (48)$$

$$[\overline{\overline{\mathrm{B}}}] = \frac{1}{R_\pi - R_c} \times \left\{ \left(\begin{bmatrix} Z_{c1} & Z_{\pi 1} \\ Z_{c2} & Z_{\pi 2} \end{bmatrix} * \begin{bmatrix} R_\pi & -R_c \\ -1 & 1 \end{bmatrix} \right) \times \begin{bmatrix} \sinh(\gamma_c l) & 0 \\ 0 & \sinh(\gamma_\pi l) \end{bmatrix} \begin{bmatrix} 1 & R_c \\ 1 & R_\pi \end{bmatrix} \right\}, \quad (49)$$

$$[\overline{\overline{\mathrm{C}}}] = \frac{1}{R_\pi - R_c}\left\{ \left(\begin{bmatrix} \frac{1}{Z_{c1}} & \frac{1}{Z_{\pi 1}} \\ \frac{1}{Z_{c2}} & \frac{1}{Z_{\pi 1}} \end{bmatrix} * \begin{bmatrix} 1 & 1 \\ R_c & R_\pi \end{bmatrix} \right) \begin{bmatrix} \sinh(\gamma_c l) & 0 \\ 0 & \sinh(\gamma_\pi l) \end{bmatrix} \begin{bmatrix} R_\pi & -1 \\ -R_c & 1 \end{bmatrix} \right\}, \quad (50)$$

$$[\overline{\overline{\mathrm{D}}}] = \frac{1}{R_\pi - R_c}\left\{ \begin{bmatrix} R_\pi & -R_c \\ -1 & 1 \end{bmatrix} \times \begin{bmatrix} \cosh(\gamma_c l) & 0 \\ 0 & \cosh(\gamma_\pi l) \end{bmatrix} \begin{bmatrix} 1 & R_c \\ 1 & R_\pi \end{bmatrix} \right\}. \quad (51)$$

The relationship between the ABCD matrix and S-parameters is:

$$\begin{bmatrix} \overline{\overline{\mathrm{A}}} & \overline{\overline{\mathrm{B}}} \\ \overline{\overline{\mathrm{C}}} & \overline{\overline{\mathrm{D}}} \end{bmatrix} = \begin{bmatrix} \overline{\overline{l}} - \overline{\overline{s_{k11}}} & -Z_0\left(\overline{\overline{l}} + \overline{\overline{S_{k11}}}\right) \\ \overline{\overline{S_{k21}}} & Z_0\overline{\overline{S_{k21}}} \end{bmatrix}^{-1} \times \begin{bmatrix} \overline{\overline{S_{k12}}} & -Z_0\overline{\overline{S_{k12}}} \\ \overline{\overline{l}} - \overline{\overline{S_{k22}}} & Z_0\left(\overline{\overline{l}} + \overline{\overline{S_{k22}}}\right) \end{bmatrix} = QW. \quad (52)$$

Here

$$\begin{bmatrix} S_{11} & S_{12} & S_{13} & S_{14} \\ S_{21} & S_{22} & S_{23} & S_{24} \\ S_{31} & S_{32} & S_{33} & S_{34} \\ S_{41} & S_{42} & S_{43} & S_{44} \end{bmatrix} = \begin{bmatrix} \overline{\overline{S_{k11}}} & \overline{\overline{S_{k12}}} \\ \overline{\overline{S_{k21}}} & \overline{\overline{S_{k22}}} \end{bmatrix},$$

$$Q = \begin{bmatrix} 1-S_{11} & S_{12} & 50(1+S_{11}) & 50*S_{12} \\ S_{21} & 1-S_{22} & 50*S_{21} & 50*(1+S_{22}) \\ S_{31} & S_{32} & 50*S_{31} & 50*S_{32} \\ S_{41} & S_{42} & 50*S_{41} & 50*S_{42} \end{bmatrix}^{-1},$$

$$W = \begin{bmatrix} S_{31} & S_{41} & -50*S_{31} & -50*S_{41} \\ S_{32} & S_{42} & -50*S_{32} & -50*S_{42} \\ 1-S_{33} & S_{43} & 50*(1+S_{33}) & 50*S_{43} \\ S_{34} & 1-S_{44} & 50*S_{34} & 50*(1+S_{44}) \end{bmatrix}.$$

In the matrix, ports 1 and 2 are on the same side, while ports 3 and 4 are on the other side. We first calculate the RLGC parameters from the S-parameters of a short segment of the cable obtained using 2D extractor. Then, using the ABCD matrix, we cascade the segment to model cables of any desired length. Through derivation, it is shown that the S-parameters for cables of different lengths can be obtained. Based on the above equations, we can write a program for future design use, utilizing this numerical analysis to create a calculation program for convenient future applications.

III. CALCULATE S-PARAMETERS FOR NON-IDEAL TWINAX CABLES

A. Mathematical model verification

Due to the significant time demands of 3D full-wave simulations in the design process, particularly for cable lengths exceeding 1 meter, we have adopted a more efficient approach. First, the S-parameters obtained from the 2D extractor are converted into ABCD parameters using (52). Next, eigenmode decomposition and sorting are performed to derive the characteristic impedances and propagation constants. To determine R_C and R_π, eigenvalue decomposition is performed on the A-matrix of the ABCD matrix by (48). The eigenvectors yield $\begin{bmatrix} 1 & 1 \\ R_c & R_\pi \end{bmatrix}$. To obtain γ_C and γ_π, the eigenvalues of the A-matrix are extracted, resulting in $\begin{bmatrix} \cosh(\gamma_c l) & 0 \\ 0 & \cosh(\gamma_\pi l) \end{bmatrix}$. The diagonal elements are then processed using $\gamma_c = cosh^{-1}(eigenvalue\ 1)/l$. For Z_{C1}, Z_{C2}, $Z_{\pi 1}$, and $Z_{\pi 2}$, the B-matrix of the ABCD matrix is used. By substituting the previously determined γ_C, γ_π, R_C, R_π, and l, the characteristic impedances can be derived. Finally, the RLGC values are calculated using (27)–(45).

To validate our methodology, we confirmed the consistency of the RLGC parameters calculated using our approach with those directly extracted from the Ansys 2D extractor. We chose to compare the inductance and capacitance values, as these parameters are fixed, making them easier to compare and clearly demonstrating their origin from the Ansys 2D extractor. Figure 4 shows the parameter settings of Twinax cables.

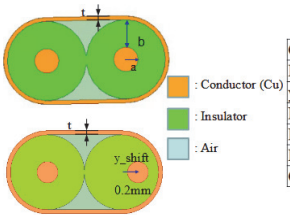

Conductor radius a	0.1275mm
Insulator thickness b	0.3225mm
y_shift	0.2mm
Dielectric constant ε_r	2.1
Loss tangent $\tan\delta$	0.001
Foil thickness t	50μm
Conductor material	Copper

Fig. 4. Parameter settings of Twinax cables.

Figure 5 shows a comparison of capacitance matrices (L). Figure 6 compares the inductance matrices (C). Results demonstrate that all the values are very close, verifying the accuracy of our calculation program.

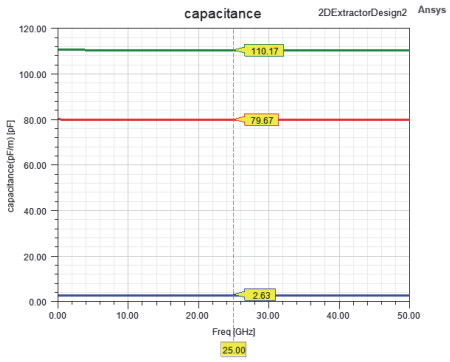

(a)

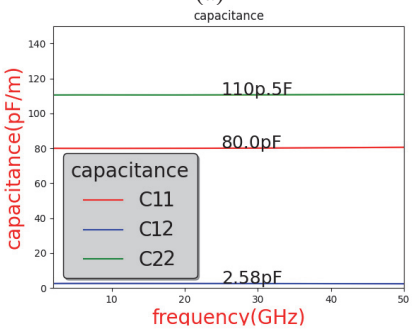

(b)

Fig. 5. Capacitance matrices. (a) 2D extractor output. (b) By calculation.

B. Calculating the parameters of non-ideal Twinax cables

Taking the most used server cable, the Twinax cable, as an example, the characteristic impedance

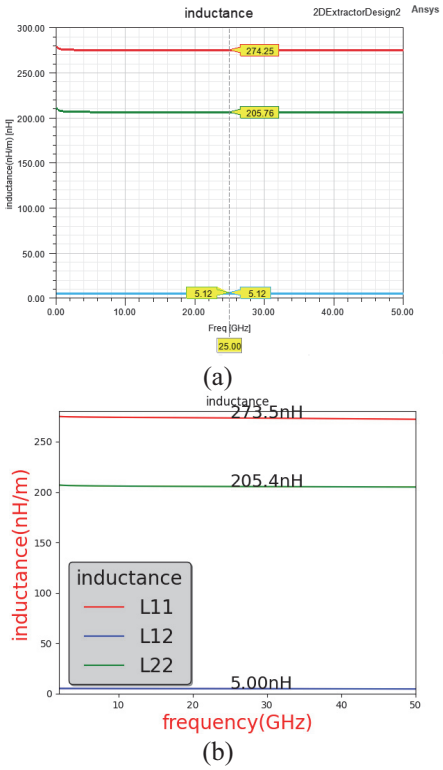

Fig. 6. Inductance matrices. (a) 2D extractor output. (b) By calculation.

is 100 ohms. Parameters are set as follows: copper conductor radius a = 0.1275 mm, insulator thickness b = 0.3225 mm, copper foil thickness t = 50 μm, $\varepsilon_r = 2.1$, and $\delta = 0.001$. First, we observe the characteristics of a 1-meter cable when the conductor position is asymmetrically offset. Conceptually, when the two conductors move in opposite directions by equal amounts, the system is still considered symmetric. In this case, the cable only exhibits odd and even mode characteristics, with minimal variation in $|S_{cd}|$.

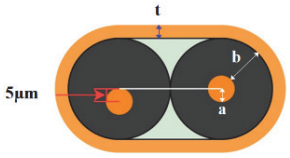

Conductor radius a	0.1275mm
Insulator thickness b	0.3225mm
z_shift	5µm
Dielectric constant ε_r	2.1
Loss tangent tanδ	0.001
Foil thickness t	50µm
Conductor material	Copper

Fig. 7. Cross-section of the cable when conductor is offset.

However, when one conductor is fixed at the center while the other is offset in any direction, the mode characteristics are no longer limited to odd or even modes. As shown in Fig. 7, when the left conductor is shifted downward by 5 μm, the modes are no longer purely odd or even. Figure 8 shows that with a 5 μm offset on one side of the conductor, there is no significant change in the RLGC parameters, whether it is self or mutual RLGC; the curves are nearly overlapping. Figure 9 illustrates the mixed-mode parameters under conductor offset, where S_{CD21} exhibits periodic fluctuations, approximately at −75 dB.

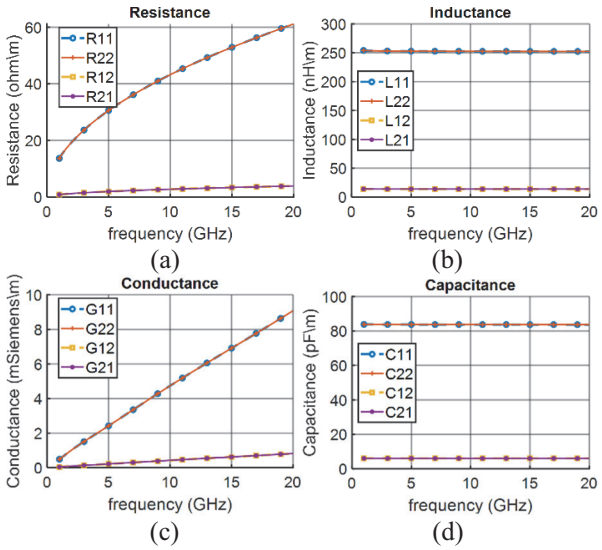

Fig. 8. RLGC parameters from calculation when the left-side conductor is downwardly offset by 5 μm. (a) Resistance. (b) Inductance. (c) Conductance. (d) Capacitance.

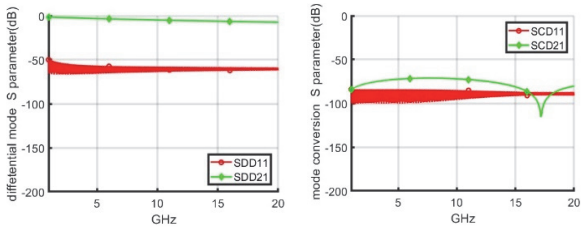

Fig. 9. Left-side conductor is downwardly offset by 5 μm for a 1-m cable. (a) S_{DD}. (b) S_{CD}.

The copper conductors inside the cable are produced through a drawing process. During production, variations in temperature and extrusion pressure can cause changes in the conductor diameter, potentially resulting in different diameters for the left and right conductors.

As shown in Fig. 10, with current precision machinery, the diameter difference can be controlled within 5 μm. This is assuming both conductors are centered with no positional offset.

Figure 11 shows that the RLGC parameters exhibit noticeable differences and are no longer overlapping. In

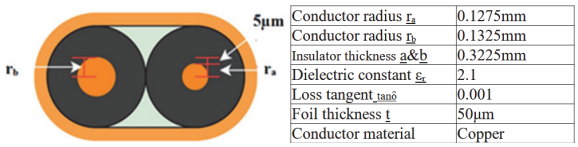

Conductor radius r_a	0.1275mm
Conductor radius r_b	0.1325mm
Insulator thickness a&b	0.3225mm
Dielectric constant ε_r	2.1
Loss tangent $_{\tan\delta}$	0.001
Foil thickness t	50μm
Conductor material	Copper

Fig. 10. Diameter difference of the copper conductor is r_b–$r_a = 5\ \mu$m.

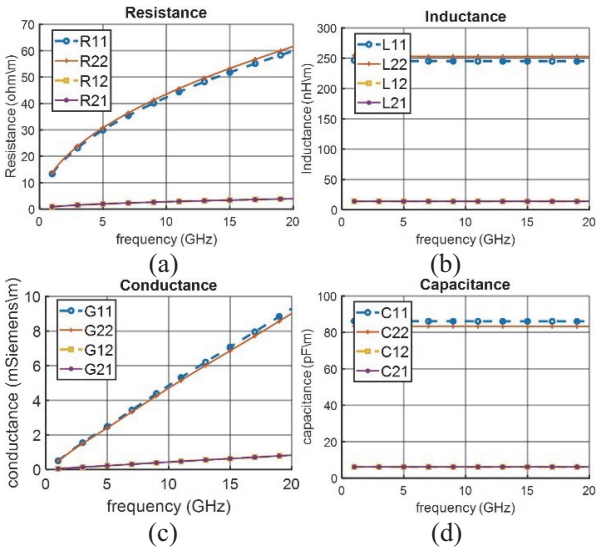

Fig. 11. RLGC parameters from the diameter difference of the copper conductor by 5 μm. (a) Resistance. (b) Inductance. (c) Conductance. (d) Capacitance.

Fig. 12, when calculating a 1-meter cable, the differential mode conversion S-parameter reaches −50 dB, which is within acceptable range in the industry.

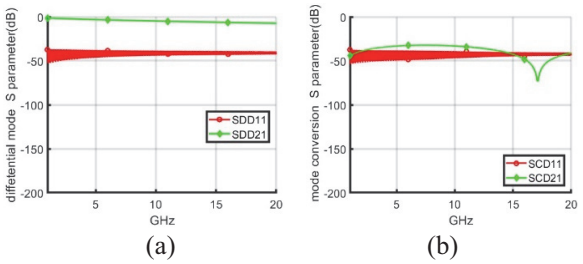

Fig. 12. Diameter difference of the copper conductor by 5 μm for a 1-m cable. (a) S_{DD}. (b) S_{CD}.

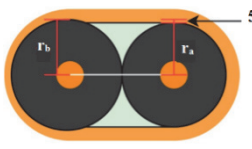

Conductor radius	0.1275mm
Insulator+Conductor r_a	0.38625mm
Insulator+Conductor r_b	0.39125mm
Dielectric constant ε_r	2.1
Loss tangent $_{\tan\delta}$	0.001
Foil thickness t	50μm
Conductor material	Copper

Fig. 13. Difference in insulator thickness r_b–$r_a = 5\ \mu$m.

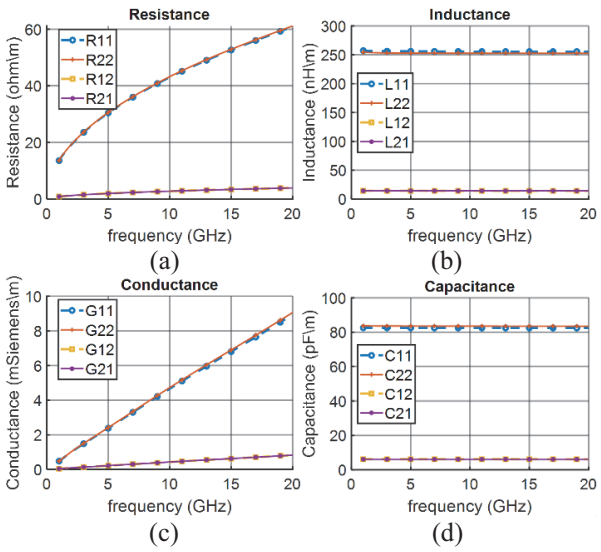

Fig. 14. RLGC parameters from difference in insulator thickness by 5 μm. (a) Resistance. (b) Inductance. (c) Conductance. (d) Capacitance.

Analyzing the thickness variation in the left and right insulation layers, the insulation is primarily formed through either physical or chemical foaming processes followed by extrusion. Due to differences in ambient temperature during production batches, variations in thickness may occur. The thickness is related to capacitance, and stray capacitance in the cable can slow down discharge rates, causing signal pulses to take longer to rise to a recognizable voltage. As a result, cables with lower capacitance exhibit more complete pulse waveforms, leading to better signal transmission performance. Additionally, the amount of air in the foam dielectric is related to the dielectric constant. For this discussion, we assume the dielectric constant is constant. Assuming a low dielectric constant of 2.1 for foamed EPE (expanded polypropylene), which is typically used in high-speed cables, we studied the impact when both conductors are the same size, but the insulation thickness differs by 5 μm, as shown in Fig. 13.

In Fig. 14, minimal resistance variation was observed, along with lower capacitance values. In Fig. 15, S_{CD11} is observed at −50 dB, which is within the acceptable range.

C. Impact from the skin effect

When the cable manufacturing process achieves high symmetry, there remains a difference between the measured and simulated insertion loss. Typically, after 10 GHz, the skin depth becomes very shallow, and surface characteristics begin to affect signal loss. Signal transmission might fall within the range of surface

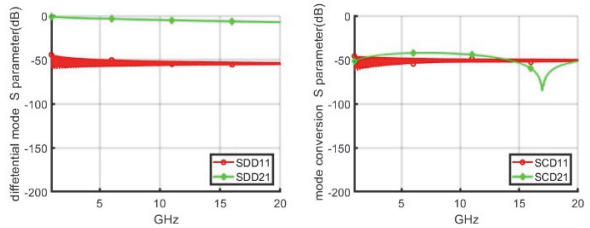

Fig. 15. Difference in insulator thickness by 5 μm for a 1-m cable. (a) S_{DD}. (b) S_{CD}.

roughness, which could worsen standing waves and reflections, elongating the signal path and increasing loss. In practice, the demand for low insertion loss copper continues to grow. In design, it is necessary to establish more realistic models.

Commercial software typically uses standard formulas to account for roughness, which represent a few traditional methods. As shown in Fig. 16, the surface features sharp peaks and valleys.

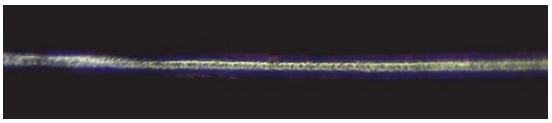

Fig. 16. Copper conductor surface under a microscope.

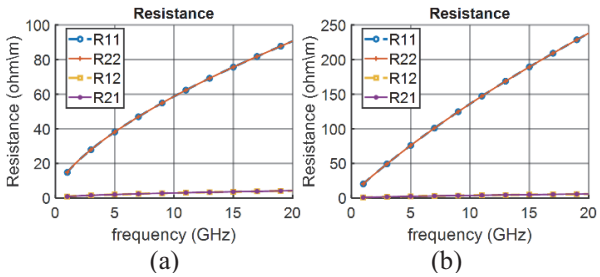

Fig. 17. The roughness of different copper conductors in resistance. (a) 1.4 μm. (b) 7.5 μm.

The simulation adopts the Huray model, which defines surface roughness by the number of spheres in each hexagon and their arrangement. The actual roughness value of the conductor can be calculated based on the manufacturer's parameters or measured data. Using HVLP2 copper roughness of 1.4 μm and STD copper roughness of 7.5 μm, we computed RLGC parameters. Comparison results are shown in Figs. 17–20.

By observing the resistance parameters, it is evident that the resistance changes with different surface roughness levels. The higher the roughness, the greater the resistance. For high-frequency signals, the roughness of

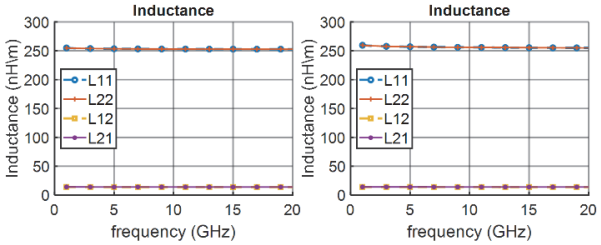

Fig. 18. Surface roughness of different copper conductors in inductance. (a) 1.4 μm. (b) 7.5 μm.

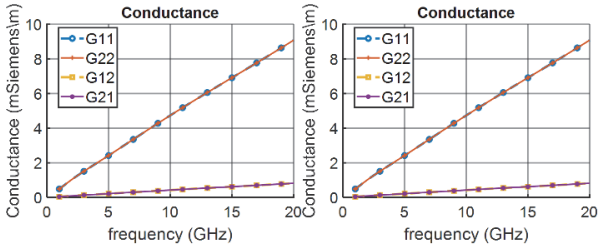

Fig. 19. Surface roughness of different copper conductors in conductance. (a) 1.4 μm. (b) 7.5 μm.

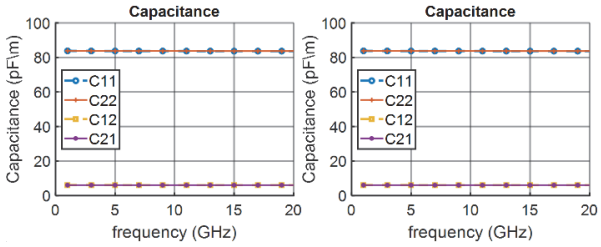

Fig. 20. Surface roughness of different copper conductors in capacitance. (a) 1.4 μm. (b) 7.5 μm.

the metal surface becomes a significant factor in signal loss, as shown in Fig. 21. The impact on differential-to-differential mode S-parameters ($|S_{DD}|$) is significant, while the impact on mode conversion S-parameters ($|S_{CD}|$) is relatively minor, as illustrated in Fig. 22.

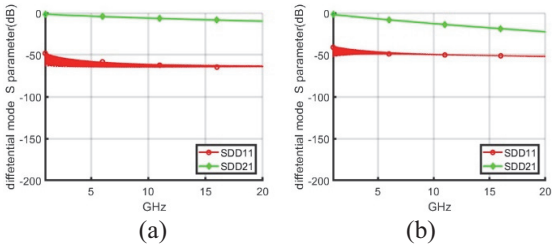

Fig. 21. Differential mode S-parameter (S_{DD}). (a) 1.4 μm. (b) 7.5 μm.

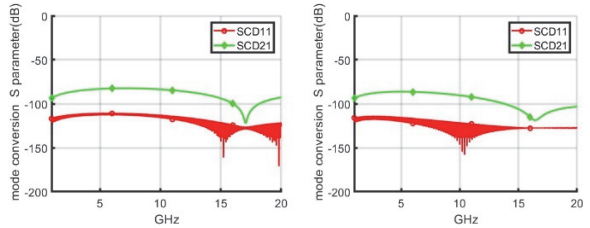

Fig. 22. Mode conversion S-parameter (S_{CD}). (a) 1.4 μm. (b) 7.5 μm.

IV. MEASUREMENT RESULTS OF TWINAX CABLE

We were unable to intentionally fabricate a worst-case Twinax cable with a 5 μm eccentric asymmetry for the purpose of comparing measurement and calculation results. Instead, we reverse-engineered the cross-sectional dimensions of a randomly selected, real Twinax cable from the production line. As shown in Fig. 23, the measured dimensions and contours were imported into the Ansys 2D extractor. Using these reverse-engineered dimensions, we obtained the S-parameters, calculated the RLGC parameters, and derived the S-parameters for a Twinax cable sample.

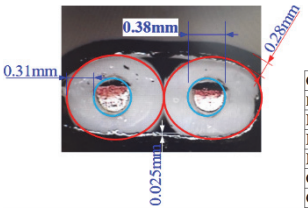

Conductor radius a	0.38mm
Insulator thickness b	0.31mm
Dielectric constant ε_r	2.1
Loss tangent tanδ	0.001
Foil thickness t	0.025mm
Outer jacket	0.28mm
Conductor material	Copper

Fig. 23. Cross-section of the Twinax cable.

Fig. 24. Device for 100-ohm cable measurement.

The sample was taken from a high-speed Twinax cable commonly used in AI server systems, with an original length of approximately 11 cm. An 8 cm section was cut for measurement. To verify our method, we compared the calculated results with VNA measurements of the 8 cm Twinax cable. The experimental setup is illustrated on Fig. 24.

Since direct measurement of the Twinax cable is not possible, fixtures were added on both sides to enable testing of the DUT. The measured S-parameters include the characteristics of the fixtures. We used the 2X-thru de-embedding technique [20, 21] to obtain the DUT's S-parameters. The results show a good agreement between the mixed-mode S-parameters calculated from the cross-sectional dimensions and the measured results, as seen in Fig. 25.

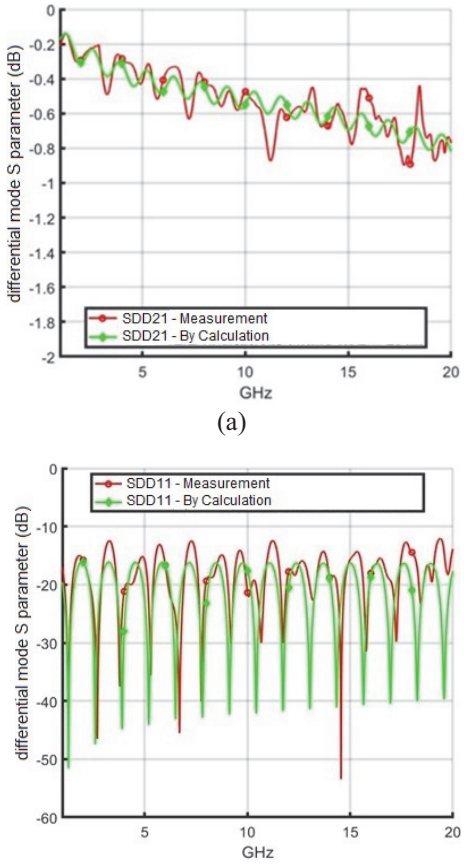

Fig. 25. Calculation and measurement comparison of 8 cm cable. (a) S_{DD21}. (b) S_{DD11}.

From these results, we can see that the cross-sectional dimensional differences in Twinax cables are a combination of various manufacturing tolerances. In production, improving precision is essential to enhance signal transmission quality.

V. CONCLUSION

In this paper, we propose a computational method that extends the fundamental theory of odd and even modes to calculate RLGC parameters and obtain the S-parameters of asymmetric Twinax cables. We also evaluate the impact of copper conductor surface roughness on signal transmission. For transmission line losses, we estimate resistance and conductance parameters. Additionally, we examine mixed-mode S-parameters to ensure product quality. A server cable was physically

measured, reverse-engineered, and its cross-sectional dimensions were compared with the S-parameters calculated using our method. The results demonstrate a strong agreement between the calculations and actual measurements. This computational approach is highly efficient and can be used to define future product standards. Our method addresses the time-consuming nature of 3D full-wave simulations for longer cables, providing the cable industry with an effective way to quickly assess production quality.

ACKNOWLEDGMENT

This work was supported by BizLink International Corporation.

REFERENCES

[1] *Physical layer specifications and management parameters for 100 Gb/s operation over backplanes and copper cables*, IEEE standard 802.3bj-2014 (amendment to IEEE standard 802.3-2012 as amended by IEEE standard 802.3bk-2013) 2014.

[2] E. Mayevskiy and J. Huffaker, *Limitations of the intra-pair skew measurements in gigabit range interconnects* [Online]. Available: https://www.te.com/content/dam/te-com/documents/medical/global/TE_WhitePaper_Limitations_of_Intra-Pair_Skew_Meas_061016.pdf

[3] Z. Chen, M. Prasad, D. O'Connor, P. Bond, and A. Muszynski, "Differential Twinax cable modeling by measured 4-port S-parameters," in *Proc. IEEE 14th Topical Meeting Elect. Perform. Electron. Packag*., pp. 87–90, 2005.

[4] T. Sugiyama, H. Nonen, I. Fukasaku, H. Ishikawa, and T. Kumakura, "High-speed transmission copper cable for 25Gbit/s/lane," in *2013 3rd IEEE CPMT Symposium Japan*, Kyoto, Japan, pp. 1–4, 2013.

[5] D. Nozadze, A. Koul, K. Nalla, M. Sapozhnikov, and V. Khilkevich, "Effective channel budget technique for high-speed channels due to differential P/N skew," in *2017 IEEE International Symposium on Electromagnetic Compatibility & Signal/Power Integrity (EMCSI)*, Washington, DC, USA, pp. 34–39, 2017.

[6] D. N. de Araujo, G. Pitner, M. Commens, B. Mutnury, and J. Diepenbrock, "Full-wave, TwinAx, differential cable modeling," in *2008 58th Electronic Components and Technology Conference*, Lake Buena Vista, FL, USA, pp. 1684–1689, 2008.

[7] A. Talebzadeh, K. Koo, and P. Vuppunutala, "SI and EMI performance comparison of standard QSFP and flyover QSFP connectors for 56+ Gbps applications," in *2017 IEEE International Symposium on Electromagnetic Compatibility & Signal/Power Integrity (EMCSI)*, Washington, DC, USA, pp. 776–781, 2017.

[8] Y. Liu, "Far-end crosstalk analysis for stripline with inhomogeneous dielectric layers (IDL)," in *2021 IEEE International Joint EMC/SI/PI and EMC Europe Symposium*, Raleigh, NC, USA, pp. 825–830, 2021.

[9] Y. Liu, S. Yong, Y. Guo, and J, He, "An empirical modeling of far-end crosstalk and insertion loss in microstrip lines," *IEEE Transactions on Signal and Power Integrity*, vol. 1, pp. 130–139, 2022.

[10] E. J. Denlinger, "Frequency dependence of a coupled pair of microstrip lines (correspondence)," *IEEE Transactions on Microwave Theory and Techniques*, vol. 18, no. 10, pp. 731–733, 1970.

[11] S. Yong, K. Cai, B. Sen, J. Fan, V. Khilkevich, and C. Sui, "A comprehensive and practical way to look at crosstalk for transmission lines with mismatched terminals," in *2018 IEEE Symposium on Electromagnetic Compatibility, Signal Integrity and Power Integrity (EMC, SI & PI)*, Long Beach, CA, USA, pp. 538–543, 2018.

[12] S. Yong, Y. Liu, and V. Khilkevich, "Dielectric loss tangent extraction using modal measurements and 2-D cross-sectional analysis for multilayer PCBs," *IEEE Transactions on Electromagnetic Compatibility*, vol. 62, no. 4, pp. 1278–1292, Aug. 2020.

[13] Y. Liu, S. Bai, C. Li, V. S. De. Moura, B. Chen, and X. Wang, "Inhomogeneous dielectric induced skew modeling of Twinax cables," *IEEE Transactions on Signal and Power Integrity*, vol. 2, pp. 94–102, 2023.

[14] N. Dikhaminjia, J. Rogava, M. Tsiklauri, M. Zvonkin, J. Fan, and J. L. Drewniak, "Fast approximation of sine and cosine hyperbolic functions for the calculation of the transmission matrix of a multiconductor transmission line," *IEEE Transactions on Electromagnetic Compatibility*, vol. 57, no. 6, pp. 1698–1704.

[15] A. A. Bhatti, "A computer-based method for computing the N-dimensional generalized ABCD parameter matrices of N-dimensional systems with distributed parameters," in *Proceedings of the Twenty-Second Southeastern Symposium on System Theory*, Cookeville, TN, USA, pp. 590–593, 1990.

[16] W. I. Bowman and J. M. McNamee, "Development of equivalent Pi and T matrix circuits for long untransposed transmission lines," *IEEE Transactions on Power Apparatus and Systems*, vol. 83, no. 6, pp. 625–632, 1964.

[17] U. Arz, D. F. William, D. K. Walker, and H. Grabinski, "Asymmetric coupled CMOS lines: An experimental study," *IEEE Transactions on Microwave Theory and Techniques*, vol. 48, no. 12, pp. 2409–2414, 2000.

[18] K.-H. Tsai and C.-K. C. Tzuang, "Mode symmetry assessment of structurally non-uniform asymmetric coupled lines meandered for CMOS passive component design," in *2009 IEEE MTT-S International*

Microwave Symposium Digest, Boston, MA, USA, pp. 285–288, 2009.

[19] W.-H. Tsai, D.-B. Lin, T.-F. Tseng, and C.-H. Ho, "Analysis of electrical characteristics of Twinax cable with asymmetric structures," in *2024 IEEE Joint International Symposium on Electromagnetic Compatibility, Signal & Power Integrity: EMC Japan / Asia-Pacific International Symposium on Electromagnetic Compatibility (EMC Japan/APEMC Okinawa)*, Ginowan, Okinawa, Japan, pp. 342–345, 2024.

[20] J.-Y. Ye, J. Fan, X. Cao, Q.-M. Cai, Y. Zhu, and Y. Zhu, "A 2x-thru standard de-embedding method of surface components in high-speed PCBs," in *2022 IEEE USNC-URSI Radio Science Meeting (Joint with AP-S Symposium)*, Denver, CO, USA, pp. 58–59, 2022.

[21] W.-H. Tsai, D.-B. Lin, P.-J. Lu, and T.-F. Tseng, "De-embedding technique for extraction and analysis of insulator properties in cables," *Applied Computational Electromagnetics Society (ACES) Journal*, vol. 40, no. 6, pp. 550–563, 2025.

Wei-Hsiu Tsai received a B.S. degree in Mathematics from the Fu Jen Catholic University, New Taipei, Taiwan, in 1999, and an M.B.A. degree in industrial management from the National Taiwan University of Science and Technology (Taiwan Tech), Taipei, in 2019. He is pursuing a Ph.D. degree in the department of electronic and computer engineering from the National Taiwan University of Science and Technology (Taiwan Tech) under the supervision of Prof. Ding-Bing Lin. He is currently an Engineer with BizLink International Corporation, New Taipei. His research interests include high-speed transmission techniques and high-frequency measurement techniques.

Ding-Bing Lin (S'89-M'93-SM'14) received the M.S. and Ph.D. degrees in electrical engineering from National Taiwan University, Taipei, Taiwan, in 1989 and 1993, respectively. From August 1993 to July 2016, he has been on the faculty of the Electronic Engineering Department, National Taipei University of Technology, Taipei, where he was Associate Professor, Professor and Distinguished Professor in 1993, 2005, and 2014, respectively. Since August 2016, he had been with National Taiwan University of Science and Technology, Taipei, where he is currently Professor in the Electronic and Computer Engineering Department. His research interests include wireless communication, antennas, high-speed digital transmission, and microwave engineering. From 2015 to 2018, he served as the Taipei Chapter Chair, IEEE EMC society. He has served as the Taipei Chapter Chair, IEEE AP society since 2022. He also serves as Associate Editor of *IEEE Transactions of Electromagnetic Compatibility* since 2019 and serves on the Editorial Board of the *International Journal of Antennas and Propagation* since 2014. He has published more than 250 papers in international journals and conferences. Lin was the recipient of the Annual Research Outstanding Award of the College of Electrical Engineering and Computer Science in 2004, 2006, and 2008. After he received these three awards, the College of Electrical Engineering and Computer Science awarded him the College Research Outstanding Award to highlight his research achievements. He was also the recipient of the Taipei Tech Annual Outstanding Research Award in 2008. Lin is the recipient of the Annual Research Outstanding Award of the National Taiwan University of Science and Technology in 2024.

Cheng-Hsun Ho received the B.S. degree from Department of Electronic and Computer Engineering, National Taiwan University of Science and Technology (NTUST), Taipei, Taiwan, in 2021, and the M.S. degree in Electronic and Computer Engineering from the National Taiwan University of Science and Technology (Taiwan Tech), Taipei, in 2023. His research includes high-frequency measurement and cable model design.

Tzu-Fang Tseng received the B.S. degree in electrical engineering from National Taiwan University, Taipei, Taiwan, in 2009, and the Ph.D. degree in photonics and opto-electronics from National Taiwan University, Taipei, in 2015. She started working in industry in 2015. Her research interests include MMW signal transmission, signal integrity in high-speed cables and connectors, and optical planar lightwave circuit design and applications.